Real-time Voltage Stability Monitoring and Control for Load Areas: A Hybrid Approach

A Dissertation Presented for the

Doctor of Philosophy

Degree

The University of Tennessee, Knoxville

Fengkai Hu

August 2016

Copyright © 2016 by Fengkai Hu

All rights reserved.

DEDICATION

This dissertation is dedicated to my beloved parents, Jingdong Hu and Wenjing Liu, my little angel, Vivian Hu, and my wife, Jing Li, whose love and encouragement make it possible for me to finish this work.

ACKNOWLEDGEMENTS

I would like to express my thanks to those who helped me with various aspects of conducting research and writing this dissertation.

Primarily, I would like to express my deepest gratitude to my advisor, Dr. Kai Sun for his continuous guidance and persistent help for this dissertation and all other research during my Ph.D. study at the University of Tennessee at Knoxville (UTK). I am grateful to Dr. Kai Sun for funding my Ph.D. Study.

I am very thankful to Dr. Fangxing "Fran" Li, Dr. Leon M. Tolbert, and Dr. Xueping Li for their time and efforts in serving as the members of my dissertation committee.

Moreover, I would like to express my special thanks to all the students and scholars in our group, Bin Wang, Weihong Huang, Nan Duan, Denis Osipov, Yongli Zhu, Wenyun Ju, Dr. Chengxi Liu, Dr. Ping Ma, Dr. Miao Fan, Dr. Junjian Qi, Dr. Rui Yao, and Dongsheng Cai for being supportive to my research.

In addition, I gratefully appreciate the support from Di Shi, Zhiwei Wang, Guangyi Liu and Yuxiang Sun in GEIRINA.

Finally, I would like to thank all my friends and professors in the Center for Ultra-Wide-Area Resilient Electric Energy Transmission (CURENT) who create a loving and friendly atmosphere for conducting research.

ABSTRACT

This dissertation proposes a hybrid approach for real-time monitoring and controlling voltage stability of a load area fed by *N* tie lines. This hybrid approach integrates both simulation-based and measurement-based approaches for voltage stability assessment (VSA).

First, for measurement-based VSA (MBVSA), a new method is proposed for monitoring and control of load areas, which adopts an *N*+1 buses equivalent system so as to model and monitor individual tie lines of a load area compared to a traditional MBVSA method adopting a Thevenin equivalent. For each tie line, the new method solves the power transfer limit against voltage instability analytically as a function of all parameters of that equivalent, which is online identified from real-time synchronized measurements on boundary buses of the load area. Thus, this new MBVSA method can directly calculate the real-time power transfer limit on each tie line.

Second, in order to assess the voltage stability margins under an *n*-1 contingency, based on the proposed MBVSA method, two sensitivity analyses have been performed, which are respectively for the parameter sensitivity of the equivalent system and the sensitivity of the tie line flow under an *n*-1 contingency.

Third, the proposed MBVSA method implemented for both the real-time condition and potential *n*-1 contingencies is integrated with the simulation-based VSA approach to form a hybrid approach. The MBVSA method helps reduce the computation burden by eliminating the unimportant contingencies while the simulation-based method provides accurate information for specific "*what if*" scenarios such as stability limit and margin

indices under *n*-1 contingency conditions. In addition, simulation using the model of the system can provide recommendations for preventive control if potential voltage instability is identified.

This proposed hybrid VSA approach has been validated on the NPCC (Northeast Power Coordinating Council) Large-scale Test Bed (LTB) system developed by the CURENT (Center for Ultra-Wide-Area Resilient Electric Energy Transmission Networks), and also implemented on the CURENT Hardware Test Bed (HTB) system. The effectiveness of the MBVSA in real-time monitoring and closed-loop control against voltage instability has been validated.

Keywords: Load center, *N*+1 buses equivalent, parameter estimation, phasor measurement unit (PMU), power transfer limit, Thevenin equivalent, voltage stability margin.

TABLE OF CONTENTS

CHAPTER 1 INTRODUCTION AND BACKGROUND INFORMATION 1

1.1 Introduction 1

1.2 Definitions 2

1.2.1 Voltage Stability and Instability 2

1.2.2 PV Curve 4

1.2.3 Voltage Stability Margin 5

1.2.4 Voltage Stability Classification 6

1.3 Model-based Voltage Stability Assessment 7

1.3.1 Modal Analysis 8

1.3.2 Continuation Power Flow (CPF) 9

1.3.3 Singular Value Decomposition (SVD) 10

1.3.4 Voltage Sensitivity Method 11

1.3.5 Bifurcation Theory 11

1.3.6 Dynamic Simulation Analysis 13

1.4 Measurement-based Voltage Stability Assessment 15

1.4.1 Thevenin Equivalent (TE) based Voltage Stability Indictor 15

1.4.2 Coupled Single-port Equivalent-based Method 17

1.4.3 Voltage Instability Load Shedding (VILS) 19

1.4.4 Measurement-based Voltage Stability Assessment (MBVSA) 21

1.4.5 TE-based Hybrid VSA Method for *n*-1 Conditions 22

1.4.6 An Adaptive Three-bus Power System Equivalent 23

1.5 Contribution of this Work: Hybrid Real-time Voltage Stability Assessment 24

CHAPTER 2 *N*+1 BUSES EQUIVALENT SYSTEM..... 27

2.1 Introduction..... 27

2.2 System Parameter Estimation 29

2.2.1 Identification of the External System Parameters..... 29

2.2.2 Identification of the Load Area Parameters 31

2.3 Solving the Power Transfer Limit of Each Tie Line..... 33

2.4 Properties of the Power Transfer Limits for the *N*+1 Equivalent Model.... 37

2.5 Online Scheme for Implementation 43

2.6 Demonstration on a 4-bus Power System 45

2.7 Case Studies on the NPCC Test System 51

2.7.1 Generator Trip Followed by Load Increase Leading to Voltage Instability 53

2.7.2 Generator Trip Followed by a Tie-Line Tip Causing Voltage Instability 63

2.7.3 Two Successive Tie Line Trips Causing Voltage Instability..... 68

2.7.4 Shunt Switching to Postpone Voltage Instability 72

2.8 Case Studies on a Detailed NYISO Model 73

2.9 Conclusion 77

CHAPTER 3 THE *N*-1 SENSITIVITY ANALYSIS OF *N*+1 BUSES EQUIVALENT MODEL 79

3.1 Introduction 79

3.2 Sensitivity Analysis for *n*-1 Contingency 80

3.2.1 *n*-1 Contingency Sensitivity Analysis for Equivalent Model 80

3.2.2 *n*-1 Contingency Sensitivity Analysis of Tie Line Flow 83

3.3 Implementation of the *n*-1 Contingency Sensitivity Analysis 87

3.4 Case Studies 88

3.4.1 Verification of the Impedance Sensitivity Analysis for *n*-1 Contingency 90

3.4.2 Verification of the Tie Line Power Flow Sensitivity for *n*-1 Contingency 92

3.4.3 *n*-1 Contingency Sensitivity Analysis Study 92

3.5 Conclusion 97

CHAPTER 4 REAL-TIME HYBRID VOLTAGE STABILITY ASSESSMENT 98

4.1 Introduction 98

4.2 Proposed Framework 98

4.3 Implementation Studies 101

4.4 Considerations for Practical Implementation 108

4.5 Conclusion 109

CHAPTER 5 DEMONSTRATIONS ON THE CURENT HARDWARE TEST BED SYSTEM 110

5.1 Introduction 110

5.2 Settings and Scenarios of Demonstrations 113

5.3 Scenario 1: Voltage Collapse without Control 118

5.4 Scenario 2: Automatic Control against Voltage Collapse 120

5.5 Conclusion 122

CHAPTER 6 CONCLUSION AND FUTURE WORK 123

6.1 Summary of Contributions 123

6.2 Future Works 124

LIST OF REFERENCES 125

APPENDIX 140

Publications during Ph.D. Study 141

VITA 143

LIST OF TABLES

Table 1. Values of transfer impedances 46

Table 2. Errors of the LODF 92

Table 3. Margins of all *n*-1 line trip contingency at 200s 101

Table 4. Stages of the simulated instability scenario 102

LIST OF FIGURES

Figure 1. PV curve and P_{margin} 4

Figure 2. Calculations of CPF 10

Figure 3. Thevenin equivalent for 2-bus system. 15

Figure 4. Thevenin reactance and load impedance. 16

Figure 5. Multi-port network system model. 17

Figure 6. Coupled single-port system equivalent. 19

Figure 7. MBVSA on a load area 21

Figure 8. Proposed transformation. 22

Figure 9. 3-bus System. 23

Figure 10. Line flow limits for tight (a) and weak (b) interconnections between two buses. 24

Figure 11. *N*+1 buses equivalent. 29

Figure 12. Nodes connection for *N*+1 buses equivalent. 39

Figure 13. Flowchart of the new method. 45

Figure 14. PV curves for weak and tight connections between boundary buses. 47

Figure 15. Tie-line flows and limits for Group A (weak connection). 49

Figure 16. Tie-line flows and limits for Group B (tight connection) 49

Figure 17. P1 and limits for Group A. 50

Figure 18. P2 and limits for Group A. 50

Figure 19. P3 and limits for Group A. 51

Figure 20. Map of NPCC system and CLC area. 52

Figure 21. Voltage magnitudes at CLC boundary buses. 53

Figure 22. PV curves monitored at the CLC boundary buses. 54

Figure 23. External system bus magnitudes. 55

Figure 24. External system bus angles. 55

Figure 25. Real-time estimation of load impedance magnitudes. 56

Figure 26. Result from a TE-based method. 56

Figure 27. Transfer limits of each tie line calculated by the new approach. 58

Figure 28. Time performances on online parameter estimation. 61

Figure 29. Comparison of different optimization time windows. 62

Figure 30. Comparison of initial values with errors. 62

Figure 31. Voltage magnitudes at CLC boundary buses. 64

Figure 32. Transfer limits of each tie line calculated by the new approach. 65

Figure 33. Voltage magnitudes at CLC boundary buses. 68

Figure 34. Transfer limits of each tie line calculated by the new approach. 69

Figure 35. Voltage magnitudes at CLC boundary buses. 72

Figure 36. P_{35} vs. its limits. 73

Figure 37. Load pocket Area Scheme. 74

Figure 38. Voltage magnitude and angle of voltage collapse scenario. 76

Figure 39. Active power and reactive power of voltage collapse scenario. 76

Figure 40. Voltage stability limits results of voltage collapse scenario. 77

Figure 41. System transformation. 81

Figure 42. LODF step 1. 85

Figure 43. LODF step 2. 86

Figure 44. Implementation of the *n*-1 contingency sensitivity analysis. 87

Figure 45. Map of CLC area. 88

Figure 46. Voltage magnitudes at CLC boundary buses. 89

Figure 47. PV curves. 90

Figure 48. Transfer conductance comparison. 91

Figure 49. Transfer susceptance comparison. 91

Figure 50. Transfer limits of each tie line under *n*-1 line trip contingency. 94

Figure 51. Hybrid approach intelligence. 100

Figure 52. Voltages of three boundary buses. 102

Figure 53. Scenario demonstration. 105

Figure 54. Trajectory of transmission line PV curve with preventive control triggered. 114

Figure 55. Closed-loop control strategy. 115

Figure 56. HTB control and communication structure. 116

Figure 57. HTB control center. 116

Figure 58. HTB three-area system topology. 117

Figure 59. HTB three-area system topology. 118

Figure 60. PV curves of transfer active power to bus 12 and bus 13. 119

Figure 61. Actual power transfers and their limits. 120

Figure 62. Trajectories of tie line power transfer PV curves with preventive control triggered. 121

Figure 63. Actual power transfers and their limits. 122

CHAPTER 1

INTRODUCTION AND BACKGROUND INFORMATION

1.1 Introduction

Growths in electrical energy consumptions and penetration of intermittent renewable resources would make power transmission systems more often operate close to their stability limits. Among all stability issues, voltage instability due to the inability of the transmission or generation system to deliver the power required by loads is one of major concerns in today's power system operations [1].

At present, some electricity utilities use model-based online voltage stability assessment (VSA) software tools to assist operators in foreseeing potential voltage instability. Based on a state estimate on the operating condition, those software tools employ power system models to simulate assumed disturbances such as contingencies and load changes. However, such a model-based approach has its limitations: the fidelity of its results highly depends on the accuracy of power system models; it needs a convergent, accurate state estimate in order to conduct stability assessment, which may be hard to obtain under stressed system conditions.

Usually, voltage instability initiates from a local bus but may develop to wide-area or even system-wide instability which leads to a system-wide issue. In order to analyze and mitigate this wide-area voltage stability issue, many researches have been conducted during the past decade. Especially after the Phasor Measurement Unit (PMU) technology

brought GPS synchronized accurate measurements, many researchers proposed and implemented the algorithms to assess many stability issues [2-8].

For the purpose of clarity, the basic concepts of voltage stability are firstly reviewed. All the existing methods for voltage stability analysis and their associated problems are then overviewed. The thesis contributions are presented at the end of this chapter.

1.2 Definitions

1.2.1 Voltage Stability and Instability

Voltage stability is one of the major concerns in today's power grid. It requires acceptable voltage levels, and its criticality plays an important role in the system operation which significantly affects the power transfer capability. Normally, voltage magnitudes drop to transmit the power along the transmission lines, and the these drops between the generation and load buses will remain in a certain range if the system is operating in a secure region. As the renewable energy and load keep increasing recently, the power transfers in the transmission system are closer to their limits which challenge the system operators continually.

When the system engages a disturbance and the load keeps consuming more and more power, the bus voltage magnitudes of the power grid will decrease. If the voltage stability margin is insufficient, the voltage instability may finally happen, which is defined as an uncontrollable decline in voltage magnitudes, followed by the system blackout. This phenomenon usually occurs following the cascading events.

Usually, voltage instability happens after some contingencies, such as generator trip or transmission line trip, which are extremely critical for the resilience power grid. The voltage instability firstly initials from one local bus or one load area, and then may spread out to the whole power grid when it is not constrained locally. Then, voltage collapse may finally happen, and the voltage magnitudes may decrease to extremely low levels and will not be able to be back to normal condition. Following that, the system blackout happens, and it causes the loss of elements in the power system and will not be able to provide the electricity service. In order to recover the system from blackout, the restoration process needs to be planned and conducted, which needs lots of efforts even with high probability to fail.

Many countries have planned to construct many new wind farms, however, the load centers are usually far from the wind farms. These two facts tell the trend that we will need to transfer these wind powers through long distance transmission corridors to the load centers, when the load centers are already stressed. So all of these factors make these tie lines transferring power closer to their limits, and thus largely challenging the voltage stability margins. However, due to the consideration of the economic efficiency, the generation and transmission facilities are constructed slowly and sometime cannot satisfy the requirements from the power market.

Therefore, the probability of the occurrence of the voltage instability is significantly increasing in recent decade, and attracts many researchers to make a lot of efforts to investigate the voltage instability. Compared to the angle stability, the voltage stability gains more attention recently due to the applications of the renewable energy solution and

the widely used power electronics devices. In the future, the renewable energy will increase rapidly beyond doubt, where the power electronics will be applied in a wider range in the power grid. Accordingly, there are lots of needs to study the voltage collapse phenomena and provide new and practical algorithms for both monitoring and control applications.

1.2.2 PV Curve

As shown in Figure 1, the curve which relates voltage to active power for a load or a transmission line is called PV curve. Usually, power systems normally operate at the upper part of the PV curve, but the figure also confirms the existence of a maximum load power at the "nose" point.

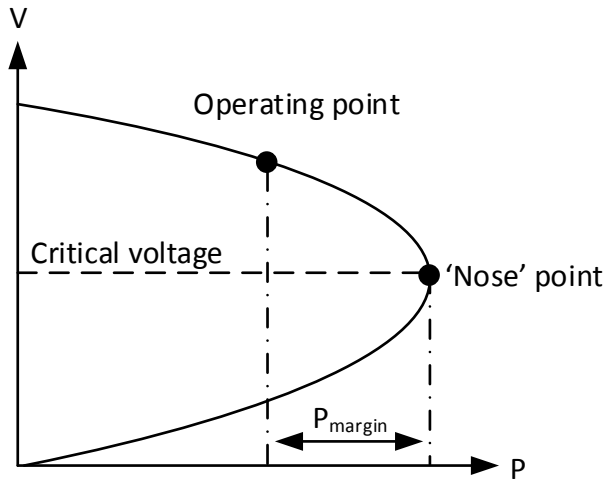


Figure 1. PV curve and P_{margin}.

The analytical expression of the PV curve can be easily derived for a small power system with all state variables available. However, in the real world, power systems are much more complex than a small system, and they have thousands of loads, generators and

transmission lines. The complexity of the systems makes it impossible to obtain PV curves accurately, and it is extremely challenging to be applied in the real-time operation environment.

1.2.3 Voltage Stability Margin

As shown in Figure 1, the system' voltage stability margin P_{margin} which is the distance between the current operating point and the maximum loadability limit tells the voltage stability in terms of active power. Usually, the voltage stability margin refers to the load loadability, however, it can also be utilized for a system interface or a load center. If the voltage stability margin is smaller than a certain threshold, the system is considered in a dangerous operating condition and remedial actions should be taken to avoid voltage instability.

There are two types of voltage stability margin indices proposed by many researchers:

1. Contingency-dependent: it is usually utilized in traditional voltage stability assessment methods for providing the operators the voltage stability margins under some predefined contingencies. It can be estimated by many commercial simulation tools.

2. Contingency-independent: it is usually used in a real-time environment to provide the current voltage stability margins. The difference between this one and the contingency-dependent is that this one does not rely on the predefined contingencies.

There are many factors which influence the accuracy of the voltage stability margins, for example, the variation of the transformer tap changers, the changes of the reactive power from either generators or some reactive support devices. Furthermore, the power grid is one of the most complicated system in the world, usually, it has hundreds of generators, thousands of transmission lines and loads. The dynamic characteristics of the system are also difficult to be modelled accurately. There are many uncertainties for the variation pattern of the load or the power flow.

However, with more practical considerations, there are some additional factors which have impacts on the accuracy: such as inaccurate system models, diverged state estimation results, high computational burden and difficulty covering all possible disturbances and uncertainties. As discussed in the above paragraphs, the model-base methods have many limitations. To improve these limitations, using measurement data to directly assess contingency-independent voltage stability indices may be one of the solutions.

This method can be more reliable since it does not rely on the model accuracy, and it reflects the system behavior in real time. The control strategies may be triggered by the real-time indices. Finally, the effectiveness of voltage control actions can be verified.

1.2.4 Voltage Stability Classification

For the better understanding of the voltage stability phenomenon, voltage stability can be divided into the following two classes according to the scale of the disturbance.

1. Small disturbance voltage stability: This type of voltage stability is a result of a small perturbation in the system. One common type of such perturbations is a gradual increase in the system loads.

2. Large disturbance voltage stability: This type of voltage stability happens as a result of a large change in the system, which could be a fault on a major transmission line, sudden outage of a transmission line or a generator.

1.3 Model-based Voltage Stability Assessment

Some indices provided by the model-based VSA is utilized to estimate the voltage stability margin of the system. If the stability margin is not sufficient, the remedial action may be taken to prevent the system from collapse. There exists an issue for the stability margin which is considered as a fixed variable for the model-based method, but in reality, it can be effected by a lot of factors, such as topology change, load/generation variation and the reactive power support.

Thus, the real time assessment of the voltage stability has significant meaning for the system operation. The idea assessment method has to be reliable all the time, even when the system is heavily stressed or under some critical disturbances. The accuracy of the assessment method has to be promised and thus its indices can be utilized for taking the remedial control actions to prevent the system from voltage collapse or any critical cascading events.

Recently, simulation-based Voltage Security Assessment (VSA) tools are applied to analyze either steady-state or transient voltage stability issues. For the steady-state

analysis, many methods are based on or derived from power flow formulation in the literature as below.

1.3.1 Modal Analysis

According to the saddle-node bifurcation theory, the static voltage stability is related to the power flow equations under one certain operating condition. Therefore, the modal analysis based on power flow equations which involves eigenvalue analysis of the system Jacobian matrix was proposed in [9]. Firstly, the linearized power flow equation is shown as below.

$$\begin{bmatrix} \Delta P \\ \Delta Q \end{bmatrix} = \begin{bmatrix} J_{P\theta} & J_{PV} \\ J_{Q\theta} & J_{QV} \end{bmatrix} \begin{bmatrix} \Delta \theta \\ \Delta V \end{bmatrix} \tag{1-1}$$

Let ΔP=0, there is

$$\Delta V = J_R^{-1} \Delta Q \tag{1-2}$$

where $J_R = J_{QV} - J_{Q\theta} J_{P\theta}^{-1} J_{PV}$ is the reduced Jacobian matrix of the system. It represents the linearized relationship between the incremental changes in bus voltage magnitudes and bus reactive power injections. This matrix becomes singular at the PV curve “nose” point.

The left eigenvectors of J_R give an indication of bus participation factors of the different modes given by the eigenvalues. Therefore, the voltage collapse is essentially the collapse of the voltage in a mode (critical mode). The minimum eigenvalue gives the critical mode because it will be zero when the system moves toward instability. Positive eigenvalues indicate the system is stable, while negative numbers mean an unstable system. In the modal analysis, the participation factors of can also be utilized to identify the critical modes where is the most important feature of the modal analysis method and is widely

used in voltage stability analysis studies [10] [11]. Although the eigenvalue gives an indication of stability, it is not a good indicator because of the nonlinearity of the power flow equations.

1.3.2 Continuation Power Flow (CPF)

Power flow analysis is a useful tool in voltage stability analysis. The maximum loadability of a power system can be determined by increasing the loads with a certain pattern in the computation of power flow until the maximum loading point is reached. A modification of this method known as Continuation power flow is used to find a static voltage stability margin, and it overcomes the singular problem by reformulating the differential algebraic equations so that they can remain well-conditioned even at the loading conditions near the stability limit [12].

The general principle of the continuation power flow is to utilize the predictor and corrector scheme. It starts from a known operating condition. After parameters have been changed, a prediction step is made, and from that point, a corrector routine using the Newton-Raphson technique will calculate the new equilibrium point. The parameterization step is then utilized to avoid the singularity of the Jacobian matrix at saddle node. A continuation method was used to detect the voltage stability limit by The University of Waterloo Power FLOW (UWPFLOW) program. With the support of modern computer hardware and software technology, many attempts have also been made to use CPF for online applications [13]. However, the computation time is still a main concern in online applications. Moreover, it is difficult to determine the vulnerable loads, branches, and generators by using this method.

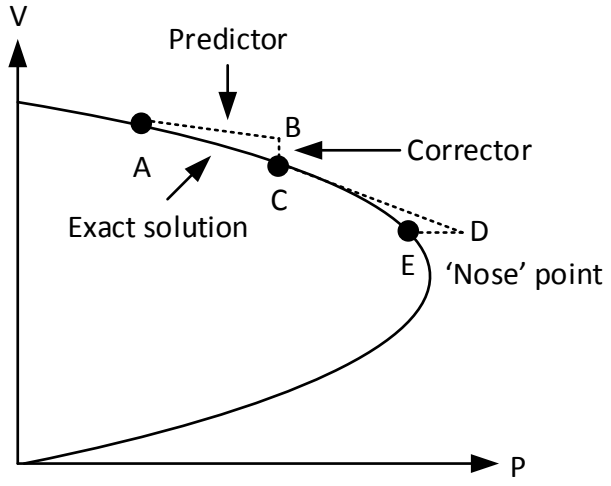


Figure 2. Calculations of CPF.

1.3.3 Singular Value Decomposition (SVD)

As defined in [14], singular value decomposition is generally used to determine the rank of a matrix **A**. The rank of the matrix **A** is equal to number of non-zero singular values of this matrix.

$$\mathbf{A} = \mathbf{LMN}^T = \sum_{i=1}^{k} m_i l_i n_i^t \tag{1-3}$$

where, **L** and **N** are $k \times k$ orthonormal matrices. **M** is an $k \times k$ diagonal matrix, and the diagonal elements of **M** are the singular values. This minimum singular value corresponds to the critical mode. If the minimum singular value is zero, then the matrix **A** is singular.

The application of singularity of the power flow Jacobian matrix as an indicator of steady-state stability limit is discussed in [15] [16]. This method is similar in nature to the modal analysis method. It works on the same reduced Jacobian matrix (J_R). It has been widely utilized for the power systems to obtain a decomposition of the Jacobian matrix.

The minimum singular value gives a mathematical measure of the distance between the studied operating point and the instability point. A fast algorithm for calculation of the minimum singular value has also been proposed in [17] to improve the computational speed of this method. As expected, the minimum singular value is an indicator for the steady-state stability limit. Therefore, the minimum eigenvalue provide similar information for voltage stability analysis.

1.3.4 Voltage Sensitivity Method

By using sensitivity analysis techniques, the relationship between various system states, controls, and dependent variables can be studied. Many sensitivity studies are utilized for identifying the voltage stability conditions [18] [19]. The sensitivities of load voltages to reactive powers and the sensitivities of the total reactive power generation to the reactive loads are proposed in [20] and [21]. A general formula was derived in [22] in order to obtain the sensitivity of the loadability margin to parameters. It was extended and applied to various parameters in [23].

However, these sensitivity methods cannot provide a measure of the distance from current operating point to the voltage collapse point [24]. However, the assumption that the slack generator will provide the required generation due to any network parameter variation is too strong.

1.3.5 Bifurcation Theory

The bifurcation theory can be applied to many types of stability problem in the power system analysis, such as voltage stability, angle stability and trainset stability.

Therefore, bifurcation analysis is an very important approach to analyze the power system stability [25] [26].

The dynamics of the power system is described by differential and algebraic equations.

$$\begin{cases} \dot{x} = f(x, y, \zeta) \\ 0 = g(x, y, \zeta) \end{cases} \tag{1-4}$$

where x is the dynamic state vector, y is the vector of the algebraic variables (complex node voltages) and ξ is a scalar parameter for loads. Assuming that there is an equilibrium point (x_0, y_0, ξ_0) for a given ξ_0, with $\Delta x=(x-x_0)$ and $\Delta y=(y-y_0)$, the linearized system becomes

$$\begin{cases} \Delta\dot{x} = J_{fx}\Delta x + J_{fy}\Delta y \\ 0 = J_{gx}\Delta x + J_{gy}\Delta y \end{cases} \tag{1-5}$$

where J_{fx}, J_{fy}, J_{gx}, J_{gy} are the Jacobian sub-matrices containing the partial derivatives with respect to the state variables. So, the dynamic Jacobian matrix J_{dyn} can be defined as:

$$J_{dyn} = \begin{vmatrix} J_{fx} & J_{fy} \\ J_{gx} & J_{gy} \end{vmatrix} \tag{1-6}$$

The eigenvalues of the dynamic Jacobian matrix can be derived. As the dynamic system moves from one equilibrium point to the others when ξ varies, the eigenvalue trajectories in complex plane may have three different ways:

1. Saddle Node Bifurcation (SNB): a real eigenvalue crosses the origin along the real axis. The number of equilibrium points changes and the loss of voltage stability is of an aperiodic type.

2. Hopf Bifurcation (HB): two complex eigenvalues cross the imaginary axis. The loss of voltage stability is of an oscillatory type, and the Hopf bifurcation gives a pair of purely imaginary eigenvalues.
3. Singularity Induced Bifurcation (SIB): a real eigenvalue moves from the left to the right complex half-plane through the infinity point. In this bifurcation case, the Jacobian matrix will be singular.

SNB is a static bifurcation and happens at the maximum loadability. HB and SIB are dynamic bifurcations and may occur before the saddle node bifurcation. The bifurcation analysis generally assumes the parameters to be slowly varying, so sudden or large disturbances in a power system cannot be studied using bifurcation analysis method.

1.3.6 Dynamic Simulation Analysis

Dynamic simulation analysis conducts time-domain simulation to provide the stability of the system which involves nonlinear differential equations as well as regular algebraic equations. It captures the actual dynamic characteristics of the system without any approximation or linearization.

Dynamic simulation analysis provides the operators with the system status of "*what-if*" scenarios, one critical contingency influencing the system strongly with high occurrence probability of the voltage collapse. The accuracy can be influenced by:

1. The accuracy of the system models largely impacts the creditability of the analysis results. The dynamic simulation relies on the accurately modelling of system components, such as generators, transformers, transmission lines and loads.

2. To simulate the predefined contingencies using the dynamic simulation analysis, an accurate steady state solution has to be provided by the state estimator. The solution needs to represent the current operation point. During some heavily stressed conditions, the converged state estimation results may not be found.

3. Since the voltage stability analysis results have to be provided in an online environment. The high computational speed is one of the critical criteria to meet these demand. For a certain power system models, there might be thousands of contingencies exist, but with the current limited computational resources, we have to selected some of the contingencies to be simulated, and it is impossible to cover all the contingencies. Thus, this method requires the operators to have abundant experiences about the power grid in order to select the contingencies with high likelihood to happen and cause extreme status. However, as it is known, all the components in the power grid vary with uncertainties all the time. It will be impossible for the operators to know all the new operation conditions only based on their experiences. Therefore, new patterns of the system variation introduces a unpredictable complexity which provides the operators with no tools to deal with which makes the system prone to enter a critical status with high likelihood of instability.

All of these factors are challenging the accuracy and reliability of the voltage stability assessment method when we are utilized the dynamic simulation analysis. The

high computational burden and the lack of accuracy could provide the operators with wrong information to make wrong decision, thus push the system to be in danger.

1.4 Measurement-based Voltage Stability Assessment

Many countries are deploying synchronized phasor measurement units (PMUs) on transmission systems to provide wide-area measurements for real-time stability monitoring. That leads to more interests in developing measurement-based VSA methods to directly assess voltage stability from measurements on monitored buses [27-53].

1.4.1 Thevenin Equivalent (TE) based Voltage Stability Indictor

A family of measurement-based methods is based on Thevenin's Theorem: local measurements at the monitored load bus or area are used to estimate a TE approximating the rest of the system, i.e., a voltage source connected through a Thevenin impedance; the power transfer to the monitored load reaches its maximum when that Thevenin impedance has the same magnitude as the load impedance [29-31].

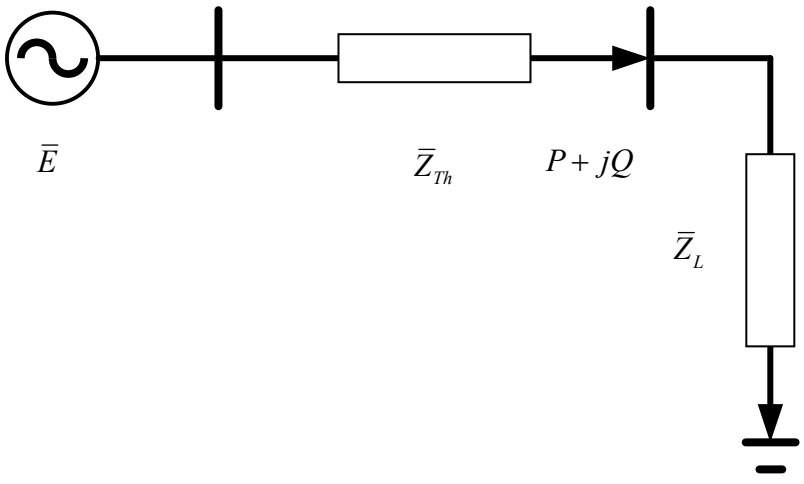


Figure 3. Thevenin equivalent for 2-bus system.

The maximum power transfer to the load in the electric circuit shown in Figure 3 occurs when

$$\left|\bar{Z}_L\right| = \left|\bar{Z}_{Th}\right| \tag{1-7}$$

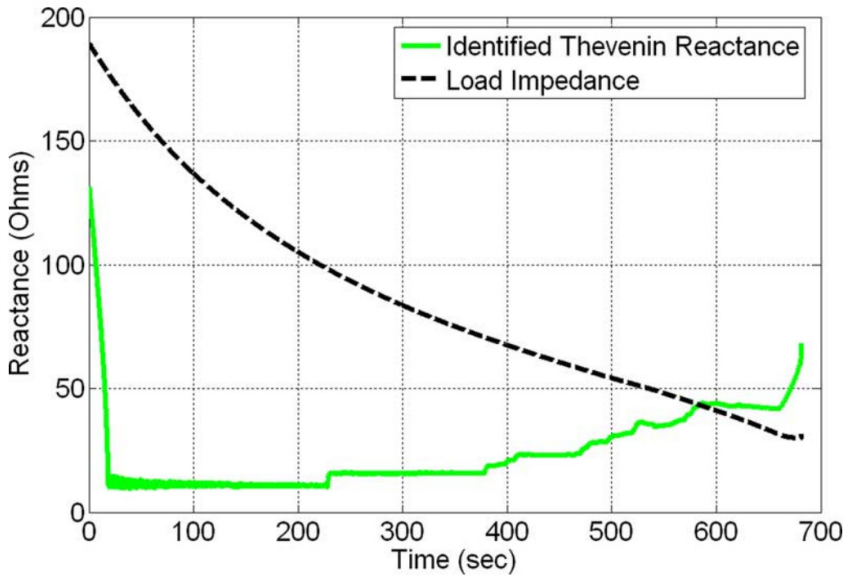


Figure 4. Thevenin reactance and load impedance.

Based on a TE, voltage stability indices can be obtained [32], [33]. Multiple such equivalents may together be applied to multiple tie lines of a load area [34]. For practical applications, paper [35] demonstrates a TE-based method on realistic EHV network, and some other works consider load tap changers and over-excitation limiters in their models for better detection of voltage instability [36-38]. Influences from system-side changes and measurement errors on TE estimation are concerned in [39]. The equivalent circuit considering HVDC integrated wind energy is studied in [40].

Basically, a TE-based method works satisfactorily on a radially-fed load bus or a transmission corridor, and its computational simplicity makes it suitable for real-time application. Paper [41] improves the TE estimation for a load area to tolerate better the fluctuations in voltage phase angles and power factors measured at boundary buses.

1.4.2 Coupled Single-port Equivalent-based Method

Some research efforts have been on how to extend the application of the TE to a broader transmission system, e.g., the coupled single-port circuit or the channel components transform [42-45].

The multi-port network can be modeled as shown in Figure 5. All the generators and load buses are brought outside of the network. The transmission network is converted to an equivalent impedance matrix.

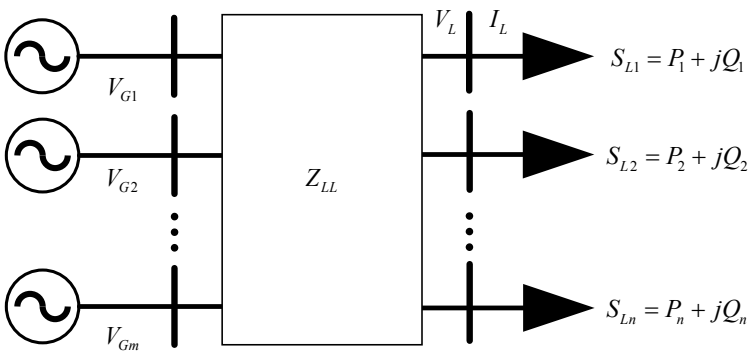


Figure 5. Multi-port network system model.

Then, the multi-port power system can be described by

$$\begin{bmatrix} -\mathbf{I}_L \\ \mathbf{0} \\ \mathbf{I}_G \end{bmatrix} = \mathbf{Y}\begin{bmatrix} \mathbf{V}_L \\ \mathbf{V}_T \\ \mathbf{V}_G \end{bmatrix} = \begin{bmatrix} \mathbf{Y}_{LL} & \mathbf{Y}_{LT} & \mathbf{Y}_{LG} \\ \mathbf{Y}_{TL} & \mathbf{Y}_{TT} & \mathbf{Y}_{TG} \\ \mathbf{Y}_{GL} & \mathbf{T}_{GT} & \mathbf{Y}_{GG} \end{bmatrix}\begin{bmatrix} \mathbf{V}_L \\ \mathbf{V}_T \\ \mathbf{V}_G \end{bmatrix} \tag{1-8}$$

where the **Y** matrix is the system admittance matrix, **V** and **I** stand for the voltage and current vectors, and the subscript **L**, **T** and **G** represent load bus, tie bus, and generator bus, respectively. Eliminate the tie buses:

$$\begin{aligned} \mathbf{V}_L &= \mathbf{K}\mathbf{V}_G - \mathbf{Z}_{LL}\mathbf{I}_L \\ \mathbf{Z}_{LL} &= (\mathbf{Y}_{LL} - \mathbf{Y}_{LT}\mathbf{Y}_{TT}^{-1}\mathbf{Y}_{TL})^{-1} \\ \mathbf{K} &= \mathbf{Z}_{LL}(\mathbf{Y}_{LT}\mathbf{Y}_{TT}^{-1}\mathbf{Y}_{TG} - \mathbf{Y}_{LG}) \end{aligned} \tag{1-9}$$

Where **K** is an $n \times m$ matrix obtained from system admittance matrix **Y**, and $\mathbf{Z}_{LL}$ is an $n \times n$ impedance matrix. From (1-9), for load bus j, we can obtain

$$\begin{aligned} V_{Lj} &= E_{eqj} - Z_{eqj}I_{Lj} - E_{coupled-j} \\ Z_{eqj} &= Z_{LLjj} \\ E_{eqj} &= [\mathbf{K}\mathbf{V}_G]_j \\ E_{coupled-j} &= \sum_{i=1, i\neq j}^{n} Z_{LLji}I_{Li} \end{aligned} \tag{1-10}$$

where Z_{eqj} is the Thevenin impedance of the network at bus j, again without the inclusion of the other loads. The circuit corresponding to (1-10) is shown in Figure 6. This is a single-port network and it can be applied to all load buses. Using this model, a power system can be broken down into a set of single-port circuits that have the impact of other loads included explicitly.

This concept consists in decoupling a mesh power grid into an individual equivalent single-port circuit coupled with an additional impedance. Under a proportional-increase

load scenario, VSI at each load bus can be obtained by individual TE circuit. However, it may yield underestimations if loads are not proportionally increasing.

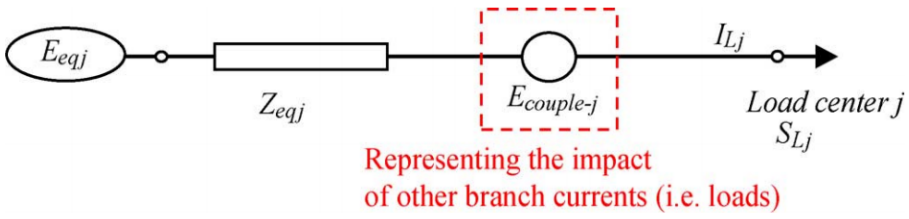


Figure 6. Coupled single-port system equivalent.

1.4.3 Voltage Instability Load Shedding (VILS)

EPRI has been conducting research projects to develop new methods using PMU data to estimate the contingency-independent voltage stability indices and margins in an online environment. In addition, the operators will utilize the calculation results of the stability analysis to monitor the current stability of the system, plan the remedial control action, and test the effectiveness of the control strategies.

In 2006, a measurement-based method for voltage stability monitoring and control at a single load bus has been proposed by EPRI with the name “Voltage Instability Load Shedding” (VILS) [46]. This method is contingency-independent, and the calculated results could be represented as the active/reactive power transferred to the local bus. The operators could utilize the provided real-time stability information to do the load shedding in order to prevent the system from collapse.

During the 2003 voltage collapse event at TVA's Philadelphia, Mississippi substation, EPRI implemented and validated this method by collecting the Digital Fault Recorder (DFR) data. EPRI has also validated this method using Phasor Measurement Unit (PMU) data collaborated with New York Power Authority. These case studies tell the advantages as follows:

1. Accurately estimate the voltage stability margins;
2. Provide the load shedding amount to the operators;
3. Assess a dynamic single voltage stability threshold for the voltage level of the monitored bus.

This method can also be utilized in the wide-area, since sometimes the voltage stability is not only a local issue, and it spreads out to a wide-area problem. To handle such a problem, a load area (center) will be monitored. Since the generation in the local area cannot meet the requirement of all the local loads, the transmission lines at the interface will all have the same pattern which is transmitting power into the load area.

When the PMU technology has been widely used in the power system, its good features appear to the researchers. It can be utilized to provide high resolution measurements with high accuracy, including the voltage phasor, current phasor, active power and reactive power. With PMU technology supporting, the researcher can propose many algorithms for the voltage stability monitoring and control.

1.4.4 Measurement-based Voltage Stability Assessment (MBVSA)

Some other efforts tested MBVSA methods on load areas as it is shown in Figure 7.

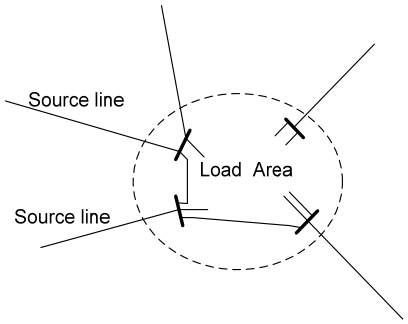


Figure 7. MBVSA on a load area.

References [47] and [48] apply the MBVSA method to a load center area, which is able to continuously calculate real-time contingency-independent voltage stability margin for a load pocket area using synchronized voltage and current measurements taken at its all boundary buses. No simulation is needed by this method in estimating voltage stability margin, so the method is fast and independent of contingency scenarios and simulation models. The calculated voltage stability margin can be expressed as the total amount of real or reactive power (i.e. the security margin) that can be further transferred through the interface buses without causing any voltage stability problem. Therefore, it can be used as a real-time indicator of the area's overall voltage stability level. Once the load area is found short of voltage stability margin (i.e. below a prescribed threshold), the shortfall directly indicates the amount of MW or MVar reserve needed to be switched in or the amount of

load needs to be shed within that area to avoid voltage instability. Thus, the MBVSA method can identify real time control strategies.

Past EPRI research projects have validated the stability margins calculated by this method for the case where PMUs or other measurements are available at interface buses of a monitored load pocket area. EPRI collaborated with Entergy to examine this method on their Western Region in 2008, and are demonstrating that method at Entergy using real-time PMU data from the Western Region supported by a DOE Smart Grid Investment Grant project [49].

1.4.5 TE-based Hybrid VSA Method for *n*-1 Conditions

Paper [50] proposes a measurement- and model-based hybrid approach to assess voltage stability under *n*-1 contingencies. This method utilizes a transformation as shown in Figure 8 to get the voltage approximation without doing the power flow calculation.

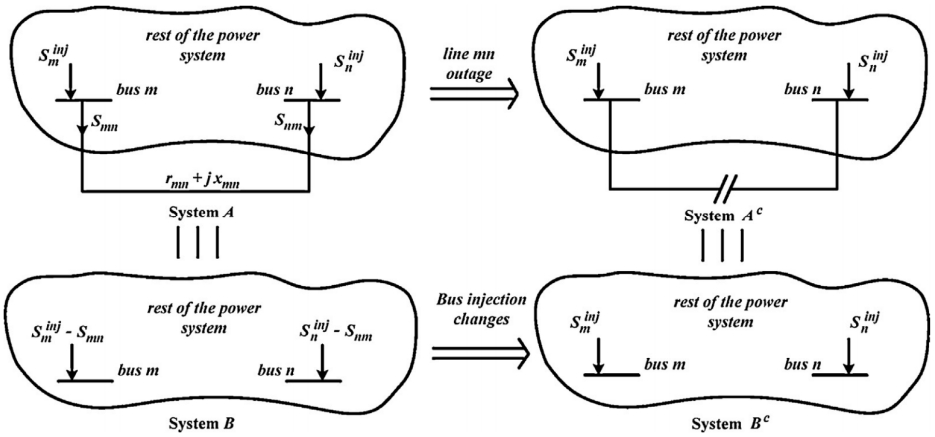


Figure 8. Proposed transformation.

To apply this method for voltage control, a Loading Margin Sensitivity (LMS) method has been proposed based on system equilibrium equations near bifurcation [51], [52].

1.4.6 An Adaptive Three-bus Power System Equivalent

A TE-based method may not provide accurate voltage stability margin for each of multiple tie lines together feeding a load area if it merges those tie lines as done in [47] and [48]. As illustrated in [53], we have proposed an adaptive three-bus power system equivalent shown in Figure 9 to improve the accuracy of TE-based method.

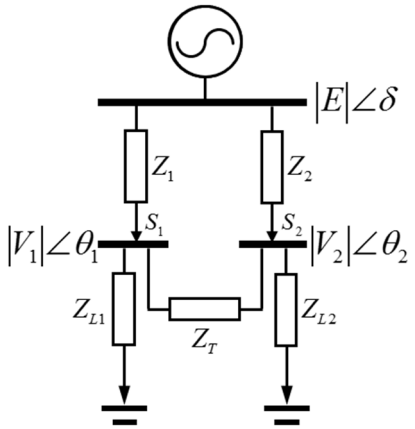


Figure 9. 3-bus System.

As shown in Figure 10, even when estimating the total transfer limit of multiple tie lines, the TE is accurate only if the boundary buses through which those tie lines feed the load area are strongly connected (as indicated by the left figure) and the external system is coherent to be regarded as a single voltage source. Those are two necessary conditions for

merging tie lines and boundary buses and developing a meaningful TE. If connections between boundary buses are weak (as shown by the right figure), when the load of the area gradually increases, tie lines may reach their power transfer limits at different time instants. In other words, voltage instability may initiate near one of boundary buses and then propagate to the rest of the area. Thus, only monitoring the total power transfer limit of all tie lines using a single TE may delay the detection of voltage instability.

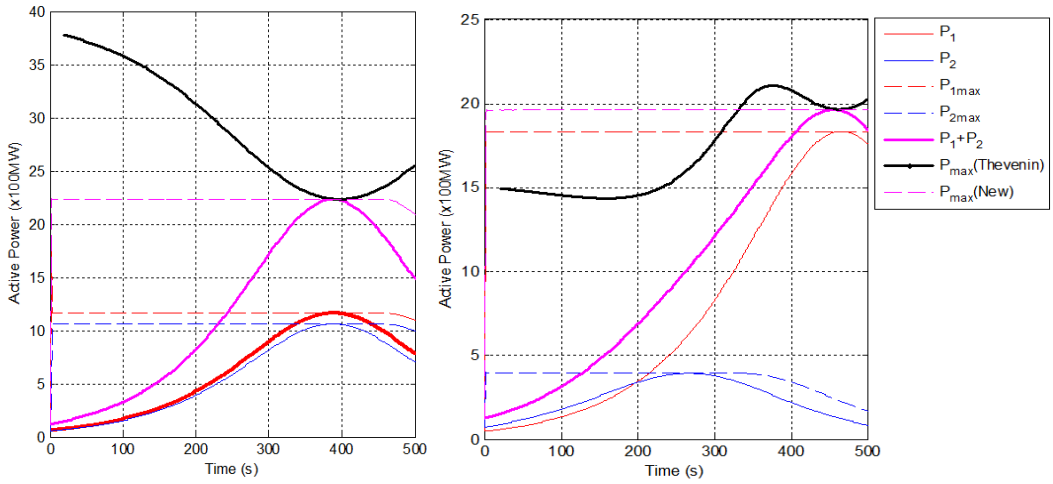


Figure 10. Line flow limits for tight (a) and weak (b) interconnections between two buses.

1.5 Contribution of this Work: Hybrid Real-time Voltage Stability Assessment

A hybrid simulation/measurement-based framework for online power system stability/security assessment combining the strengths and features of simulation-based and

measurement-based approaches will be valuable to provide real-time situational awareness on available operating margins against major stability problems.

This thesis proposes a hybrid VSA approach to real-time voltage stability monitoring and control for Load Areas. The theory is likely to bring new insights into the interactions of various quantities measured by PMUs and thus leads to the establishment of a new framework for PMU applications. Specifically, the contributions of this work can be summarized into the following five aspects.

1. Propose a new N+1 buses equivalent system.

For most of the MBVSA methods, Thevenin equivalent has been widely used and lots of improvements have been made on it. However, simplicity is a both good feature and bad feature. The simplicity of the TE makes it easy to use and largely reduce the computation burden, but some useful information has been eliminated. With the N+1 equivalent modeling the individual tie lines and their coupling relationship, the new MBVSA can provide the individual voltage stability limits with higher accuracy. This method identifies all the parameters of the equivalent in real time, and then solve the limit as an analytical function. This process makes the new method more accurate than TE method.

2. Assess the voltage stability margins under an n-1 contingency.

Most of the measurement-based method are not able to provide the margins under an n-1 contingency due to their oversimplified model. However, with the N+1 equivalent model containing the parameters obtained by network transformation, this network

transformation enables the ability of the new method for foreseeing the *n*-1 stability margins.

3. Reduce the computation burden for the *n*-1 simulation study.

For a system with thousands of transmission lines, the *n*-1 study needs thousands of simulation scenarios which will be very difficult to be conducted online. The new method gives a criticality ranking in terms of the active power margin so as to eliminate the non-critical contingencies and largely reduce the computation burden.

4. Offer a framework to provide stability margins and preventive control actions.

In this practical framework, the MBVSA method not only help reducing the computation burden, but also triggering the preventive control actions. Thus, a complimentary monitoring and control framework can be implemented by taking the advantages of both measurement-based and simulation-based methods.

5. Implement the MBVSA method and closed-loop control scheme on a physical power system - the CURENT Hardware Test Bed (HTB) system.

This new approach has been implemented on a power electronic convertor-based power system. In this physical power system, the measurements error/noise and communication delay are inevitable, so it further validates the effectiveness and robustness of the new approach.

CHAPTER 2

N+1 BUSES EQUIVALENT SYSTEM

2.1 Introduction

In this chapter, the TE will be extended and generalized for voltage stability monitoring to an *N*+1 buses equivalent system such that a unified MBVSA method based on the identification of this new equivalent is proposed. In that sense, the TE-based method can be considered the special implementation of this new unified MBVSA approach that is applied better to a radial network.

Compared to the TE, this new equivalent has N buses interconnected to represent a load area with N boundary buses and one voltage source representing the external system. Thus, the TE is its special case with *N*=1. By modeling boundary buses separately for a load area, a new method based on this new equivalent is developed and demonstrated in this chapter to calculate power transfer limits at individual boundary buses.

This chapter introduces the new method in detail, including the description of the *N*+1 buses equivalent system, its parameter identification and analytical solutions of power transfer limits of its tie lines. In addition, an online scheme to implement the new method is presented. A simple 4-bus power system is utilized to illustrate the advantages of the new method over a traditional TE-based method, and then the new method is validated on the NPCC 48-machine, 140-bus power system.

For a load area fed by *N* tie lines, voltage instability may be a concern with its boundary buses when power flows of those tie lines approach to their transfer limits. As

shown in Figure 11, an N+1 buses equivalent system is proposed to model those boundary buses and tie lines while reducing the network details both inside and outside of the load area. Assume the external system to be strongly coherent without any angular stability concern. Thus, it is represented by a single voltage source with phasor $\overline{E}$ connected by N branches with impedances $\overline{z}_{E1} \sim \overline{z}_{EN}$ (representing N tie lines) to N boundary buses, respectively. Each boundary bus is monitored and connects an equivalent load with impedance $\overline{z}_{ii}$ modeling the portion of load seen from that bus. Connection between any two boundary buses i and j is modeled by impedance $\overline{z}_{ij}$. The power transfer limit of each tie line is a function of $N(N-1)/2+2N+1$ complex parameters of that equivalent system including voltage phasor $\overline{E}$, N tie-line impedances $\overline{z}_{Ei}$'s, $N(N-1)/2$ transfer impedances $\overline{z}_{ij}$'s and N load impedances $\overline{z}_{ii}$'s.

Let $\overline{S}_i = P_i + jQ_i$ denote the complex power fed to boundary bus i and let $\overline{V}_i$ denote the bus voltage phasor. Using synchronized measurements on $\overline{S}_i$ and $\overline{V}_i$, all parameters of the equivalent can be identified online (e.g., every 0.1-1s) using the latest measurements of a sliding time window. Section 2.2 and 2.3 present the algorithms for estimating the parameters of the external system (i.e., $\overline{E}$ and $\overline{z}_{Ei}$) and the load area (i.e., $\overline{z}_{ii}$ and $\overline{z}_{ij}$) and then derives the analytical solution of each tie-line power transfer limit.

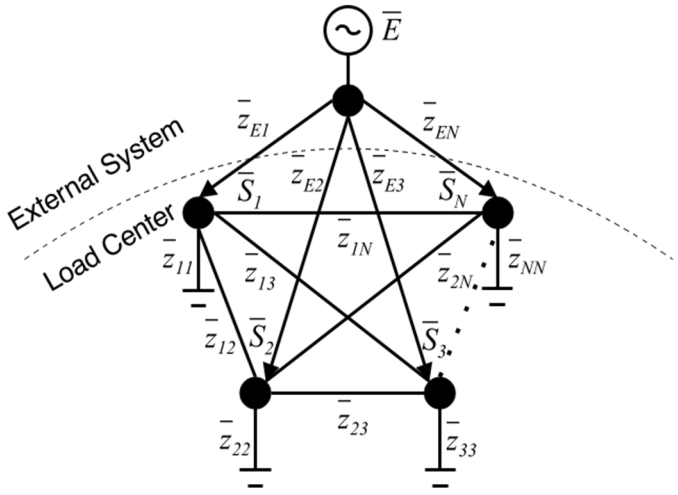


Figure 11. *N*+1 buses equivalent.

2.2 System Parameter Estimation

2.2.1 Identification of the External System Parameters

Assume that the sliding time window contains *K* measurement points. The external system parameters are assumed to be constant during the time window and hence are estimated by solving the following optimization problem. Nodal power injection equation (2-1) holds at each measurement point k of the time window.

$$\overline{S}_i(k) = \left(\frac{\overline{E} - \overline{V}_i(k)}{\overline{z}_{Ei}}\right)^* \times \overline{V}_i(k) \quad k=1\sim K \tag{2-1}$$

where $\overline{S}_i(k) = P_i(k) + jQ_i(k)$ and $\overline{V}_i(k) = V_i(k)\angle\theta_i(k)$ are respectively the received complex power and voltage phasor at boundary bus *i* at time point *k*. The magnitude of $\overline{E}$, denoted by *E*, can be estimated from measurements at each boundary bus *i*, whose estimation error is

$$e_i^{ex}(k) = E - \left| (P_i(k) - \mathrm{j}Q_i(k))(r_{Ei} + jx_{Ei}) + (V_i(k))^2 \right| / V_i(k) \tag{2-2}$$

The optimization problem in (2-3) computes the optimal estimates of E, r_{Ei} and x_{Ei}.

$$\min J^{ex} = \sum_{k=1}^{K}\sum_{i=1}^{N} \frac{\omega_e}{N}\left[e_i^{ex}(k) \right]^2 + \sum_{i=1}^{N} \omega_z \left(\frac{r_{Ei}}{r_{Ep}} - 1 \right)^2 + \sum_{i=1}^{N} \omega_z \left(\frac{x_{Ei}}{x_{Ep}} - 1 \right)^2$$

$$s.t. \quad E > 0, \quad r_{Ei} \geq 0 \tag{2-3}$$

The 1st term summates the estimation errors of E for all buses and all time points. The 2nd and 3rd terms respectively summate normalized differences in r_{Ei} and x_{Ei} between the estimates for the current and previous time window. ω_e and ω_z are weighting factors respectively for variances of E and $\bar{z}_{Ei}$ over the time window. For instance, if the network topology of the external system does not change, $\bar{z}_{Ei}$ will be constant. Thus, there should be $\omega_z > \omega_e$ to allow more changes in E. The Sequential Quadratic Programming (SQP) method is used to solve the optimization problem in (2-3) [54].

The above optimization problem for the external system is actually a non-convex problem, so it needs to select good initial values for the external system parameters. As long as the initial values are in a neighborhood of the optimum that is considered as the true solution, the SQP method can make sure to converge to that solution. However, the problem does have multiple local optima. In practice, the initial values of external system parameters for optimization are determined as follows: at the beginning when the new measurement-based method is performed or whenever a major disturbance, e.g., a line outage and a generator outage, is detected on the external system, the Least Square method

is applied to the *K* data points of the current time window to estimate the parameters as new initial values; otherwise, the new method selects initial values from the optimization results of the previous time window. Because of the non-convex nature of this optimization problem, if the initial values selected at the beginning are far from the true solution, the optimization may converge to a different solution with errors in parameter estimation and consequently cause inaccurate transfer limits at the end. Those errors may last until the next time the Least Square method is performed to re-create new initial values. Later in a case study on the NPCC system, the results from different initial values with errors intentionally added are compared. In practice, the Least Square method may be performed at a certain frequency, e.g., every a few minutes, even if a major disturbance is not detected.

2.2.2 Identification of the Load Area Parameters

Load area parameters include load impedance $\bar{z}_{ii}$ and transfer impedance $\bar{z}_{ij}$ (*i* and *j*=1~*N*), whose admittances are $\bar{y}_{ii}$ and $\bar{y}_{ij}$. In each time window, assume constant $\bar{y}_{ij}$ if there is no topology change in the load area, and allow $\bar{y}_{ii}$ to change. From power flow equations,

$$\bar{y}_{ii}(k) = \frac{\bar{S}_i^*(k) - \sum_{j=1\sim N, j\neq i} \left[V_i^2(k) - \bar{V}_i^*(k)\bar{V}_j(k) \right] \bar{y}_{ij}}{V_i^2(k)} \tag{2-4}$$

A window of *K* data points has *NK* values of $\bar{y}_{ii}$ and *N*(*n-1*)/2 values of $\bar{y}_{ij}$ to be estimated. Thus, there are totally $N^2 - N + 2NK$ real parameters to estimate. *K* data points can provide 2*NK* nodal power injection equations in real realm. Since $N^2 - N + 2NK > 2NK$, there are insufficient equations to solve all parameters. In each window, if we may assume

a constant power factor for each $\bar{y}_{ii}$, its conductance g_{ii} and susceptance b_{ii} of $\bar{y}_{ii}$ at two adjacent time points will satisfy

$$\frac{g_{ii}(k-1)}{b_{ii}(k-1)} = \frac{g_{ii}(k)}{b_{ii}(k)} \quad (k=2\sim K) \tag{2-5}$$

Thus, K-1 more equations are added to each bus and the entire load area needs to solve $3NK$-N equations. From equality (2-6), there is K=N.

$$N^2 - N + 2NK = 3NK - N \tag{2-6}$$

It means that each time window needs to have at least N data points to be able to solve all parameters of the load area. For instance, for load areas with N=2, 3 and 4 boundary buses, we need at least the same numbers of data points to solve 10, 24 and 44 unknowns, respectively.

From (2-4), g_{ii} and b_{ii} are both functions of $\bar{y}_{ij}$'s ($i \neq j$). An error index on (2-5) is defined as

$$e_i^{in}(k) = g_{ii}(k-1)b_{ii}(k) - g_{ii}(k)b_{ii}(k-1) \tag{2-7}$$

The second optimization problem is formulated as (2-8) for estimating load area parameters by minimizing three weighted summation terms. g_{ij} and b_{ij} are estimated conductance and susceptance of $\bar{y}_{ij}$; the 2nd and 3rd terms respectively summate their normalized differences from the previous time window; ω_{pf} and ω_y are the weighting factors respectively for variances of the power factor and $\bar{y}_{ij}$ over the time window.

$$\min J^{in} = \sum_{k=2}^{K}\sum_{i=1}^{N}\frac{\omega_{pf}}{N}\left[e_i^{in}(k)\right]^2 + \sum_{\substack{i,j=1 \\ i\neq j}}^{N}\omega_y\left(\frac{g_{ij}}{g_{ijp}}-1\right)^2 + \sum_{\substack{i,j=1 \\ i\neq j}}^{N}\omega_y\left(\frac{b_{ij}}{b_{ijp}}-1\right)^2$$

$$s.t. \quad g_{ij} > 0 \tag{2-8}$$

The SQP method is also used to solve all $\bar{y}_{ij}$'s for each time window. Then, calculate load admittance $\bar{y}_{ii}$ directly by (2-4).

For this second optimization on estimation of load area parameters, initial values of g_{ij} and b_{ij} are also required, which can be obtained directly from the reduced bus admittance matrix about the load area by eliminating all buses except boundary buses.

2.3 Solving the Power Transfer Limit of Each Tie Line

From real-time estimates of equivalent parameters, the active power transfer limit of each tie line can be solved analytically as a function of equivalent parameters.

The admittance matrix of the load area of the equivalent system is given in (2-9), where $\bar{Y}_{ij} = \bar{Y}_{ji} = -\bar{y}_{ij}$ and $\bar{Y}_{ii} = \sum_{j=1}^{N} \bar{y}_{ij}$.

$$\mathbf{Y} = \begin{bmatrix} \bar{Y}_{11} & \cdots & \bar{Y}_{1i} & \cdots & \bar{Y}_{1N} \\ \vdots & \ddots & & & \vdots \\ \bar{Y}_{i1} & & \bar{Y}_{ii} & & \bar{Y}_{iN} \\ \vdots & & & \ddots & \vdots \\ \bar{Y}_{N1} & \cdots & \bar{Y}_{Ni} & \cdots & \bar{Y}_{NN} \end{bmatrix} \tag{2-9}$$

Let $\mathbf{Y_E}$ be a column vector about all admittances $\bar{y}_{Ei} = 1/\bar{z}_{Ei}$ (i=1~N) and $\mathbf{Y_E^D}$ be a diagonal matrix created from $\mathbf{Y_E}$, i.e.,

$$\mathbf{Y_E} = [\bar{y}_{E1} \quad \bar{y}_{E2} \quad \cdots \quad \bar{y}_{EN}]^T \tag{2-10}$$

$$\mathbf{Y_E^D} = diag(\mathbf{Y_E}) = \begin{bmatrix} \bar{y}_{E1} & & 0 \\ & \ddots & \\ 0 & & \bar{y}_{EN} \end{bmatrix} \tag{2-11}$$

A vector about the injected currents satisfies

$$\mathbf{I} = \overline{E}\mathbf{Y_E} - \mathbf{Y_E^D V} \tag{2-12}$$

where $\mathbf{V} = [\overline{V}_1 \quad \overline{V}_2 \quad \cdots \quad \overline{V}_N]^T$. Then, there is

$$\mathbf{V} = \overline{E}(\mathbf{Y} + \mathbf{Y_E^D})^{-1}\mathbf{Y_E} = \overline{E}\,\frac{\mathrm{adj}(\mathbf{Y} + \mathbf{Y_E^D})}{\det(\mathbf{Y} + \mathbf{Y_E^D})}\mathbf{Y_E} \tag{2-13}$$

For simplicity, let α_i denote the i-th element of $\mathrm{adj}(\mathbf{Y} + \mathbf{Y_E^D})\mathbf{Y_E}$ and let $\gamma = \det(\mathbf{Y} + \mathbf{Y_E^D})$. There is

$$\overline{V}_i = \overline{E}\alpha_i / \gamma \tag{2-14}$$

The complex power transferred on each tie line is a function of elements of $\mathbf{Y}$, $\overline{E}$ and $\mathbf{Y_E}$.

$$\mathbf{S} = [\overline{S}_1 \quad \overline{S}_2 \quad \cdots \quad \overline{S}_N]^T = (\overline{E}\mathbf{Y_E^D} - \mathbf{V}^{\mathbf{D}}\mathbf{Y_E^D})^* \mathbf{V} \tag{2-15}$$

where $\mathbf{V^D} = diag(\mathbf{V})$. If changes on the external system are ignored, each complex power is a function of load admittances, i.e.

$$\overline{S}_i(\overline{y}_{11}, \cdots, \overline{y}_{NN}) = (\overline{E}^* \overline{y}_{Ei}^* - \overline{y}_{Ei}^* \overline{V}_i^*)\overline{V}_i = \left|\overline{E}\right|^2 (\overline{y}_{Ei}^* - \overline{y}_{Ei}^* \frac{\alpha_i^*}{\gamma^*})\frac{\alpha_i}{\gamma} \tag{2-16}$$

$$P_i(\overline{y}_{11}, \cdots, \overline{y}_{NN}) = \left|\overline{E}\right|^2 \mathrm{Re}\left[(\overline{y}_{Ei}^* - \overline{y}_{Ei}^* \frac{\alpha_i^*}{\gamma^*})\frac{\alpha_i}{\gamma} \right] \tag{2-17}$$

Based on the aforementioned constant power factor assumption over a time window for each load, P_i is a function of all load admittance magnitudes, i.e. y_{jj} (j=1~N). Its maximum $P_{i,j}^{\mathrm{Max}}$ with respect to the change of y_{jj} at bus j is reached when

$$\frac{\partial P_i(y_{11}, \cdots, y_{NN})}{\partial y_{jj}} = 0 \qquad i, j = 1 \sim N \tag{2-18}$$

If an analytical solution of y_{jj} is obtained from (2-18) as a function of equivalent parameters, an analytical expression of $P_{i,j}^{\text{Max}}$ can be derived by plugging the solution of y_{jj} into (2-17). $P_{i,i}^{\text{Max}}$ with $i=j$ represents the maximum active power transfer to bus i with only the local load at bus i varying; $P_{i,j}^{\text{Max}}$ with $j\neq i$ represents the maximum active power transfer to bus i with only the load at another bus j varying.

For a general N+1 buses equivalent, the analytical solution of $P_{i,j}^{\text{Max}}$ can be obtained by solving a quadratic equation. The proof based on (2-18) is given in the Appendix.

Theorem: an analytical solution of $P_{i,j}^{\text{Max}}$ can be obtained by solving a quadratic equation.

Proof: As defined above, α_i represents the i-th element of $\text{adj}(\mathbf{Y}+\mathbf{Y}_{\mathbf{E}}^{\mathbf{D}})\mathbf{Y}_{\mathbf{E}}$ and $\gamma=\det(\mathbf{Y}+\mathbf{Y}_{\mathbf{E}}^{\mathbf{D}})$. It is easy to know that they are both linear complex functions of the load admittance $\overline{y}_{jj}=y_{jj}e^{j\phi}$, where y_{jj} and ϕ are the magnitude and angle of $\overline{y}_{jj}$. So they can be represented as $\gamma=d_{j1}y_{jj}e^{j\phi}+d_{j2}$ and $\alpha_i=d_{j3}y_{jj}e^{j\phi}+d_{j4}$, where d_{j1}~d_{j4} are constant complex numbers (note that if $j=i$, y_{jj} does not appear in α_i, so $d_{j3}=0$).

Equation (2-18) becomes

$$\frac{\partial P_i(y_{jj})}{\partial y_{jj}}=\frac{E^2}{|\gamma|^4}\text{Re}\{\overline{y}_{Ei}^{*}[d_{j3}\gamma(\gamma^*)^2-d_{j3}\alpha_i^*\gamma\gamma^*-d_{j3}^*\alpha_i\gamma\gamma^* -d_{j1}\alpha_i(\gamma^*)^2+d_{j1}\alpha_i\alpha_i^*\gamma^*+d_{j1}^*\alpha_i\alpha_i^*\gamma]\}=0 \tag{2-19}$$

where E^2 and $|\gamma|^4=0$. Then, an analytical solution of y_{ii} can be obtained by solving

$$\begin{aligned}&\mathrm{Re}\{\overline{y}_{Ei}^{*}[d_{j3}\gamma(\gamma^{*})^{2}-d_{j3}\alpha_{i}^{*}\gamma\gamma^{*}-d_{j3}^{*}\alpha_{i}\gamma\gamma^{*}\\&-d_{j1}\alpha_{i}(\gamma^{*})^{2}+d_{j1}\alpha_{i}\alpha_{i}^{*}\gamma^{*}+d_{j1}^{*}\alpha_{i}\alpha_{i}^{*}\gamma]\}=0\end{aligned} \tag{2-20}$$

It can be simplified into the form of a quadratic equation:

$$ay_{jj}^{2}+by_{jj}+c=0 \tag{2-21}$$

where

$$\begin{aligned}a=\mathrm{Re}\{&y_{Ei}^{*}[(\left|d_{j1}\right|^{2}d_{j3}d_{j4}^{*}-d_{j1}d_{j2}^{*}\left|d_{j3}\right|^{2})e^{j\phi}\\&+((d_{j1}^{*})^{2}d_{j2}d_{j3}-d_{j1}(d_{j1}^{*})^{2}d_{j4}-d_{j1}^{*}d_{j2}\left|d_{j3}\right|^{2}+\left|d_{j1}\right|^{2}d_{j3}^{*}d_{j4})e^{-j\phi}]\}\end{aligned} \tag{2-22}$$

$$b=\mathrm{Re}\{2\overline{y}_{Ei}^{*}[\left|d_{j1}\right|^{2}\left|d_{j4}\right|^{2}-\left|d_{j2}\right|^{2}\left|d_{j3}\right|^{2}+d_{j1}^{*}\left|d_{j2}\right|^{2}d_{j3}-\left|d_{j1}\right|^{2}d_{j2}^{*}d_{j4}]\} \tag{2-23}$$

$$\begin{aligned}c=\mathrm{Re}\{&y_{Ei}^{*}[(d_{j2}(d_{j2}^{*})^{2}d_{j3}-d_{j1}(d_{j2}^{*})^{2}d_{j4}-\left|d_{j2}\right|^{2}d_{j3}d_{j4}^{*}+d_{j1}d_{j2}^{*}\left|d_{j4}\right|^{2})e^{j\phi}\\&+(d_{j1}^{*}d_{j2}\left|d_{j4}\right|^{2}-\left|d_{j2}\right|^{2}d_{j3}^{*}d_{j4})e^{-j\phi}]\}\end{aligned} \tag{2-24}$$

The closed-form solution of (2-21) can be derived and then plugged into (2-17) to obtain the analytical expression of $P_{i,j}^{\mathrm{Max}}$.

□

As an example, for *N*=3, to solve $P_{1,1}^{\mathrm{Max}}$ and $P_{1,2}^{\mathrm{Max}}$, define

$$\overline{y}_{i}\overset{\mathrm{def}}{=}\overline{y}_{Ei}+\sum_{j=1\sim3}\overline{y}_{ij}\qquad i=1\sim3 \tag{2-25}$$

All involved *d*-constants, d_{11}, d_{12}, d_{13}, d_{14}, d_{21}, d_{22}, d_{23}, and d_{24} are

$$d_{11}=\overline{y}_{2}\overline{y}_{3}-\overline{y}_{23}^{2} \tag{2-26}$$

$$d_{12}=d_{11}(\overline{y}_{E1}+\overline{y}_{12}+\overline{y}_{13})-\overline{y}_{12}^{2}\overline{y}_{3}-\overline{y}_{13}^{2}\overline{y}_{2}-2\overline{y}_{12}\overline{y}_{13}\overline{y}_{23} \tag{2-27}$$

$$d_{13}=0 \tag{2-28}$$

$$d_{14} = d_{11}\bar{y}_{E1} + (\bar{y}_{12}\bar{y}_3 + \bar{y}_{13}\bar{y}_{23})\bar{y}_{E2} + (\bar{y}_{12}\bar{y}_{23} + \bar{y}_{13}\bar{y}_2)\bar{y}_{E3} \tag{2-29}$$

$$d_{21} = \bar{y}_1\bar{y}_3 - \bar{y}_{13}^2 \tag{2-30}$$

$$d_{22} = d_{21}(\bar{y}_{E2} + \bar{y}_{12} + \bar{y}_{23}) - \bar{y}_{12}^2\bar{y}_3 - \bar{y}_{23}^2\bar{y}_1 - 2\bar{y}_{12}\bar{y}_{13}\bar{y}_{23} \tag{2-31}$$

$$d_{23} = \bar{y}_{E1}\bar{y}_3 + \bar{y}_{E3}\bar{y}_{13} \tag{2-32}$$

$$d_{24} = d_{23}(\bar{y}_{E2} + \bar{y}_{12} + \bar{y}_{23}) - \bar{y}_{23}^2\bar{y}_{E1} + \bar{y}_{12}\bar{y}_{23}\bar{y}_{E3} + (\bar{y}_{12}\bar{y}_3 + \bar{y}_{13}\bar{y}_{23})\bar{y}_{E2} \tag{2-33}$$

Note that $\bar{y}_{11}$ does not appear in d_{11}~d_{14} and $\bar{y}_{22}$ does not appear in d_{21}~d_{24}.

This method assumes that each y_{jj} may change individually, so there are N such transfer limits $P_{i,1}^{\text{Max}} \sim P_{i,N}^{\text{Max}}$ for each tie line. By estimating the real-time pattern of load changes, the limit matching best that pattern will be more accurate and selected. Voltage stability margin on a tie line is defined as the difference between the limit and the real-time power transfer.

2.4 Properties of the Power Transfer Limits for the *N*+1 Equivalent Model

A measurement-based N+1 buses equivalent model has been proposed in ref. [55-57] to assess the voltage stability for load areas in real time. For each transmission line connecting the load area and external system, the method provides N power transfer limits by solving the partial derivative with respect to all equivalent impedances. This section provides proofs of the properties of the power transfer limits for transmission line in different load changing scenarios.

Voltage instability for load area fed by multiple interface lines is a major concern for power system operators. A measurement-based real-time N+1 equivalent model has

been proposed to investigate such problems which has the ability to provide the power transfer limits for each individual interface line. The operator will need to monitor all power transfer limits to determine the criticality of the system. In order to uncover the inherent characteristics of these limits, the following properties and their proofs will be addressed.

Figure 12 illustrates the *N*+1 equivalent model for the load area fed by *N* interface lines. Assuming the external system of the load area to be strongly coherent, the external system can be represented by a voltage source $\overline{E}$ connected by *N* branches with admittances $\overline{y}_{E1} \sim \overline{y}_{EN}$ (representing the *N* interface lines) to *N* boundary buses, respectively. Each boundary bus connects an equivalent load, and the connection between any two boundary buses *i* and *j* is modeled by admittance $\overline{y}_{ij}$.

The power transfer limit of each interface line is a function of all the parameters of that equivalent system including the voltage source, the *N* interface line admittances, the transfer admittances and the *N* load admittances. Assuming, the local load admittance is $\overline{y}_{ii}$, in order to analyze the impact from the remote load admittance $\overline{y}_{jj}$, (2-34) can be obtained.

$$P_i(\overline{y}_{ii}, \overline{y}_{jj}) = \left|\overline{E}\right|^2 \mathrm{Re}\left[(\overline{y}_{Ei}^* - \overline{y}_{Ei}^* \frac{\alpha_i^*}{\gamma^*}) \frac{\alpha_i}{\gamma} \right] \tag{2-34}$$

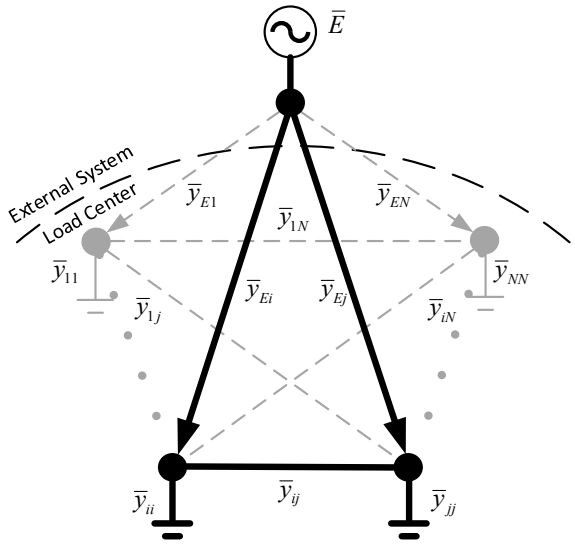


Figure 12. Nodes connection for *N*+1 buses equivalent.

***Property* 1: The limit with respect to the increasing load has less variation than the one with respect to the non-increasing load.**

According to the Theorem in [57], the analytical solution of $P_{i,i}^{\text{Max}}$ can be obtained by solving a quadratic equation $ay_{ii}^2+by_{ii}+c=0$ with respect to y_{ii}. Since the solution of the quadratic equation will be plugging into the (2-34) to get $P_{i,i}^{Max}$, y_{ii} will not appear in $P_{i,i}^{Max}$. Assuming the load increment only happened on the local load, which means y_{ii} is the only parameter changing. So $P_{i,i}^{Max}$ will be constant as y_{ii} will not appear in $P_{i,i}^{Max}$. However, $P_{i,j}^{Max}$ will change as the y_{ii} is one of the variables of $P_{i,j}^{Max}$. Thus, $P_{i,i}^{Max}$ has less variation than $P_{i,j}^{Max}$ when the load on the *i*-th bus is increasing. Due to the similarity, $P_{i,j}^{Max}$ has less variation than $P_{i,i}^{Max}$ when the load on the *j*-th bus is increasing.

***Property* 2: The limit with respect to the local load is larger than the ones with respect to remote loads under the normal operating condition.**

According to Theorem in [57], there are two analytical roots. Suppose that all conductances of the equivalent line are positive and all susceptances of the equivalent line are negative, the root with reasonable physical meaning will be plugging into (2-34). In order to compare the derived analytical expressions $P_{i,i}^{Max}$ and $P_{i,j}^{Max}$, a function $f_\Delta = P_{i,i}^{Max} - P_{i,j}^{Max}$ can be defined to describe the relationship between the two limits. [30] and [34] both show that the load impedance is much larger than the equivalent Thevenin impedance under normal operating condition, and it is almost 20 times larger in [30] and [34]. Since the load admittance is the reciprocal of the load impedance, the polynomial terms in f_Δ involving load admittances can be ignored. Therefore, we have

$$f_\Delta^0 \approx -\frac{1}{2}\frac{|E|^2 B_{Ei}^2}{B_{Ei}+B_{ij}} > 0 \tag{2-35}$$

Equation (2-35) indicates that under the normal operating condition, the limit about local load will be larger than the ones with respect to the remote loads.

As the load is increasing and the system is approaching the "nose" point, in order to reveal the sequence of the limits, two properties about two fundamental load changing directions (local and remote) need to be studied.

***Property* 3: If only local load is increasing, at the "nose" point, $P_{i,i}^{Max} < P_{i,j}^{Max}$, and $P_{i,i}^{Max}$ is reached firstly.**

$P_{i,i}^{Max}$ is fixed since it matches the assumption of the load increasing direction, and all variables in $P_{i,i}^{Max}$ are constant. When P_i reaches its maximum, y_{ii} is the solution of $\partial P_i(y_{ii})/\partial y_{ii} = 0$. Therefore, the y_{ii} in f_Δ expression will be substituted by the analytical solution of $\partial P_i(y_{ii})/\partial y_{ii} = 0$. Since y_{jj} is never changing in this scenario, its initial value under normal operating condition is quite small and can be ignored in the polynomial expression. Note that, the polynomial terms with conductances are also ignored, since the absolute value of conductance is usually much smaller than the one of susceptances in transmission system. Finally, the f_Δ will have the following form

$$\begin{aligned} f_\Delta^i \approx & -\frac{1}{2}\left|\bar{E}\right|^2 \sqrt{B_{ij}^2 + 2B_{ij}B_{Ej} + 2B_{Ej}^2}\, B_{ij}B_{Ei}B_{Ej}^2 / \\ & \{[(-B_{ij} - B_{Ej})\sqrt{B_{ij}^2 + 2B_{ij}B_{Ej} + 2B_{Ej}^2} + B_{ij}^2 + 2B_{ij}B_{Ej} + 2B_{Ej}^2] \\ & (B_{ij}^2 + 2(B_{Ei} + B_{Ej})B_{ij} + 2B_{Ei}B_{Ej})\} < 0 \end{aligned} \tag{2-36}$$

A negative value of this expression indicates that when the active power reaches maximum due to the local load's increment, the limit about local load will be smaller than the one with respect to remote load. Considering the sequence described in ***Property* 2**, as a consequence, the sequence swap will happen before the "nose" point under this load increasing scenario.

***Property* 4: If only a remote load is increasing, at the "nose" point, $P_{i,i}^{Max} > P_{i,j}^{Max}$ when the boundary buses have different "nose" points, and $P_{i,j}^{Max}$ is reached firstly.**

$P_{i,j}^{Max}$ is fixed since it matches the assumption of load increasing direction, and all variables in $P_{i,j}^{Max}$ are constant. When P_i reaches its maximum, y_{jj} is the solution of

$\partial P_i(y_{jj})/\partial y_{jj} = 0$. Therefore, the y_{jj} in f_Δ expression will be substituted by the analytical solution of $\partial P_i(y_{jj})/\partial y_{jj} = 0$. Since y_{ii} is never changing in this scenario, its initial value under normal operating condition is much small and can be ignored in polynomial expression. Note that, the polynomial terms with conductances are also ignored, since the absolute value of conductance is usually much smaller than the one of susceptance in a transmission system. Finally, the f_Δ will have the following form

$$f_\Delta^j \approx \frac{1}{2}|E|^2 B_{Ei} \frac{f_a}{f_b f_c} \tag{2-37}$$

where, f_a, f_b and f_c are real polynomial functions of all admittances. By checking the explicit expressions of f_b and f_c term by term, $f_b < 0$ and $f_c > 0$. Therefore, the sign of f_a determines the sign of f_Δ^j. Firstly, split f_a into positive part f_{a+} and negative part f_{a-}. To compare their absolute values, the following equation can be utilized

$$\begin{aligned} f_{a+}^2 - f_{a-}^2 = -B_{Ei}(2B_{ij} + B_{Ei})[B_{ij}^4 + 2(B_{Ei} + B_{Ej})B_{ij}^3 + 2(B_{Ei}^2 + \\ 3B_{Ei}B_{Ej} + B_{Ej}^2)B_{ij}^2 + 4(B_{Ei}^2 B_{Ej} + B_{Ei}B_{Ej}^2)B_{ij} + 2B_{Ei}^2 B_{Ej}^2]g \end{aligned} \tag{2-38}$$

where,

$$\begin{aligned} g = 2B_{Ei}B_{ij}^7 - (3B_{Ei}^2 + 4B_{Ei}B_{Ej} + 2B_{Ej}^2)B_{ij}^6 - (26B_{Ei}^3 + 34B_{Ei}^2 B_{Ej} + \\ 12B_{Ei}B_{Ej}^2)B_{ij}^5 - (46B_{Ei}^4 + 98B_{Ei}^3 B_{Ej} + 42B_{Ei}^2 B_{Ej}^2)B_{ij}^4 - (32B_{Ei}^5 + \\ 124B_{Ei}^4 B_{Ej} + 80B_{Ei}^3 B_{Ej}^2)B_{ij}^3 - (8B_{Ei}^6 + 72B_{Ei}^5 B_{Ej} + 80B_{Ei}^4 B_{Ej}^2)B_{ij}^2 - \\ (16B_{Ei}^6 B_{Ej} + 40B_{Ei}^5 B_{Ej}^2)B_{ij} - 8B_{Ei}^6 B_{Ej}^2 \end{aligned} \tag{2-39}$$

By introducing $B_{12} = kB$ and $B_{Ei} = B_{Ej} = B$, we have

$$g = 2k^7 - 9k^6 - 72k^5 - 186k^4 - 236k^3 - 160k^2 - 56k - 8 \tag{2-40}$$

The roots of $g = 0$ are 3 pairs of conjugate complex roots and one real root 9.48. If the boundary buses' "nose" points are different, which means B_{12} won't be significant larger than the others, so *g* will be negative, then $f_{a+}^2 - f_{a-}^2 > 0$ and $f_a > 0$, finally $f_\Delta^j > 0$. If their "nose" point are almost the same, according to (2-37), since the numerator's order of B_{12} is larger than the denominator's order, (2-37) will approach zero when $B_{12} \to \infty$.

***Property* 5: The stronger the coupling relationship is, the closer the limits will be.**

When $B_{12} \to \infty$, (2-35), (2-36) and (2-37) will approach zero, which means the limits will be closer to each other as the coupling relationship is stronger.

As a conclusion, the five properties have been presented and their proofs for the power transfer limits for the *N*+1 equivalent model have been shown in details. The following facts are critical for the applications of the *N*+1 equivalent model method for measurement-based voltage stability monitoring:

1. The variation of the limit will tell actually variation direction of the loads;
2. The power transfer limit met firstly indicates that the "nose" point has been reached;
3. The coupling relationship tells the closeness of the limits.

2.5 Online Scheme for Implementation

Compared with the traditional TE-based approach, this new measurement-based method uses a more complex *N*+1 buses equivalent to model more details about the boundary of a load area. Synchronized measurements on all boundary buses are needed

from either state estimation results if only steady-state voltage instability is concerned or PMUs for real-time detection of voltage instability. The parameters of the equivalent are identified using real-time measurements over a recent time window for several seconds. In a later case study on the NPCC system, results from 5s and 10s time windows will be compared. If the scheme uses PMUs, in order to speed up online parameter identification and filter out noise or dynamics irrelevant to voltage stability, the original high-resolution measurements (e.g. at 30Hz) may be downgraded to a low-sampling rate f_s (e.g. 2Hz) by averaging the raw data over a time internal of $1/f_s$ (i.e. 0.5s for 2Hz).

As shown by the flowchart in Figure 13, the new method first identifies all branches connecting the load area with the rest of the system, which comprise a cut set partitioning the load area. Those branches are assumed coming from the same voltage source $\overline{E}$. Then, any branches coming to the same boundary buses are merged. Assume that M branches are yielded. The proposed method is able to calculate the transfer limit for each branch using an M+1 buses equivalent. However, if M is large, it will result in huge computational burdens in estimating $M(M\text{-}1)/2+2M+1$ parameters and consequently calculating M limits. Different from the TE that merging all M branches to one fictitious tie line, this new approach may group some branches across the boundary and only merge each group to one fictitious tie line. The criteria of grouping are such as: the boundary buses in one group are tightly interconnected; the branches in one group reach limits almost at the same time; it is not required to monitor the branches within a group individually. For the fictitious tie line representing a group of branches, only its total limit is calculated. Thus, after merging some groups of branches to fictitious tie lines, the final number of tie lines becomes $N<M$. A

simpler N+1 buses equivalent is used, which still keeps characteristics of the load area regarding voltage stability. The TE-based approach is a special case of this new method with N=1.

The next two sections will test the new method on a 4-bus power system and the NPCC 140-bus system using data generated from simulation. All computations involved in the algorithms of the new method are performed in MATLAB on an Intel Core i7 CPU desktop computer.

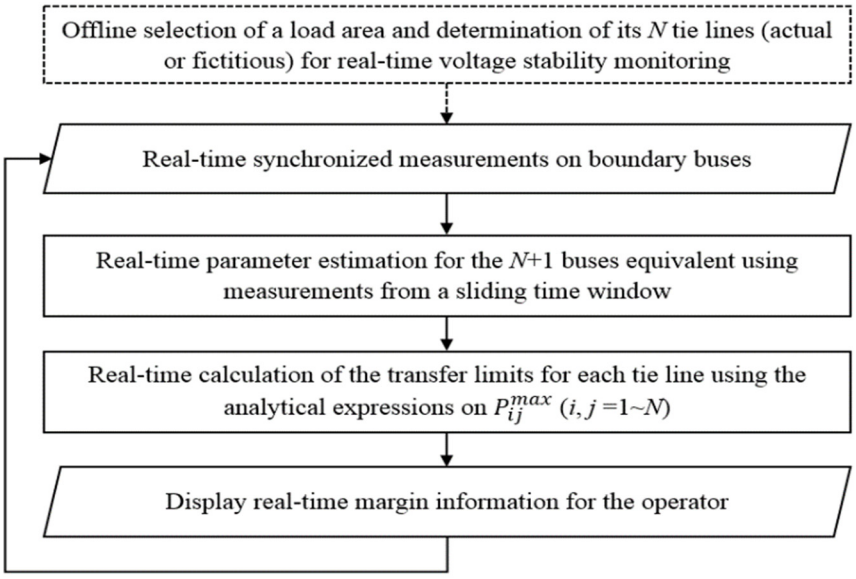


Figure 13. Flowchart of the new method.

2.6 Demonstration on a 4-bus Power System

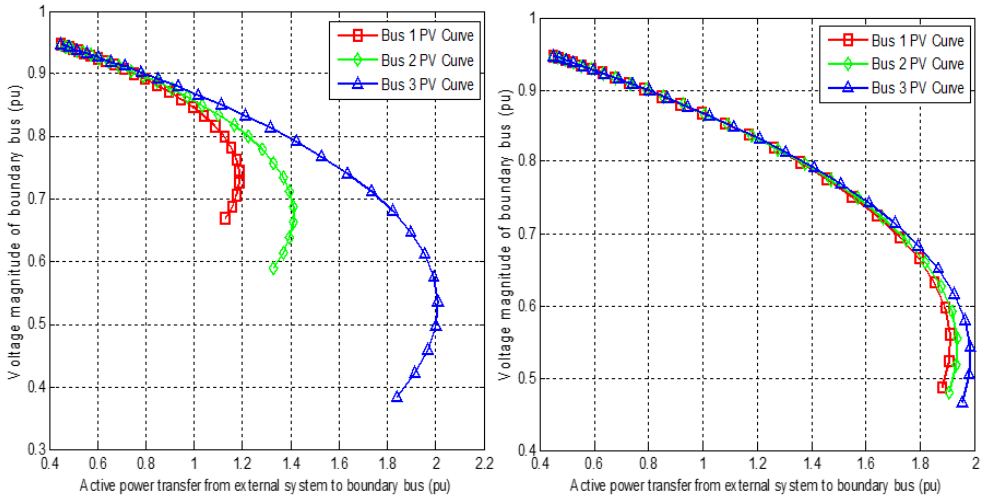
This section demonstrates the new method on a 4-bus power system with one constant voltage source supporting three interconnected load buses representing a load area. The system is simulated in MATLAB with gradual load increases at three load buses.

The simulation results on three load buses are treated as PMU data and fed to the new method. The system represents a special case of the system in Figure 1 with N=3. Let $\overline{E} = 1.0\angle 5^\circ$ p.u. and three tie lines have the same impedance $\overline{z}_{E1} = \overline{z}_{E2} = \overline{z}_{E3} = 0.01 + j0.1$ p.u. At the beginning, three load impedances $\overline{z}_{11} = \overline{z}_{22} = \overline{z}_{33} = 1 + j1$ p.u. Consider two groups of transfer impedances in Table I respectively for weak and tight connections between three boundary buses.

Table 1. Values of transfer impedances

Group	$\overline{z}_{12}$ (p.u.)	$\overline{z}_{13}$ (p.u.)	$\overline{z}_{23}$ (p.u.)
A	0.01+j0.1	0.015+j0.15	0.005+j0.05
B	0.0005+j0.005	0.0008+j0.0075	0.0003+j0.0025

Keep the impedance angle of $\overline{z}_{33}$ unchanged but gradually reduce its modulus by 1% every 2s until active powers on all tie lines meet limits. As shown in Figure 14, three PV curves (P_i vs. V_i) are drawn for two groups of transfer impedances. For Group A, the transfer impedances between boundary buses are not ignorable compared with the tie-line and load impedances, so three PV curves are distinct. However, when those impedances decrease to the values in Group B, three PV curves coincide, which is the case a TE can be applied to.



(a) Group A (weak). (b) Group B (tight).

Figure 14. PV curves for weak and tight connections between boundary buses.

Simulation results are recorded at 1Hz sampling rate. The new method is performed every 1s using the data of the latest 10s time window. All computation of the new method on each time window is finished within 0.05s in MATLAB. The new method gives each tie line three limits for three extreme load increase assumptions. For two groups, Figures. 15 and 16 show $P_1 \sim P_3$, the total tie-line flow $P_\Sigma = P_1 + P_2 + P_3$, and their limits calculated by the new method. The limits from solutions of $\partial P_1/\partial y_{33} \sim \partial P_3/\partial y_{33}$ match the actual load increase, so their sum is defined as the total tie-line flow limit $P_\Sigma^{\text{Max(New)}}$. For comparison, the TE-based method in [47] and [48] is also performed to give the total tie-line flow limit as $P_\Sigma^{\text{Max(TE)}}$ in Figure 15.

Tests on those two groups of data show that when a TE-based method is applied to a load area, voltage instability is detected only when the total tie-line flow meets its limit.

However, due to the uneven increase of load, one tie line may be stressed more to reach its limit earlier than the others, which can successfully be detected by the new method. Another observation on Figures. 15 and 16 is that the curve of $P_{\Sigma}^{\text{Max(New)}}$ is flatter than that of $P_{\Sigma}^{\text{Max(TE)}}$, and $P_{\Sigma}^{\text{Max(TE)}}$ is more optimistic and less accurate than $P_{\Sigma}^{\text{Max(New)}}$ when the system has a distance to voltage instability.

For Group A with weak interconnection between boundary buses, Figure 15 shows that three individual tie-line flows P_1, P_2 and P_3 meet their limits at t=680s, 676s and 666s respectively. The total tie-line flow P_{Σ} meets $P_{\Sigma}^{\text{Max(New)}}$ at t=680s. $P_{\Sigma}^{\text{Max(TE)}}$ from the TE-based method is not as flat as $P_{\Sigma}^{\text{Max(New)}}$, and it is met by P_{Σ} after t=700s. Figure 17-19 give details of Figure 15 on each tie-line flow and its three limits calculated according to (2-18) for three load increase assumptions. The limit from solution of $\partial P_i/\partial y_{33}$ matches the actual load increase, and its curve is flat and met by P_i earlier than the other two. By using the new method, zero margin is first detected at t = 666s on the 3rd tie line and then on the other two tie lines as well as the total tie-line flow. However, the TE-based method detects zero margin much later since, first, it only monitors the total tie-line flow limit and second, the limit curve is not as flat as that given by the new method.

For Group B with tight connection between boundary buses, Figure 16 shows that all tie-line flows reach their limits at t=732s. In addition, P_{Σ} meets both $P_{\Sigma}^{\text{Max(New)}}$ and $P_{\Sigma}^{\text{Max(TE)}}$ at that same time.

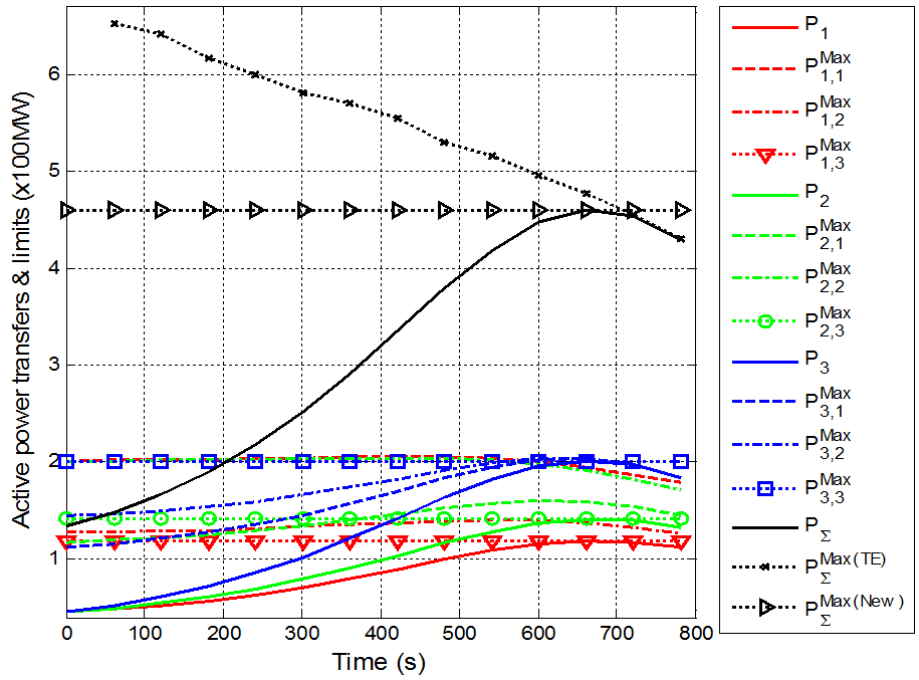


Figure 15. Tie-line flows and limits for Group A (weak connection).

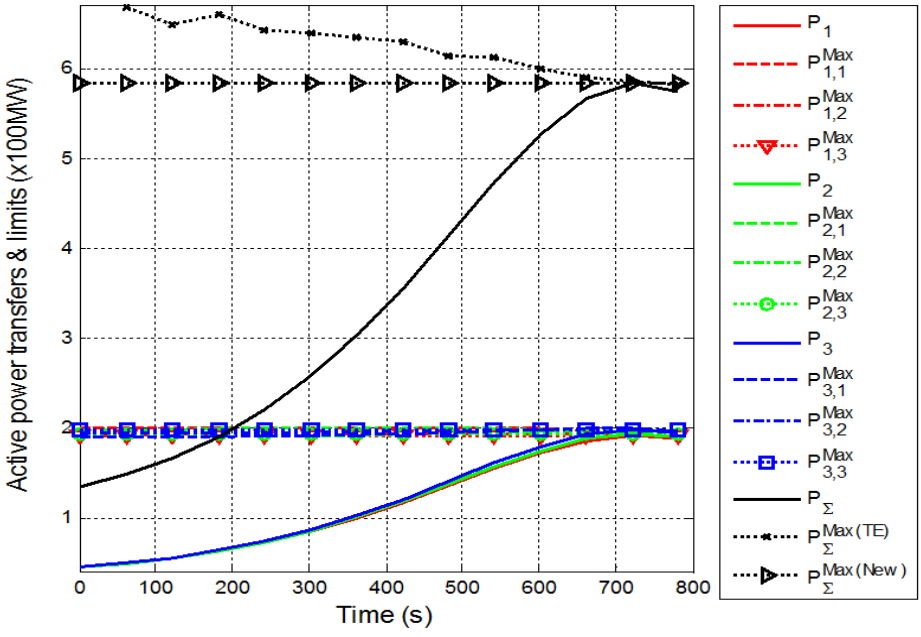


Figure 16. Tie-line flows and limits for Group B (tight connection).

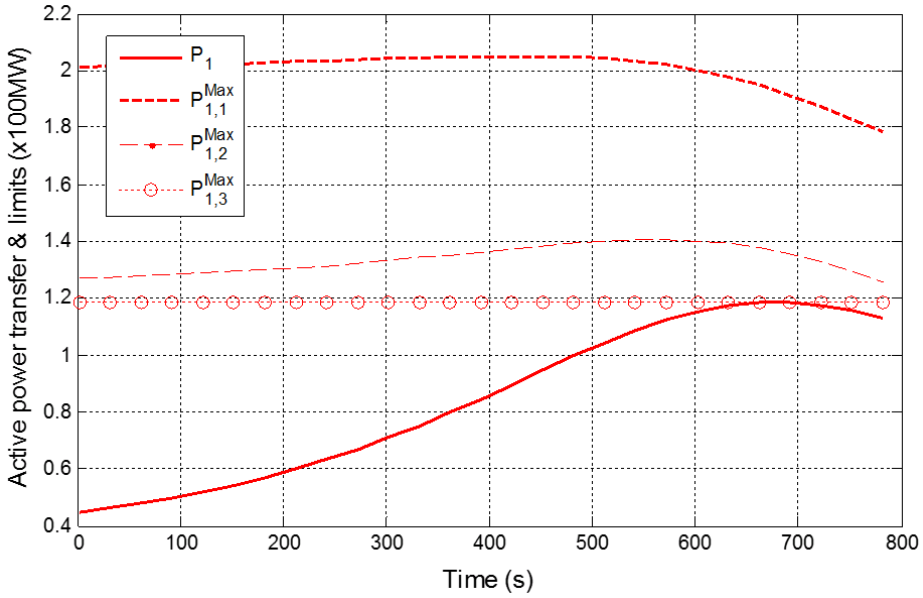


Figure 17. P1 and limits for Group A.

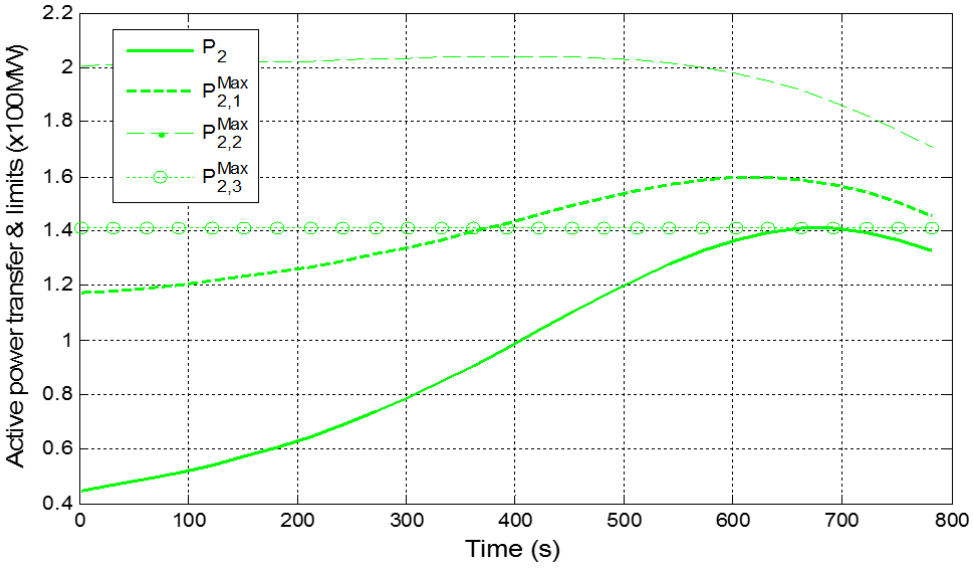


Figure 18. P2 and limits for Group A.

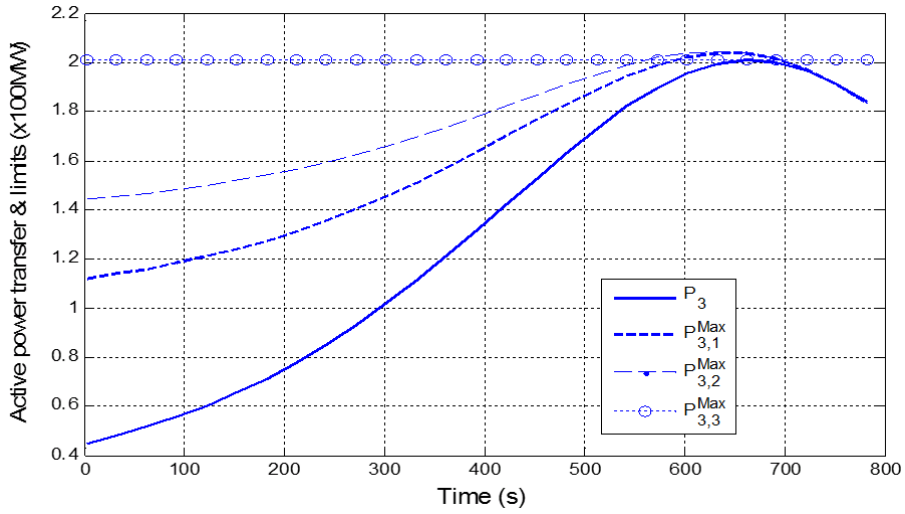


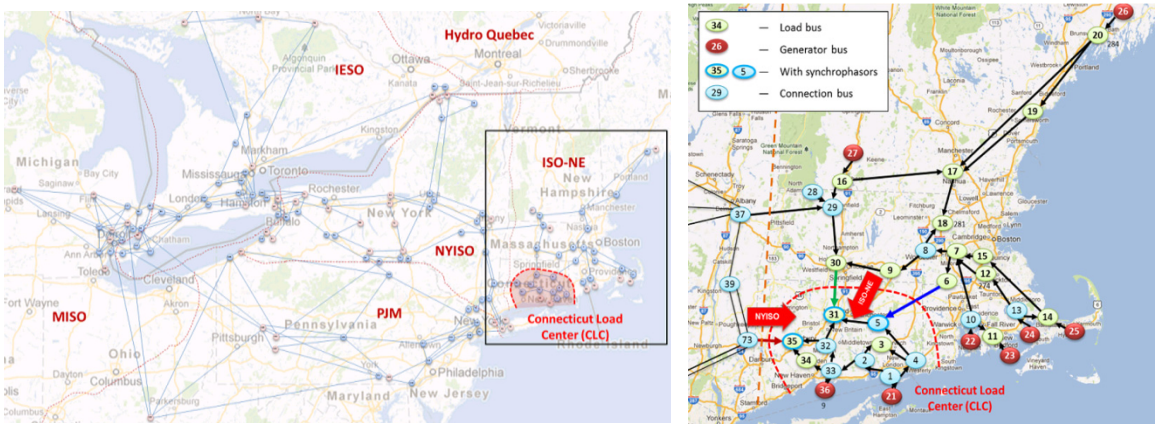
Figure 19. P3 and limits for Group A.

2.7 Case Studies on the NPCC Test System

The proposed new method is tested on a Northeast Power Coordinating Council (NPCC) 48-machine, 140-bus system model [58]. As highlighted in Figure 20, the system has a Connecticut Load Center (CLC) area supported by power from three tie lines, i.e. 73-35, 30-31 and 6-5. Line 73-35 is from the NYISO region and the other two are from the north of the ISO-NE region. Powertech's TSAT is used to simulate four voltage instability scenarios about the CLC area:

1. Generator trip followed by load increase leading to voltage instability;
2. Generator trip followed by a tie-line tip causing voltage instability;
3. Two successive tie-line trips causing voltage instability;
4. Shunt switching to postpone voltage instability.

The load model at each load bus adopts the default load model setting in TSAT, i.e. 100% constant current for real power load and 100% constant impedance for reactive power load. Simulation results on the voltages at boundary buses 35, 31 and 5 and the complex powers of the 3 tie lines are recorded at 30Hz, i.e. the typical PMU sampling rate. The raw data are preprocessed by an averaging filter over 15 samples to be downgraded to 2Hz. The processed data are then fed to the new method for estimating the external and load area parameters and calculating transfer limits. That data preprocessing improves the efficiency of two optimizations for parameter estimation while keeping necessary dynamics on voltage stability in data. The new method is performed every 0.5s on data of the latest 5-s time window.



(a) System topology. (b) CLC area.

Figure 20. Map of NPCC system and CLC area.

2.7.1 Generator Trip Followed by Load Increase Leading to Voltage Instability

To create voltage collapse in the CLC area, all its loads are uniformly increased by a total of 0.42 MW per second from its original load of 1906.5 MW with constant load power factors. At *t*=360s, the generator on bus 21 is tripped, which pushes the system to be close to the voltage stability limit. Shortly after slight load increase, voltage collapse happens around *t*=530s as shown in Figure 21 on three boundary bus voltages. Figure 22 indicates the PV curves monitored at three boundary buses. To better illustrate the PV curves, the figure is drawn using the data sampled at 25s intervals until *t*=500s to filter out transient dynamics on the curves right after the generator trip and the voltage collapse at the end. Note that the generator trip causes a transition from the pre-contingency PV curves to the post-contingency PV curves with a more critical condition of voltage stability. Bus 35 is the most critical bus since the "nose" point of its post-contingency PV curve is passed.

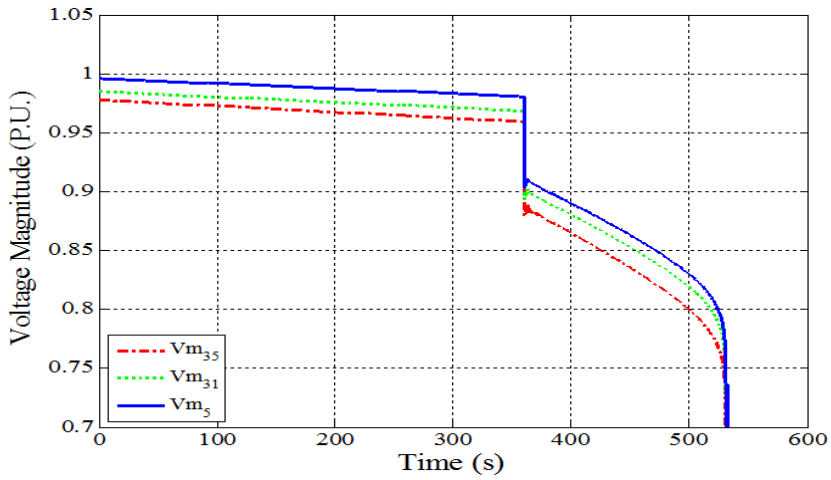


Figure 21. Voltage magnitudes at CLC boundary buses.

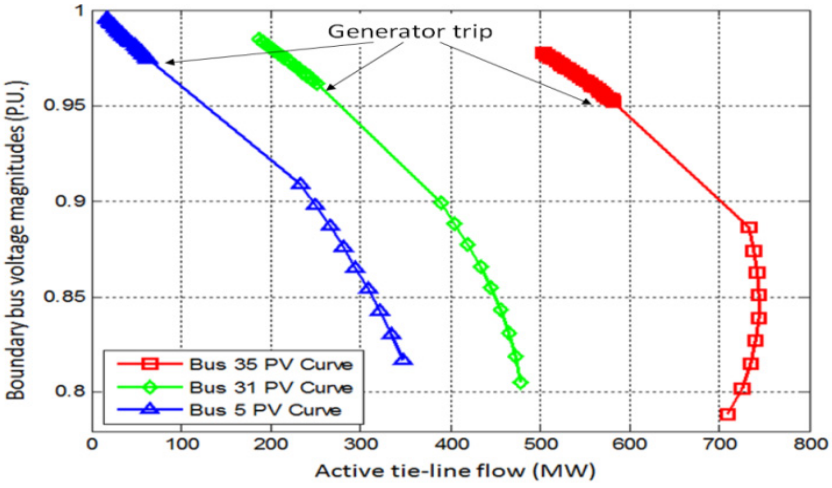


Figure 22. PV curves monitored at the CLC boundary buses.

When the external system has strong coherency, the proposed new method can be applied to reduce it to one voltage phasor $\overline{E}$ connected with boundary buses of the load area by N branches, respectively. Figures. 23 and 24 show the voltage magnitudes and angles of all buses in Figure 20(b) that are outside the CLC load center, indicating a strong coherency of the external system [59]. Therefore, the proposed method is valid and may adopt a 3+1 buses equivalent to calculate the power transfer limits separately for three tie lines.

Figure 25 gives estimates of three load impedance magnitudes seen at the boundary buses. The figure shows that the load seen from bus 5 changes more significantly than the others. Hence, $P_{35,5}^{\mathrm{Max}}$, $P_{31,5}^{\mathrm{Max}}$ and $P_{5,5}^{\mathrm{Max}}$ calculated from $\partial P_i/\partial y_5=0$ are more accurate and used to calculate stability margin.

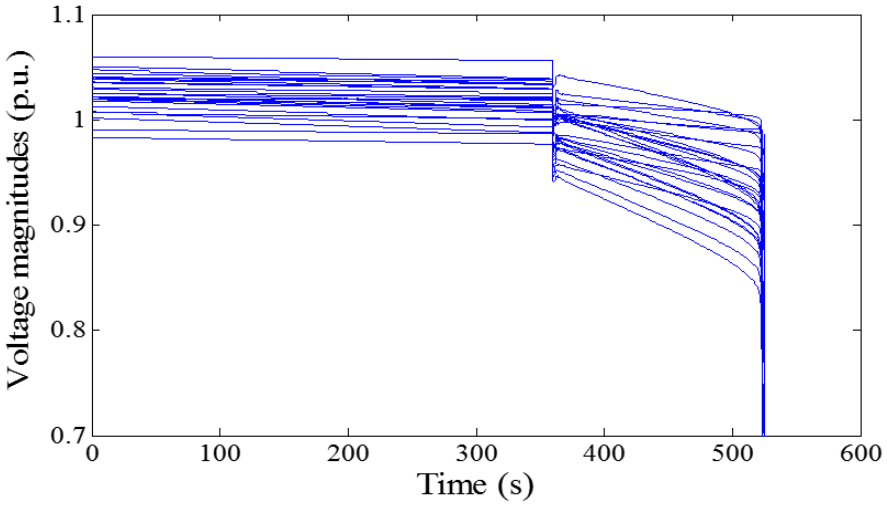


Figure 23. External system bus magnitudes.

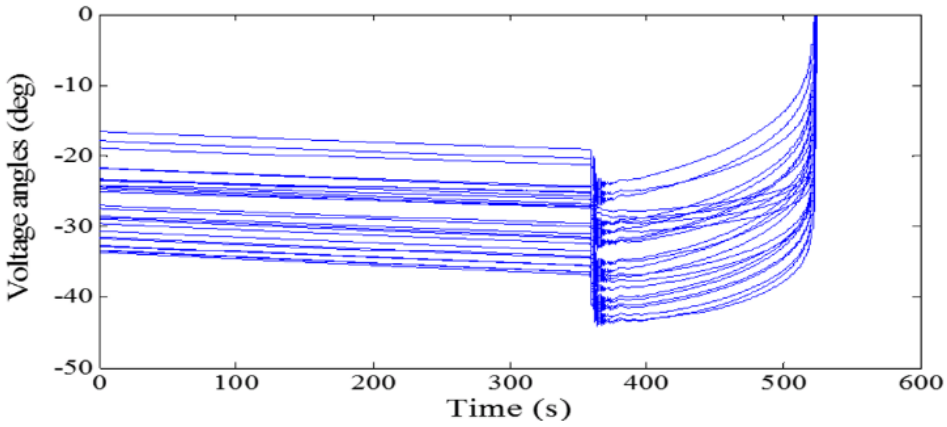


Figure 24. External system bus angles.

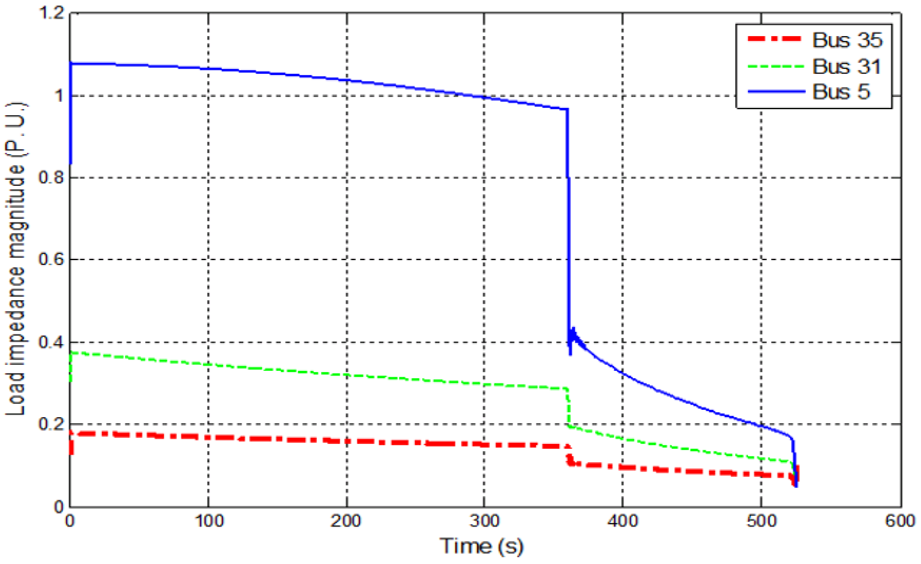


Figure 25. Real-time estimation of load impedance magnitudes.

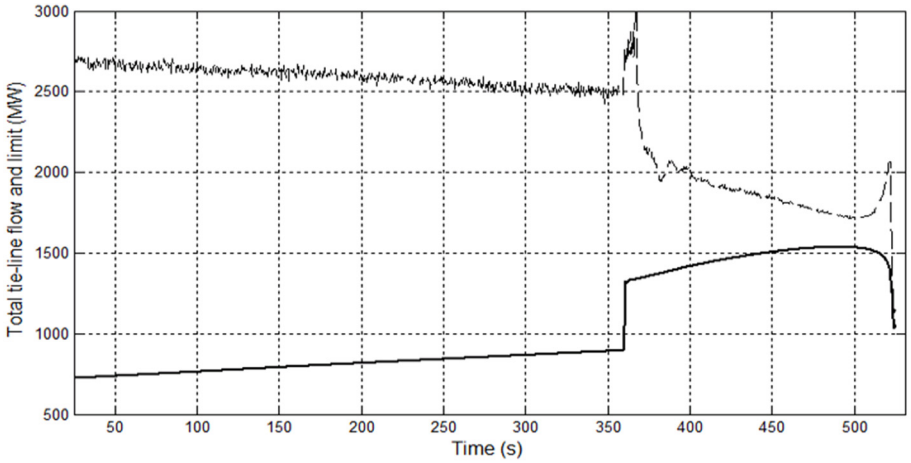
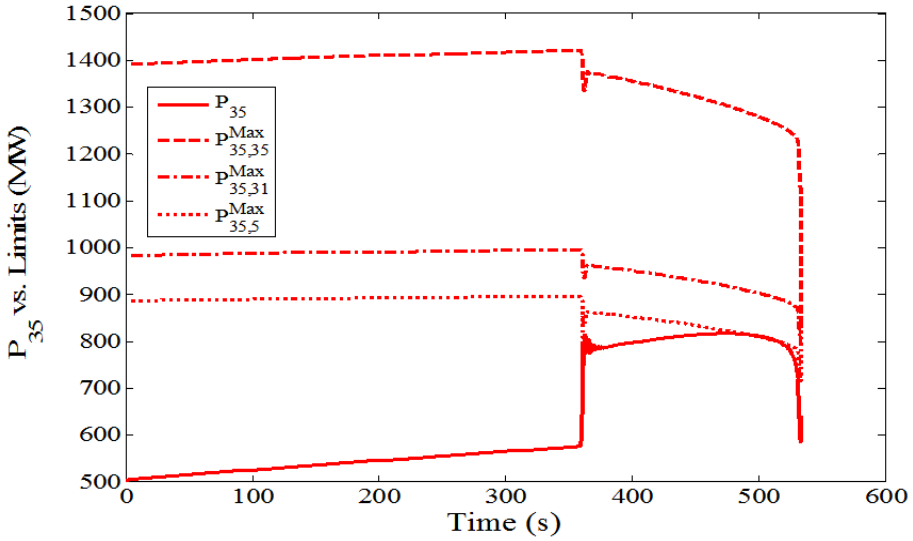


Figure 26. Result from a TE-based method.

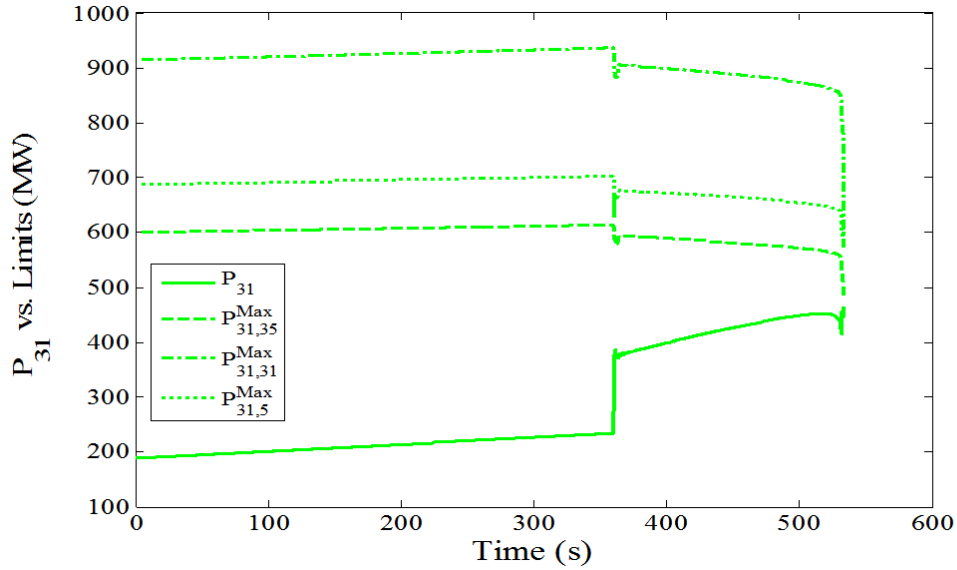
To compare with the new method, Figure 26 gives the total transfer limit estimated using a TE-based method. The margin stays positive until the final collapse of the entire system.

Figure 27 gives the results from the new method and each tie line has three transfer limits. Before the generator trip, all lines have sufficient margins to their limits. After the trip, more power is needed from the external system, so the active powers of the three tie lines all increase significantly to approach to their limits. In Figure 27(a), P_{35} of 73-35 reaches the limit $P_{35,5}^{\text{Max}}$ at t=473.5s. From Figure 27 (b) and (c), the other two lines keep positive margins until the final voltage collapse. It confirms the observation from Figure 22 that voltage collapse will initiate from bus 35. If the limit and margin information on individual tie line is displayed for operators in real time, an early remedial action may be taken before voltage collapse. However, such information is not available from a TE-based method.

Figure 27. Transfer limits of each tie line calculated by the new approach.

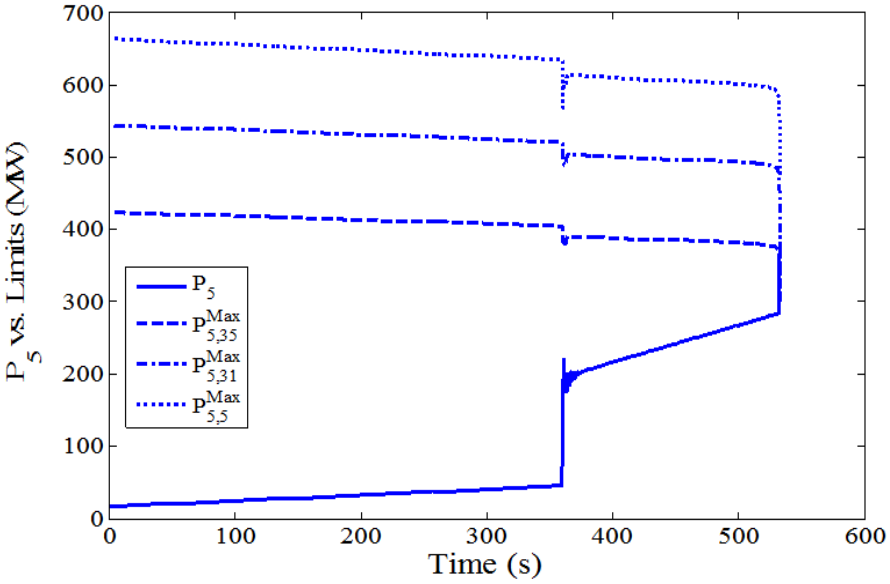


(a) P35 vs. its limits.



(b) P31 vs. its limits.

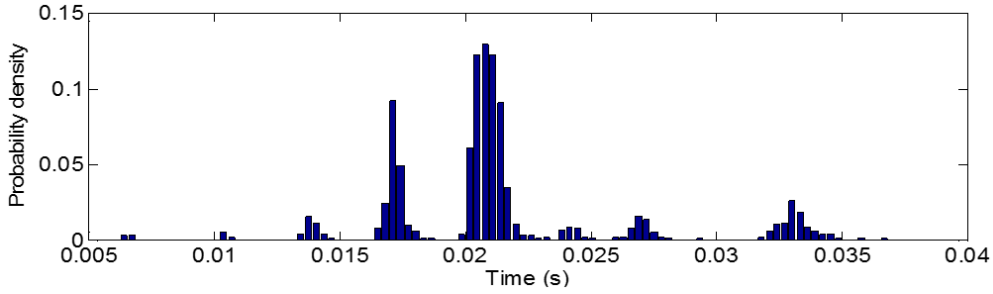
Figure 27 Continued



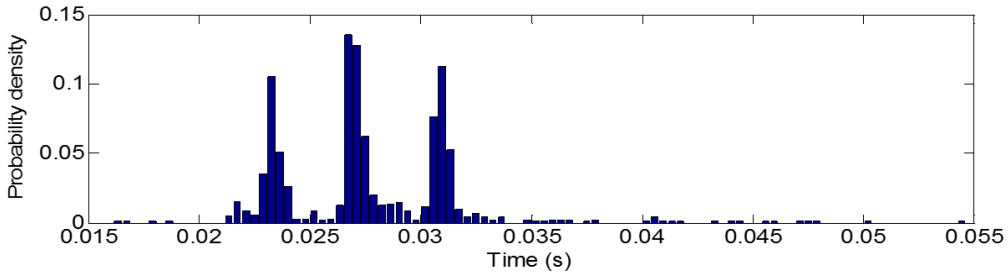
(c) P5 vs. its limits.

Figure 27 Continued

Once parameters of the N+1 buses equivalent are estimated, transfer limits are directly calculated by their analytical expressions. The major time cost of the new method is with online parameter estimation. Figure 28 gives the probability density about the times spent respectively on estimating the external system and the load area over one time window. According to the figure, parameter estimation over one time window can be accomplished within 0.02s to 0.1s. The average total time cost for each cycle of the new method's online procedure (i.e. steps 2-5 in Figure 13) is 0.0614s, which includes 0.0221s for external parameter estimation, 0.0271s for load area parameter estimation, and 0.0122s for transfer limits calculation. The times on measurements input and margin display are ignorable. The test results indicate that the new method can be applied in an online environment.



(a) Time for estimating external system parameters.



(b) Time for estimating load area parameters.

Figure 28. Time performances on online parameter estimation.

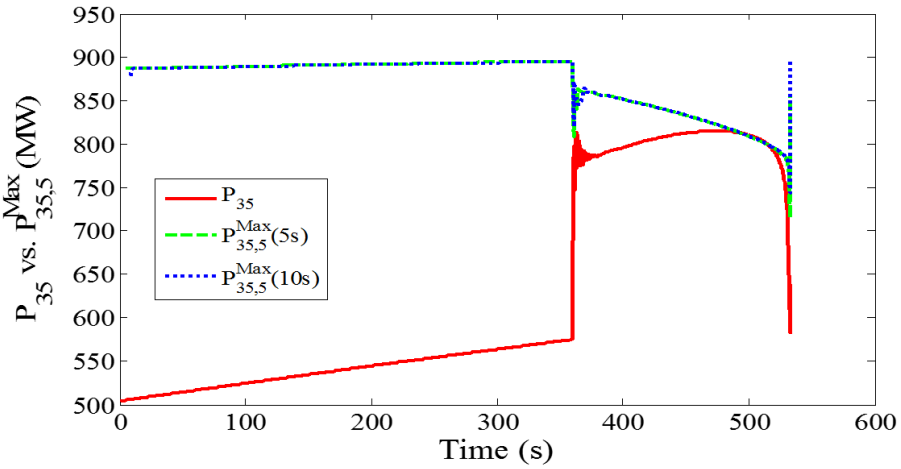


Figure 29. Comparison of different optimization time windows.

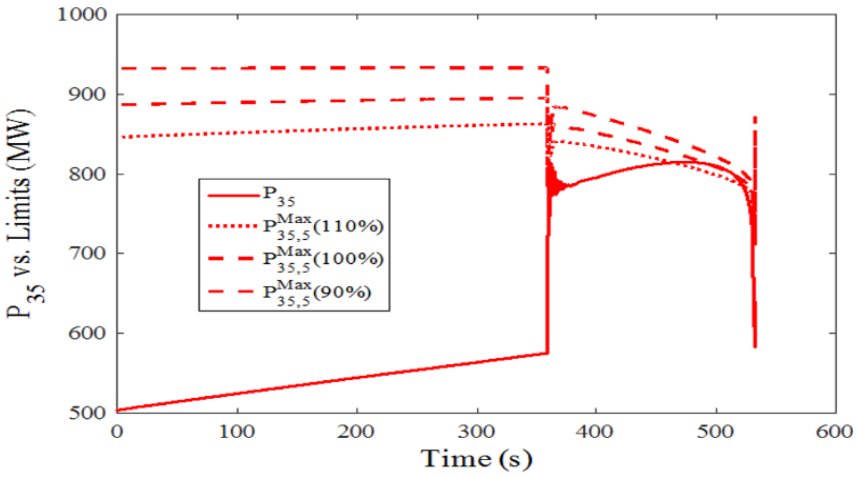


Figure 30. Comparison of initial values with errors.

Figure 29 compares the estimated $P_{35,5}^{\text{Max}}$ using a 5s sliding time window with that using a 10s sliding window. Two results match very well, which indicates that the new method is not very sensitive to the length of the sliding time window.

To test the results of the new method using inaccurate initial values in the external system parameter estimation, Figure 30 compares the tie-line power limits for 73-35 with three different sets of initial values: 110%, 100%, and 90% of the estimates from a Least Square method on the first time window at the beginning. From the figure, a 10% error will cause less than 5% error in the transfer limit estimation before the generator trip and about 2% error in the limit after the generator trip. If the Least Square method is used to re-estimate the initial values when the generator trip is detected, that 2% error can be eliminated and these three limits will merge to one limit associated with accurate initial values. Considering in the real world, small errors in the initial values cannot be avoided completely, a small positive threshold rather than zero may be defined for the transfer margin as an alarm of voltage instability.

2.7.2 Generator Trip Followed by a Tie-Line Tip Causing Voltage Instability

Before t=400s, this scenario is the same as Scenario B. At t=400s, tie line 73-35 is tripped to cause voltage collapse immediately. The voltage magnitudes of three boundary buses are shown in Figure 31.

Figure 32 shows the tie-line power flows and their limits for this scenario. After the generator trip, all tie-line flows become closer to their limits, and tie-line 73-35 carries 795 MW, which is higher than the total margin of 667MW on tie-lines 31-30 and 6-5. When tie line 73-35 is tripped at t=400s, its flow is transferred to the other two tie lines to cause

them to meet limits. That explains why voltage collapse happens following that tie-line trip. If the above tie-line margin information is presented to the system operator before *t*=400s, the operator will be aware of that the system following the generator trip cannot endure such a single tie-line trip contingency and may take a control action.

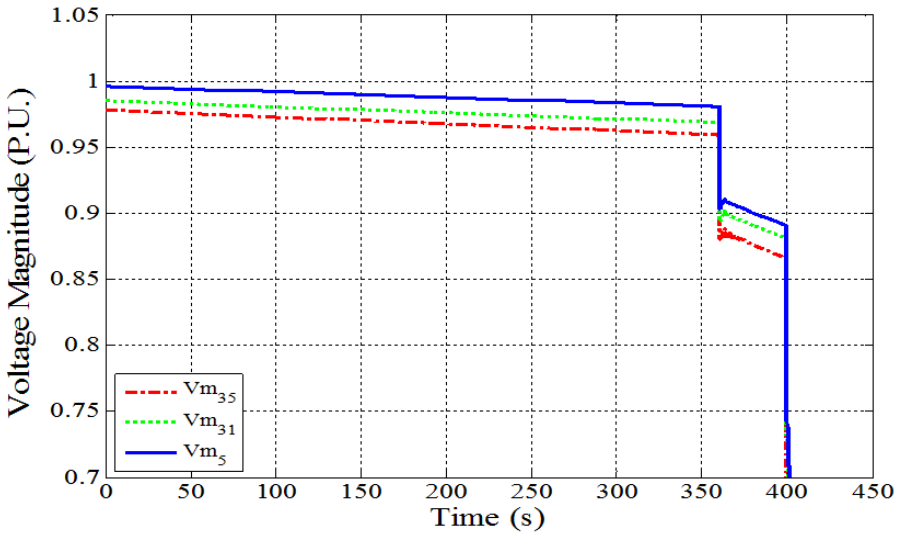
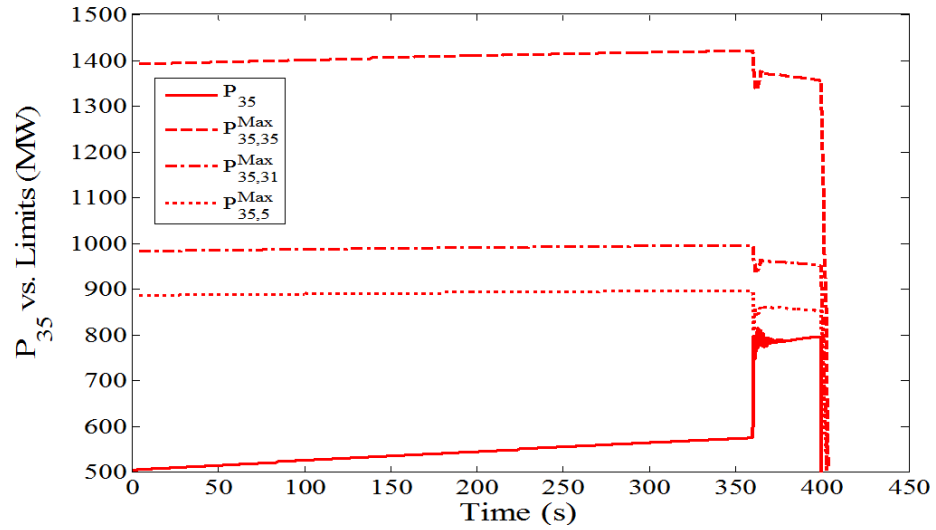
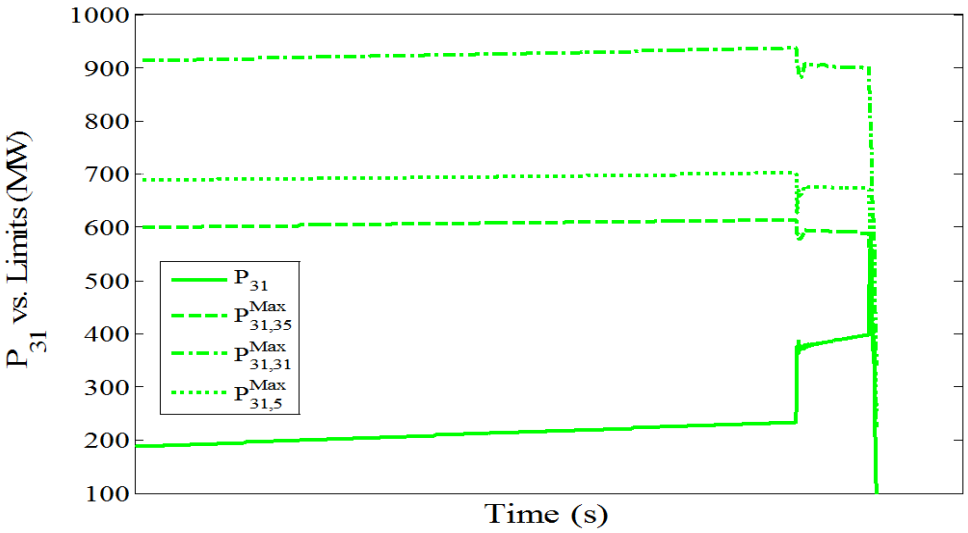


Figure 31. Voltage magnitudes at CLC boundary buses.

Figure 32. Transfer limits of each tie line calculated by the new approach.

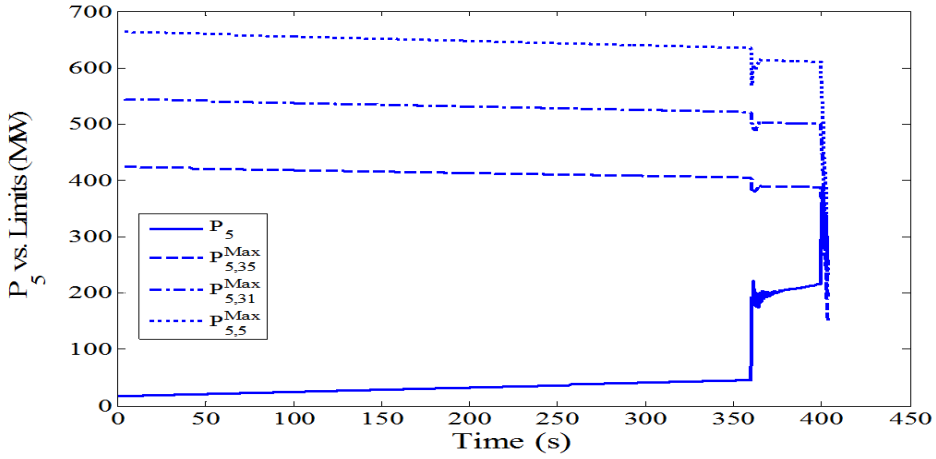


(a) P_{35} vs. its limits.



(b) P_{31} vs. its limits.

Figure 32 continued



(c) P_5 vs. its limits.

Figure 32 continued

2.7.3 Two Successive Tie Line Trips Causing Voltage Instability

In this scenario, two successive tie-line trips on 31-30 and 6-5 are simulated to test the adaptability of the new method to *n*-1 and *n*-2 conditions. During *t*=0-100s, all loads in CLC area are uniformly increased by 0.43MW/s from its original load of 1906.5 MW with constant power factors unchanged. At *t*=100s, the tie line 31-30 is tripped, and thus the voltages of three boundary buses drop significantly. During *t*=100-200s, loads keep increasing at a lower speed equal to 0.37MW/s. At *t*=200s, the tie line 6-5 is tripped, causing voltage collapse as shown in Figure 33.

Figure 34 gives the results on each tie line and the transfer limits. Before the tie line 31-30 is tripped at *t*=100s, all the tie lines have sufficient transfer margin. After that trip, P_{31}=0 is captured from measurements and the new method sets the corresponding y_{E31}=0 to adapt to the new "*n*-1" condition. Then, the transfer limit on the line 73-35 drops to 677 MW. Before the next the tie line 6-5 is tripped at *t*=200s, the tie lines 73-35 and 6-5 totally transfer 733MW to the CLC area, which is higher than the limit 677 MW of the tie line 73-35. Therefore, the second tie-line trip causes zero margin on the line 73-35, followed by a voltage collapse.

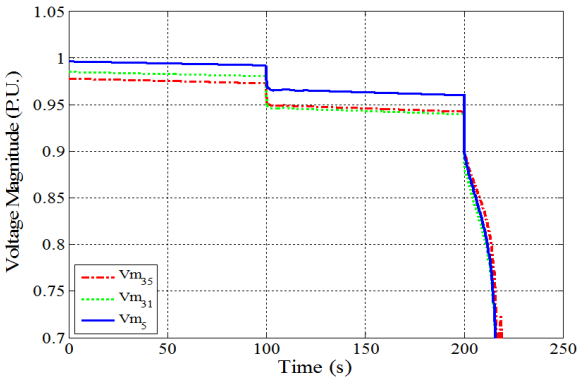
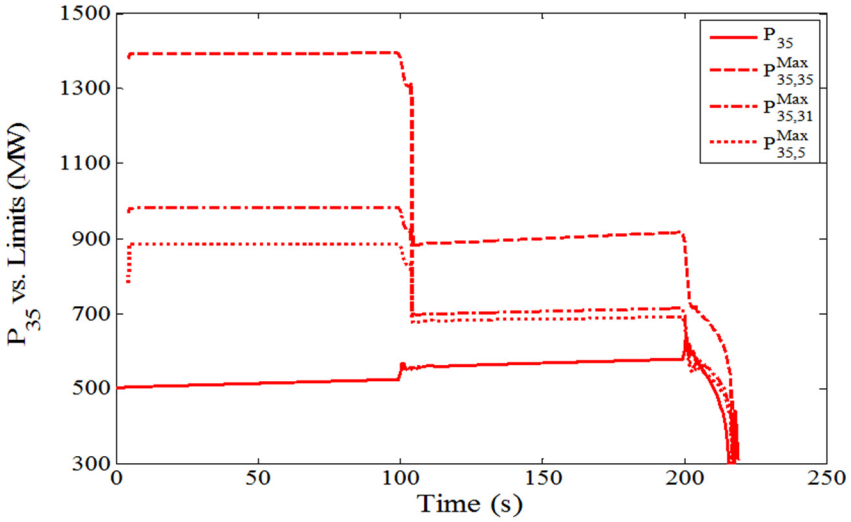
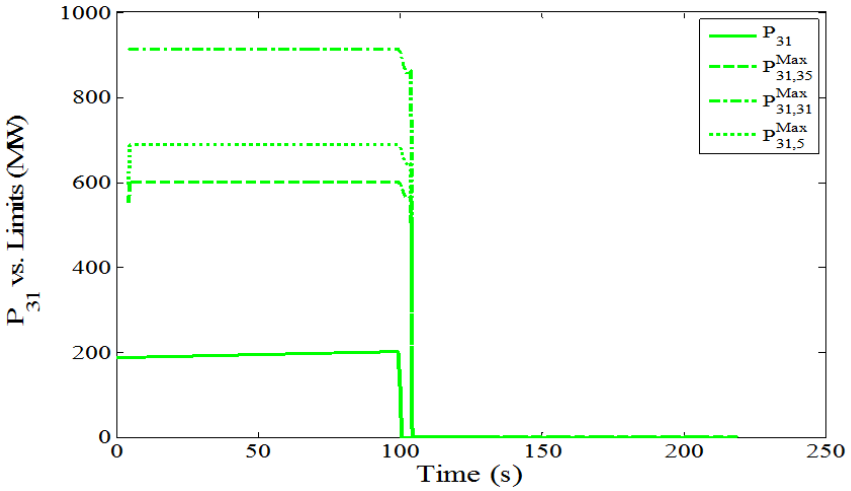


Figure 33. Voltage magnitudes at CLC boundary buses.

Figure 34. Transfer limits of each tie line calculated by the new approach.

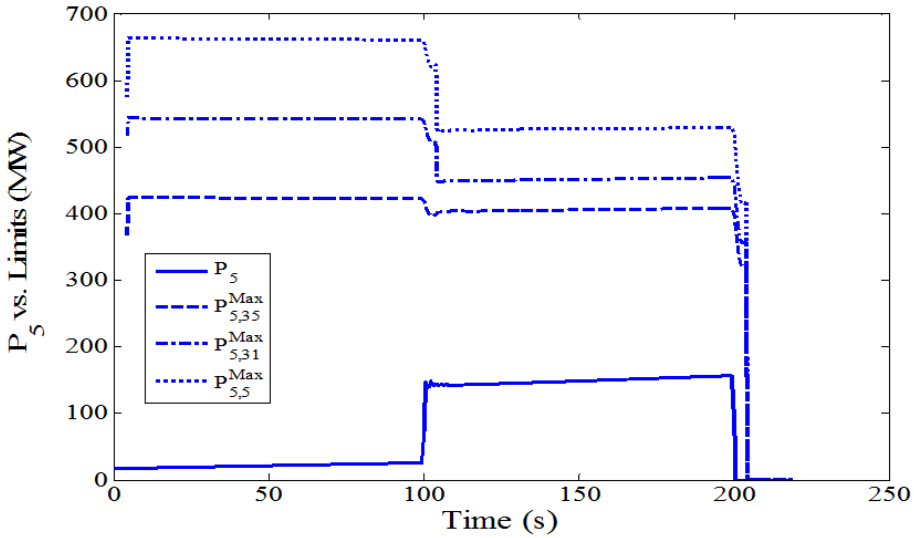


(a) P_{35} vs. its limits.



(b) P_{31} vs. its limits.

Figure 34 continued



(c) P_5 vs. its limits.

Figure 34 continued

2.7.4 Shunt Switching to Postpone Voltage Instability

This scenario considers switching in a capacitor bank located in the CLC area to postpone voltage collapse. Everything of this scenario during t=0-440s is the same as Scenario A. At t=440s when the transfer margin on the most critical tie-line 73-35 drops to 3%, a 50MVAR capacitor bank at the bus 33 is switched in. Due to its additional VAR support, the voltage of the CLC area increases as shown in Figure 35 about voltage magnitudes of three boundary buses. Figure 36 shows the transfer limits on the line 73-35 for this scenario. Both the tie-line flow and limits increase after that switch. The slight tie-line flow increase is caused by voltage-sensitive loads in the load area, which is smaller than the increase of the limit. Therefore, zero margin happens at t=496.5s, i.e. 23s later than the 473.5s of Scenario A. This scenario demonstrates that adding VAR support in the load area will increase voltage stability margin, which is correctly captured by the new method.

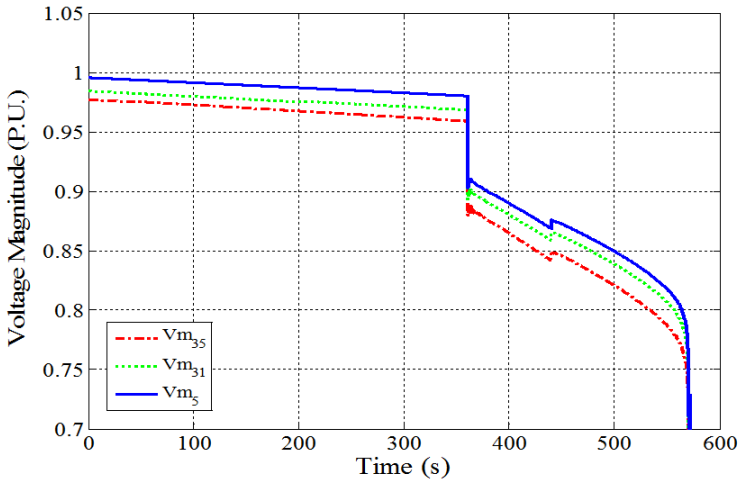


Figure 35. Voltage magnitudes at CLC boundary buses.

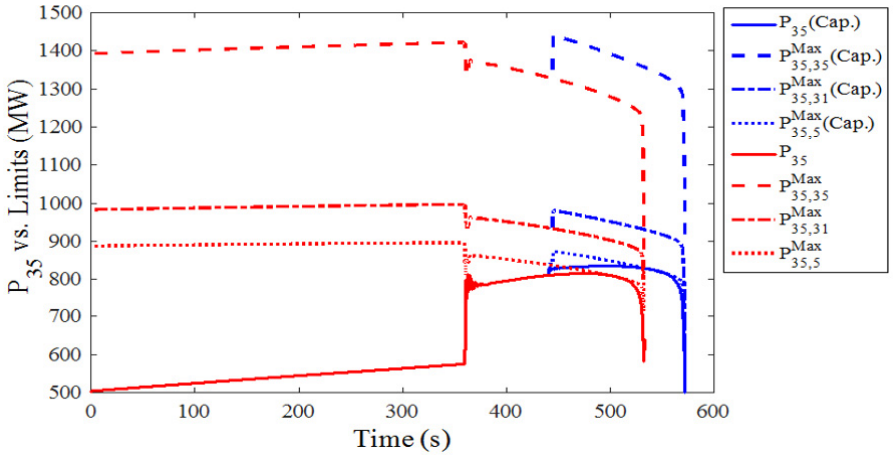


Figure 36. P_{35} vs. its limits.

2.8 Case Studies on a Detailed NYISO Model

Dynamic simulation of large, interconnected power systems is computationally intensive even for a standard 10-20 seconds simulation time horizon, and this computational burden limits the number of contingencies that can be analyzed within a given wall clock time and with a given computing resource. Thus, this limitation is particularly constraining for on-line Dynamic Security Assessment (DSA) because of the short time frame available. However, with the new MBVSA method, the voltage stability indicator can be obtained in real time even for a large wide area system.

A testing system was developed from a detailed NYISO power system. This test system has 25,357 buses, 4,198 generators, 18512 loads, 28,713 lines, 8,627 transformers and. In this system, load center has been highlighted in the box, with a total 4705.6 MW of active power and 1330 MVar of reactive power.

The interface (facing NYISO) corresponds to the branch 73-35 in the NPCC 140-bus system, these lines from 72925 LUDLOW to 73112 MANCHSTR corresponds to the branch 30-31, and these lines from 73119 LAKEROAD to 73108 CARD corresponds to the branch 6-5.

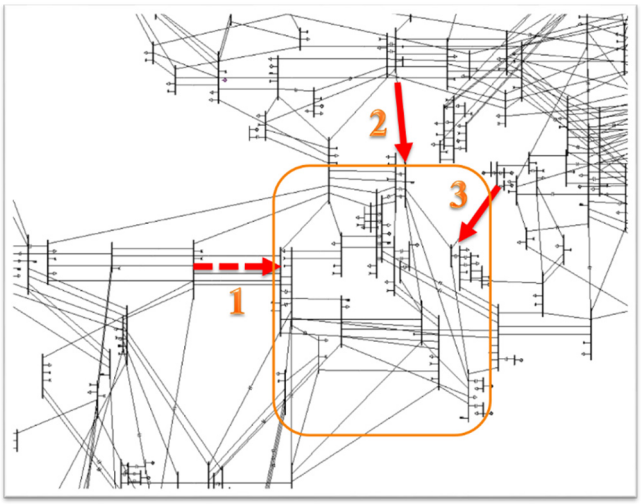


Figure 37. Load pocket Area Scheme.

The voltage collapse scenario has been created on this model considering both ZIP load models and dynamic load models. Ramp active power and reactive power of the loads in the load pocket area by 70% within 150s. At time 150s, disconnect the generator on bus 73563 and the generator on bus 73559. At time 160s, ramp active power and reactive power of the loads in the load pocket area by 35% within 40s. (Same rate as the first load ramping)

For the dynamic simulation, we used the Siemens PTI PSS/E to simulate the this detailed NYISO system, and it costs an average 320s to simulate the 200s scenario using

Intel i7-4870HQ processor (2.5 GHz base frequency and 3.7 GHz max turbo frequency). Based on the current configuration, it is 60% slower than real time.

For this detailed NYISO system, we are mainly focusing on the two tie-line groups connecting to ISONE pool and NYISO pool respectively. The group facing NYISO are defined as tie-line group 1, and the one facing ISONE are defined as tie-line group E. To aggregate the lines into one fictitious bus, the method in [26] is utilized.

$$\bar{I} = \sum_i \left(\frac{\bar{S}_i}{\bar{V}_i} \right)^2 \tag{2-41}$$

$$\bar{S}_L = \sum_i \bar{S}_i \tag{2-42}$$

$$\bar{V}_L = \frac{\bar{S}_L}{\bar{I}^*} \tag{2-43}$$

where $\bar{S}_i$ and $\bar{V}_i$ are complex power and voltage measured at bus *i* in the tie-line group.

This method actually provides a way for the reduction of the tie-line groups, and it reduces the computational burden with a scalable model. This allows the new method to be applied in large scale systems with thousand lines. Figure 38 shows the voltage magnitude and angle of these two fictitious buses.

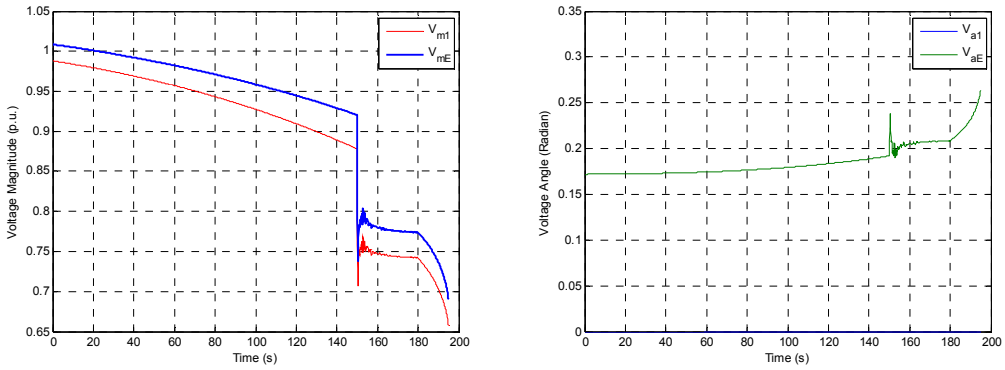


Figure 38. Voltage magnitude and angle of voltage collapse scenario.

As shown in Figure 39. with the aforementioned method, the active power and reactive power of the two fictitious tie lines can be easily obtained.

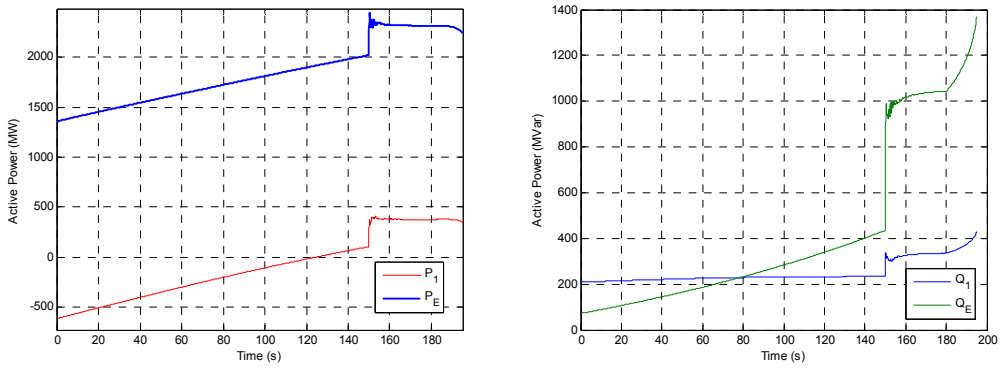


Figure 39. Active power and reactive power of voltage collapse scenario.

Before the trip of the generators on bus 73563 and the generator on bus 73559, the limits are almost constant values or slashes with certain slopes in Figure 40. After the transient state of the trip event happened at 140s, P_1 for group 1 still has positive margin, but P_E for group E has no margin. Shortly after one equivalent line passed its "nose" point,

voltage collapse happened. Based on the results from the new MBVSA, it tells that the transmission line group E is more critical than the transmission line group 1, which means the transmission lines connected ISONE pool have less margin than the ones connected NYISO pool. So this new method provides the operators with early detection of voltage collapse, and the identification of the critical transmission line. This complementary information will help the online time domain simulation for the selection of remedial actions which cannot be provided by the TE method.

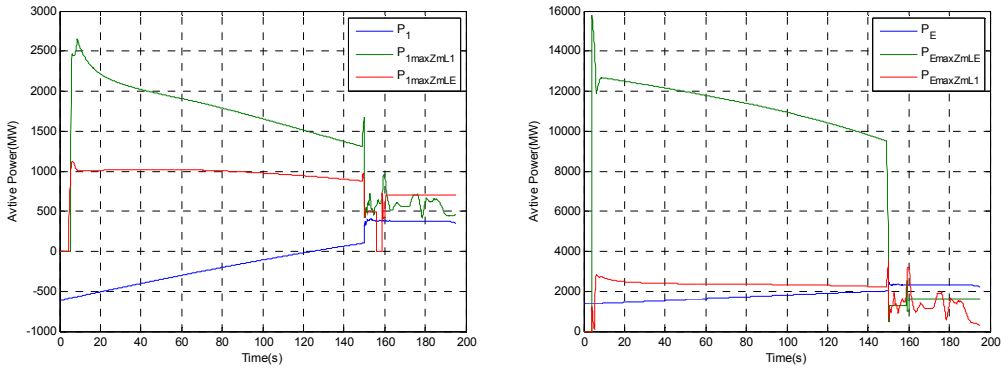


Figure 40. Voltage stability limits results of voltage collapse scenario.

2.9 Conclusion

A new measurement-based method for real-time voltage stability monitoring of a load area fed by multiple tie lines has been proposed. The new method is based on an *N*+1 buses equivalent system, whose parameters are estimated directly from synchronized measurements obtained at the boundary buses of the load area. For each tie line, the method calculates the transfer limit and margin against voltage instability analytically from that

estimated equivalent system. The new method has been demonstrated in detail on a 4-bus system and then tested by case studies on a 140-bus NPCC system model and detailed NYISO model.

Compared to a traditional TE-based method for measurement-based voltage stability monitoring, the new method has two apparent advantages. First, the new method offers detailed limit and margin information on individual tie lines to identify the tie line and boundary bus with the smallest margin as the location where voltage instability more likely initiates. Second, as demonstrated on the 4-bus system, before the voltage collapse point, the total tie-line flow limit from the new method is more accurate than the limit from the TE-based method. The latter fluctuates more and is not as flat as the former because the TE-based method does not model the weak or strong connection between boundary buses. The above second advantage makes the new method more suitable for online monitoring and early warning of voltage instability, and the first advantage can help the system operator to identify the location where voltage instability more likely initiates and accordingly choose more effective control resources, e.g., those having shorter electrical distances to the tie line with the smallest margin.

CHAPTER 3

THE *N*-1 SENSITIVITY ANALYSIS OF *N*+1 BUSES EQUIVALENT MODEL

3.1 Introduction

The *n*-1 contingency analysis gives the criticality of the post-outage voltages and power flows to show that which contingencies is more critical. In order to assess the voltage stability margins for the proposed MBVSA method, two sensitivities need to be studied, which are the sensitivity of the parameters of the equivalent and the sensitivity of the tie line flow under *n*-1 contingency.

For the equivalent system parameter sensitivity, the proposed method is based on the power flow data, due to the specific *N*+1 model, the sensitivity analysis is derived from the *N*+1 buses equivalent system.

To determine post-outage quantities in performing contingency analysis, the Sensitivity and Distribution Factor (DF) methods are widely utilized. Sauer finds Line Outage Distribution Factors (LODFs) using admittance values in [60] to determine the real power line flows. Then in [61], a improved technique based on phasor measurements was proposed. In [62], Ilic and Phadke used the decoupled method to estimate the distribution factors to determine reactive power line flows. In [63], Singh and Srivastava have obtained the P-δ and Q-V relationship based on the load flow Jacobian matrix. However, this method still required the $\mathbf{Y}_{bus}$ matrix.

In this chapter, the sensitivity analysis of *N*+1 buses equivalent model has been addressed. With all equivalent parameters estimated, the proposed sensitivity analysis method will provide both equivalent parameter sensitivity and tie line power flow sensitivity. Therefore, the *n*-1 margin will be predicted with these two sensitivity studies.

3.2 Sensitivity Analysis for *n*-1 Contingency

There are two parts in this section, one is about the impedance sensitivity analysis for *n*-1 contingency, and the other is the sensitivity analysis of the line power transfer. With those two sensitivity analyses, the margins of the power transfers on the tie lines for post-contingency will be derived.

3.2.1 *n*-1 Contingency Sensitivity Analysis for Equivalent Model

Once the **Y** matrix for the load area is calculated, the equivalent can be derived by eliminating all the buses except for the boundary buses and obtain the **Y** matrix for the reduced network.

Firstly, replace the external system of the load area with *N* hypothesis voltage sources $\overline{E}_1 \sim \overline{E}_N$. As it is shown in Figure 41, the original load area forming by *R* buses has been connected by *N* tie lines between boundary buses and *N* hypothesis voltage sources.

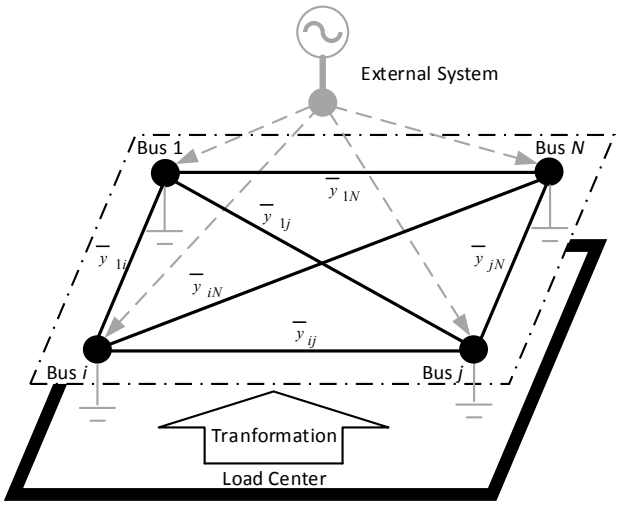


Figure 41. System transformation.

To reduce the system, all loads in the load center will be converted to equivalent admittances to ground, and all generators in the load center will be considered as negative loads and converted to equivalent admittances to ground. Since these load admittances and generator admittances are added to the diagonal elements in the matrix, the off-diagonal elements will not be influenced by this transformation. The transformed admittance for load or generator on bus *i* is:

$$y_{Ti} = \frac{\overline{S}_i^*}{\left|\overline{V}_i\right|^2} = \frac{P_i - jQ_i}{\left|\overline{V}_i\right|^2} \tag{3-1}$$

With the updated $\mathbf{Y}_{bus}$, the node equation $\mathbf{I}_{bus} = \mathbf{Y}_{bus}\mathbf{V}_{bus}$ for this system can be written as:

$$\begin{bmatrix} \mathbf{I}_N \\ \mathbf{0} \end{bmatrix} = \begin{bmatrix} \mathbf{Y}_{NN} & \mathbf{Y}_{RN} \\ \mathbf{Y}_{NR} & \mathbf{Y}_{RR} \end{bmatrix} \begin{bmatrix} \mathbf{V}_N \\ \mathbf{V}_R \end{bmatrix} \tag{3-2}$$

where $\mathbf{I}_N$ represents the vector of the injected bus currents to the load center, $\mathbf{Y}_{NN}$, $\mathbf{Y}_{RR}$, $\mathbf{Y}_{RN}$ are respectively the admittance matrix for N hypothesis voltage sources $\overline{E}_1 \sim \overline{E}_N$, the admittance matrix for the load center, and the off-diagonal elements of the admittance matrix of this system. Since the admittance matrix is symmetrical, $\mathbf{Y}_{RN} = \mathbf{Y}_{NR}$.

Expanding equation (3-2),

$$\begin{aligned} \mathbf{I}_N &= \mathbf{Y}_{NN}\mathbf{V}_N + \mathbf{Y}_{RN}\mathbf{V}_R \\ 0 &= \mathbf{Y}_{NR}\mathbf{V}_N + \mathbf{Y}_{RR}\mathbf{V}_R \end{aligned} \tag{3-3}$$

From which the $\mathbf{V}_R$ can be eliminated to find

$$\mathbf{I}_N = (\mathbf{Y}_{NN} - \mathbf{Y}_{NR}\mathbf{Y}_{RR}^{-1}\mathbf{Y}_{RN})\ \mathbf{V}_N \tag{3-4}$$

Therefore, the admittance matrix for the reduced N buses system is

$$\mathbf{Y}_{bus}^{red} = \mathbf{Y}_{NN} - \mathbf{Y}_{NR}\mathbf{Y}_{RR}^{-1}\mathbf{Y}_{RN} \tag{3-5}$$

The objective of this transformation is to obtain the equivalent transfer admittances of the load area connecting each boundary buses. Therefore, they can be directly fetched on the corresponding positions in $\mathbf{Y}_{bus}^{red}$.

In this transformation, all transient characteristics have been ignored, so even the PMU data are not available, the admittance matrix can still be derived from the power flow data. The load admittances and generator equivalent admittances only change the off-diagonal elements of the admittance matrix, so the transfer impedances, which are diagonal elements, will remain constant until the topology changes.

The external voltage source and external impedance will remain their values the same as the ones in pre-contingency state respectively, since we assume the n-1 contingency only happens within the load center. With aforementioned parameter

estimation of the equivalent system, the power transfer limits will be given in real time by performing the MBVSA calculation addressed in Chapter 2.

3.2.2 *n*-1 Contingency Sensitivity Analysis of Tie Line Flow

When assessing the post-contingency power transfer on tie lines, the Line Outage Distribution Factor (LODF) can be utilized with less computation burden and higher efficiency. Typically, it is used to determine the impact of a line outage on other system real power flows without having to explicitly solve the power flow for the contingency.

The required data for this method is the active power transfer of the tie line to be tripped as an *n*-1 contingency, and the system admittance matrix. These data can be easily found in the static power flow calculation, and there is no need to update it frequently.

The LODF is defined as

$$\tau_{ij,lm} = \frac{\Delta \overline{S}_{ij}}{\overline{S}_{lm}} \tag{3-6}$$

where $\Delta \overline{S}_{ij}$ is the power transfer change on the tie line from bus *i* to bus *j*, $\overline{S}_{lm}$ represents the power transfer of the outraged line.

The LODF will be based on the Power Transfer Distribution Factor (PTDF), representing the sensitivity of line loading with respect to bus demands. NERC defines a PTDF as "In the pre-contingency configuration of a system under study, a measure of the responsiveness or change in electrical loadings on transmission system Facilities due to a change in electric power transfer from one area to another, expressed in percent (up to 100%) of the change in power transfer".

The PTDF relating the power transfer $\overline{S}_{ij}$ on the line from bus *i* to bus *j* with respect to injected bus power $\overline{S}_k$ is denoted

$$\rho_{ij,k} = \frac{\Delta \overline{S}_{ij}}{\Delta \overline{S}_k} \approx \frac{\partial \overline{S}_{ij}}{\partial \overline{S}_k} \tag{3-7}$$

Expanding equation (3-7) with the voltage and current phasors,

$$\rho_{ij,k} = \frac{\partial \left[(\overline{V}_i - \overline{V}_j) / \overline{z}_{ij} \right]^* V_j}{\partial (\overline{V}_k \overline{I}_k^*)} \tag{3-8}$$

where, $\overline{z}_{ij}$ represents the transmission line impedance between bus *i* and bus *j*.

For the case of near unity bus voltage, the variation of the injected power was mostly lead by the variation of the current $\overline{I}_k$,

$$\rho_{ij,k} = \frac{\partial \left[(\overline{V}_i - \overline{V}_j) / \overline{z}_{ij} \right]^* V_j}{\partial (\overline{I}_k^*) \overline{V}_k} = \frac{\overline{V}_j}{\overline{V}_k} \frac{(\frac{\partial \overline{V}_i}{\partial \overline{I}_k} - \frac{\partial \overline{V}_j}{\partial \overline{I}_k})^*}{\overline{z}_{ij}^*} \tag{3-9}$$

Thus

$$\rho_{ij,k} = \frac{\overline{V}_j}{\overline{V}_k} \frac{(\overline{Z}_{ik} - \overline{Z}_{jk})^*}{\overline{z}_{ij}^*} \tag{3-10}$$

where, $\overline{Z}_{ik}$ and $\overline{Z}_{jk}$ respectively are the element at *i*-th row and *k*-th column, and the element at *j*-th row and *k*-th column of the impedance matrix $\mathbf{Z}_{bus}$, and $\mathbf{Z}_{bus} = (\mathbf{Y}_{bus})^{-1}$.

With PTDF $\rho_{ij,k}$ defined, the LODF $\tau_{ij,lm}$ is derived according to Figure 42.

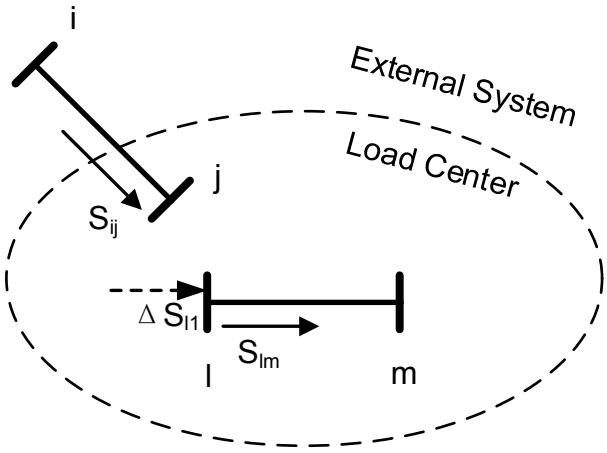


Figure 42. LODF step 1.

Firstly, add a hypothetical injection $\Delta\overline{S}_{l1}$ at bus l to decrease the line flow to 0, which means $\Delta\overline{S}_{lm} = -\overline{S}_{lm}$. Therefore, the tie line change $\Delta\overline{S}_{ij}^{'}$ will satisfy

$$\Delta\overline{S}_{ij}^{'} = \rho_{ij,l}\Delta\overline{S}_{l1} = \rho_{ij,l}\frac{\Delta\overline{S}_{lm}}{\rho_{lm,l}} = \rho_{ij,l}\frac{-\overline{S}_{lm}}{\rho_{lm,l}} \tag{3-11}$$

With aforementioned change, the line *i-j* was removed without changing the system operation state. Simultaneously, the impedance matrix $\mathbf{Z}_{bus}$ need to be updated according to this topology change. Additionally, The new PTDF $\rho_{ij,k}^{'}$ under this new system topology will be re-defined with new impedance matrix $\mathbf{Z}_{bus}^{'}$.

As shown in Figure 43, to eliminate the hypothetical injection, a new hypothetical injection $-\Delta\overline{S}_{l1}$ is added, so under the new system topology, the tie line change $\Delta\overline{S}_{ij}^{''}$ will satisfy

$$\Delta\overline{S}_{ij}^{''} = \rho_{ij,l}^{'}(-\Delta\overline{S}_{l1}) = \rho_{ij,l}^{'}\frac{\overline{S}_{lm}}{\rho_{lm,l}} \tag{3-12}$$

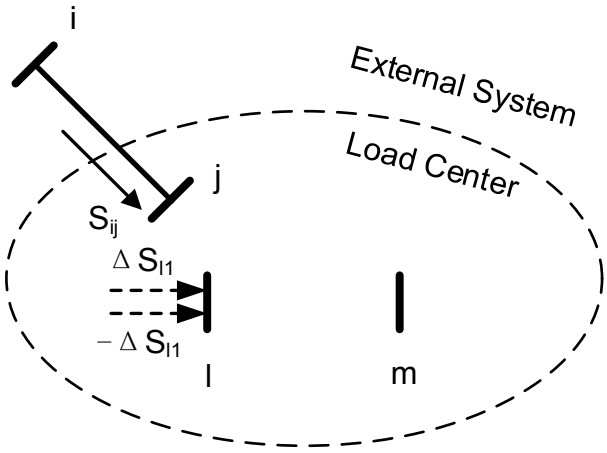


Figure 43. LODF step 2.

After the aforementioned two steps, two changes of tie line *ij* power flow calculated by PTDF are $\Delta\overline{S}_{ij}^{'}$ and $\Delta\overline{S}_{ij}^{''}$. Summate them up, and plug in both expressions,

$$\Delta\overline{S}_{ij} = \Delta\overline{S}_{ij}^{'} + \Delta\overline{S}_{ij}^{''} = \frac{\rho_{ij,l}^{'} - \rho_{ij,l}}{\rho_{lm,l}}\overline{S}_{lm} \tag{3-13}$$

Thus,

$$\tau_{ij,lm} = \frac{\rho_{ij,l}^{'} - \rho_{ij,l}}{\rho_{lm,l}} = \frac{\overline{V}_j}{\overline{V}_m}\frac{z_{lm}^{*}(Z_{il}^{'} - Z_{jl}^{'})^{*} - z_{lm}^{*}(Z_{il} - Z_{jl})^{*}}{z_{ij}^{*}(Z_{ll} - Z_{lm})^{*}} \tag{3-14}$$

where all the impedances in (3-14) will be derived directly from the impedance matrix of the system. $\overline{V}_j$ and $\overline{V}_m$ can be obtained from either the state estimator or the PMU measurements. If both state estimation results and measurements are not available, the assumption $\overline{V}_j = \overline{V}_m$ will be made to get the LODF.

The power transfer changes of all tie lines will be estimated by (3-13) and (3-14). Compared with power flow calculation, this proposed method can be applied with much less computation burden and very fewer measurements are required.

3.3 Implementation of the *n*-1 Contingency Sensitivity Analysis

In order to avoid the error caused by the LOPF, a hybrid approach need to be utilized. In this hybrid approach, besides the admittance matrix, the results from state estimator are also considered as a critical information source.

As shown in the Figure 44, at the 1st stage, this method does not need a converged state estimation solution. The parameter estimation for load center only requires the admittance matrix of the power grid, and the power flow sensitivity algorithm only needs the admittance matrix and the reactive power transferred on the line with *n*-1 scenario consideration.

When there is a state estimation solution, it is utilized to do an *n*-1 contingency screen to compare its results with the results coming from the power flow sensitivity.

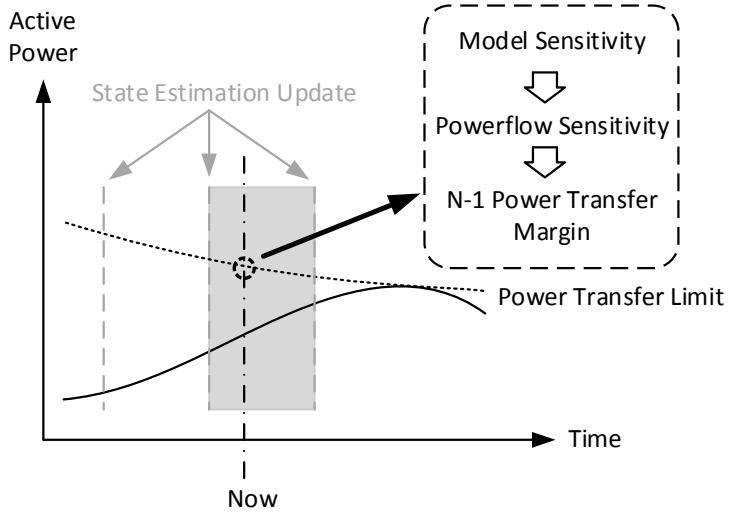


Figure 44. Implementation of the *n*-1 contingency sensitivity analysis.

3.4 Case Studies

The NPCC 48-machine, 140-bus system model was utilized to verify the *n*-1 contingency sensitivity analysis algorithm proposed. The system models are as same as the one used in Chapter 2. In Figure 45, a Connecticut Load Center (CLC) area is supported by three tie lines, i.e. 73-35, 30-31 and 6-5. Powertech's TSAT is also used to simulate all *n*-1 contingency scenarios about the CLC area.

Simulation results on the voltages at boundary buses 35, 31 and 5 and the complex powers of the corresponding three tie lines are recorded at 30Hz, i.e. the typical PMU sampling rate. The raw data are preprocessed by an averaging filter over 15 samples to be downgraded to 2Hz. The processed data are then fed to the new method for estimating the external and load area parameters and calculating transfer limits. The new method is performed every 0.5s on data of the latest 5-s time window.

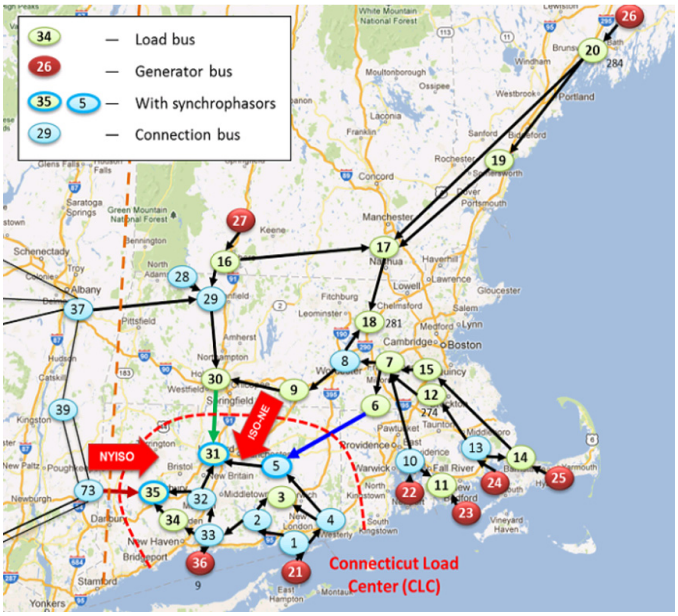


Figure 45. Map of CLC area.

According to the *n*-1 contingency screening results in the load area, the most critical *n*-1 contingency has been selected to demonstrate the sensitivity analysis algorithm: all loads of the load center are uniformly increased by a total of 1.53 MW per second from its original load of 1906.5 MW with constant load power factors; at *t*=200s, the transmission line between bus 4 and bus 5 is tripped, which pushes the system to be close to the voltage stability limit; after another 200s load increase, voltage collapse happens around *t*=400s as shown in Figure 46 on three boundary bus voltages.

Figure 47 indicates the PV curves monitored at three boundary buses.

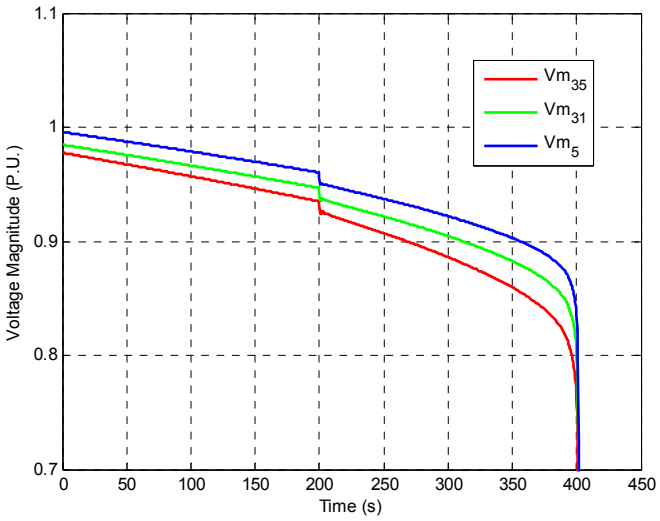


Figure 46. Voltage magnitudes at CLC boundary buses.

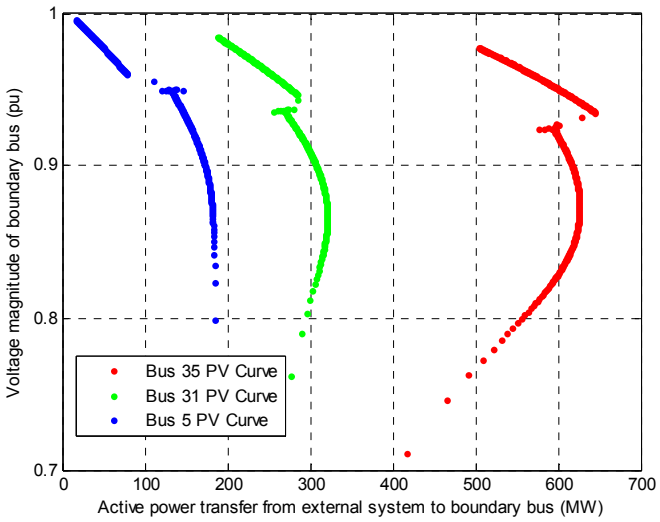


Figure 47. PV curves.

3.4.1 Verification of the Impedance Sensitivity Analysis for *n*-1 Contingency

In the impedance sensitivity analysis for *n*-1 contingency, in order to simplify the system, the external system of the load area has been replaced with *N* hypothesis voltage sources, and all loads in load center have been converted to equivalent admittances to ground, so do all generators. Therefore, the accuracy of the transformation needs to be verified. As shown in Figures 48 and 49, the conductances and susceptances of all three transfer admittances have been compared separately using the most critical *n*-1 contingency. With the dynamical simulation data, the conductances and susceptances are calculated following the steps discussed in Chapter 3.2. These two figures clearly show that the transfer admittances will remain constant if there is no system topology change; even the load and generation vary all the time.

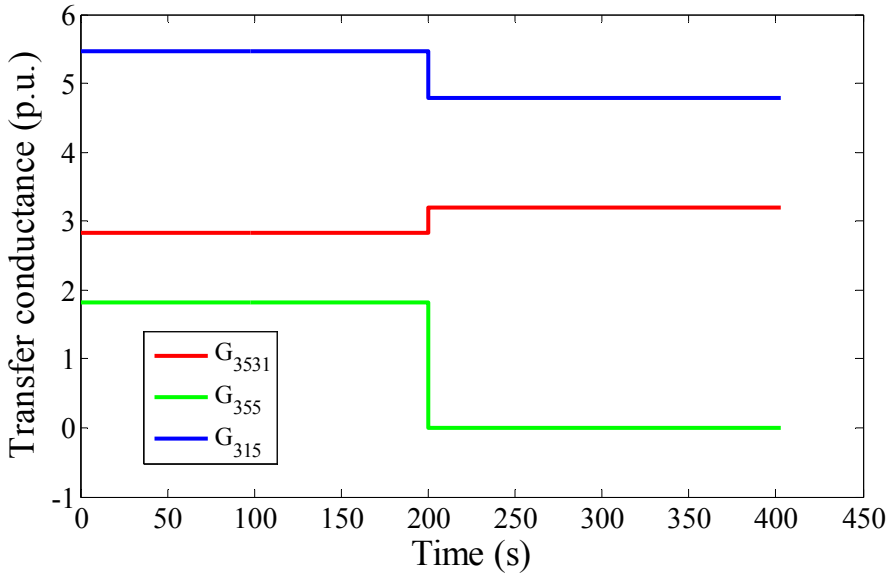


Figure 48. Transfer conductance comparison.

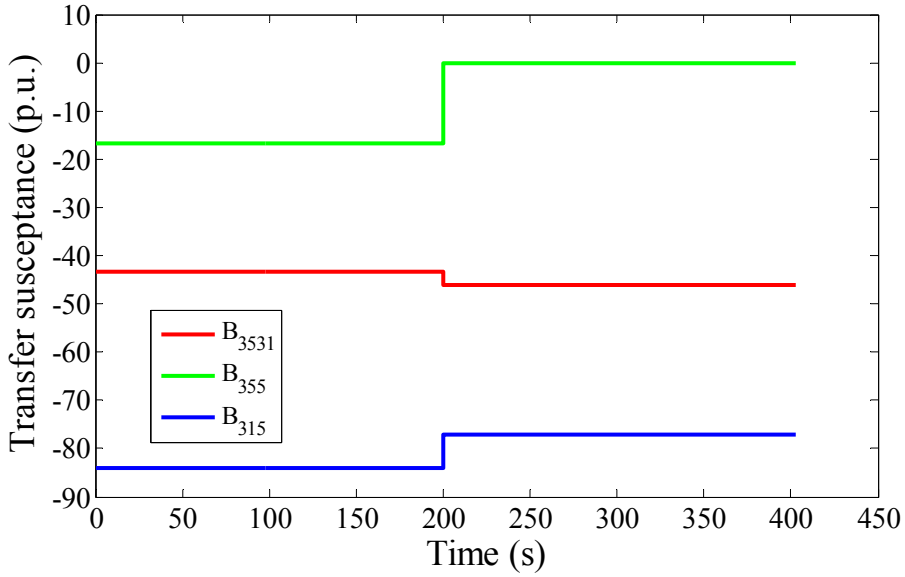


Figure 49. Transfer susceptance comparison.

3.4.2 Verification of the Tie Line Power Flow Sensitivity for *n*-1 Contingency

The Line Outage Distribution Factor (LODF) has been utilized to determine the tie line power flow sensitivity for *n*-1 line outage contingency. Comparing with the power flow calculation, LODF was solved explicitly and needs no iterations. To verify the accuracy of the LODF method, all 12 *n*-1 line outage contingencies for the load area are simulated and the post-contingency power flow results are compared. In Table 2, the errors of the LODF method are compared with the actual simulation results for the most critical tie line 73-35 in terms of percentage error of the tie line power transfer. In conclusion, the average error will be less than 3%, which shows a good accuracy.

Table 2. Errors of the LODF

Contingency	Error	Contingency	Error
1. Line 4-5 trip	0.56%	7. Line 33-34 trip	-1.92%
2. Line 5-31 trip	-2.59%	8. Line 1-2 trip	-2.51%
3. Line 1-4 trip	-0.90%	9. Line 34-35 trip	-0.52%
4. Line 32-33 trip	-2.03%	10. Line 32-35 trip	2.09%
5. Line 2-33 trip	2.07%	11. Line 3-4 trip	-0.17%
6. Line 31-32 trip	2.19%	12. Line 2-3 trip	-0.04%

3.4.3 *n*-1 Contingency Sensitivity Analysis Study

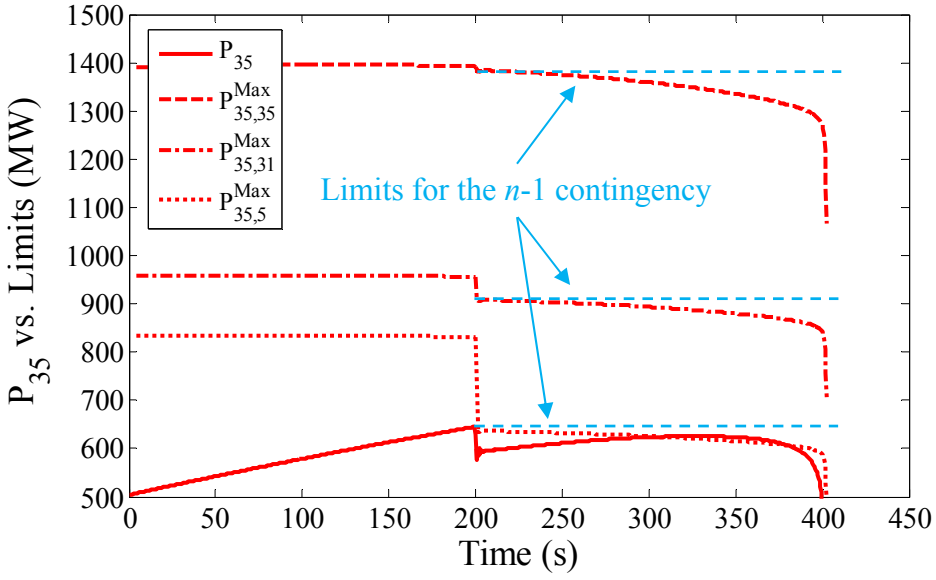
Sensitivity analysis is conducted on the calculated voltage stability limits under *n*-1 tie line trip contingency. Figure 50 gives the results from the proposed *n*-1 contingency

sensitivity analysis. Before the *n*-1 line trip contingency happened, all the lines have sufficient margins to their limits. The *n*-1 contingency sensitivity analysis module kept computing the power transfer limits under *n*-1 conditions. As shown in Figure 50, *n*-1 limits are the blue dashed lines from 200s to 400s. When the *n*-1 line trip happened, the dynamical system moved to a critical status immediately with less stability margin, and the actual active powers of the three tie lines are approaching to their limits. Comparing with the actual limits, all nine *n*-1 limits have a high accuracy on predicting the actual limits under *n*-1 condition.

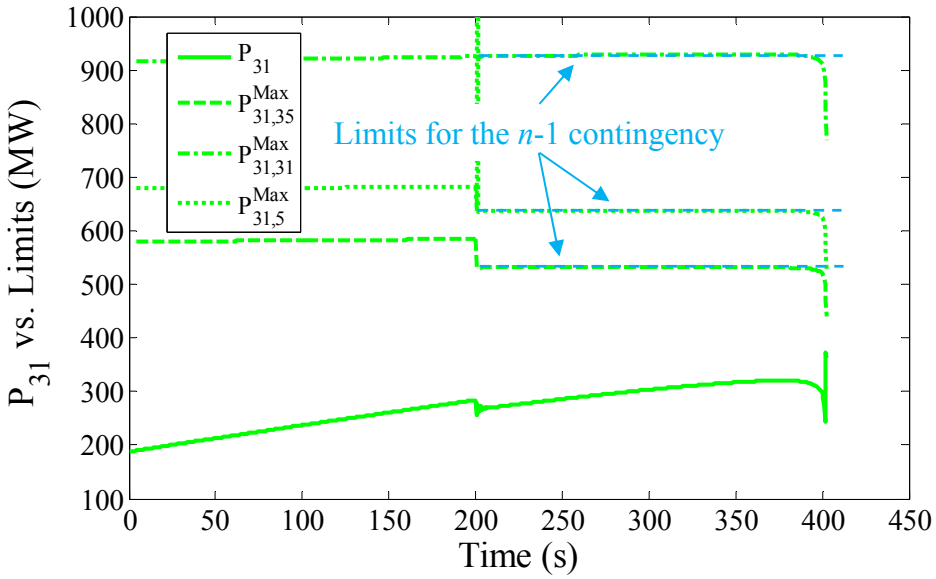
After the *n*-1 line trip happened, P_{35} of tie line 73-35 is the most critical tie line due to its significant small margin. As loads keep increasing, P_{35} reaches the limit $P_{35,5}^{\text{Max}}$ at t=307s. From Figure 50 (b) and (c), the other two lines keep positive margins until the final voltage collapse. After another 100s, the voltage collapse happened.

The *n*-1 line trip contingency analysis actually offers a way to screen the contingencies need to be conducted in the simulation, since the limit and margin information on individual tie line will tell the operators in real time, which contingency will be more critical than the others. By receiving such information, a huge number of unimportant simulations will be skipped and only the most critical ones will be adopted. Therefore, the operators will have enough time to run the simulation and find the optimized remedial action before system collapse.

Figure 50. Transfer limits of each tie line under *n*-1 line trip contingency.

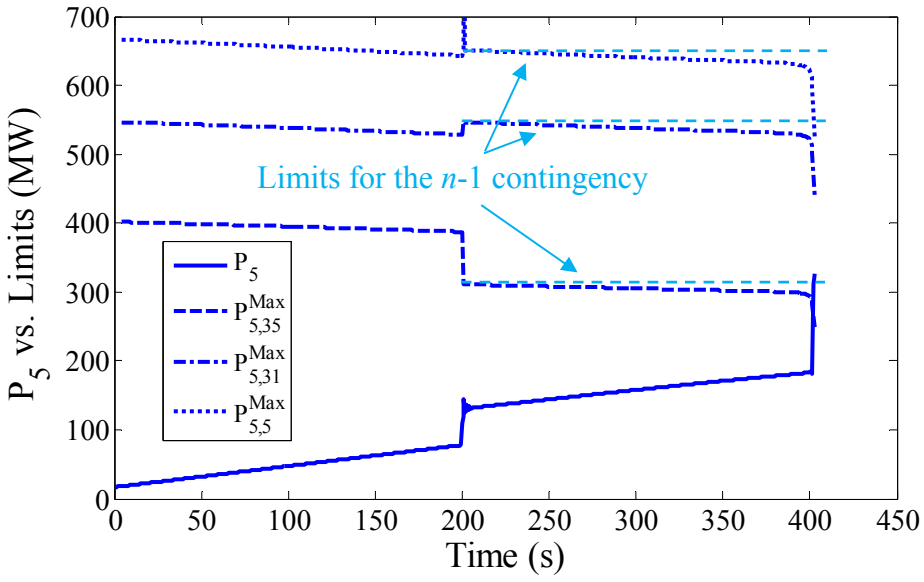


(a) P35 vs. its limits.



(b) P31 vs. its limits.

Figure 50 continued



(c) P5 vs. its limits.

Figure 50 continued

3.5 Conclusion

The *n*-1 sensitivity analysis has been adopted by the MBVSA method. With this sensitivity analysis, the MBVSA is able to provide the stability margins under *n*-1 sensitivity. There are two sensitivities have been studied, which are the parameter sensitivity of the equivalent system and the sensitivity of the tie line flow under *n*-1 contingency. Consequently, *n*-1 stability limits can be predicted with much less computationally intensive by this method.

CHAPTER 4

REAL-TIME HYBRID VOLTAGE STABILITY ASSESSMENT

4.1 Introduction

To accurately foreseeing and screen the critical contingencies in the future, one of the promising methods is the dynamic simulation by solving the differential and algebraic equations of the power system. It not only captures the dynamic characteristics of the system, but also can help the operator with remedial actions recommended. However, the inevitable heavy computation burden limits its online applications, and how to make up this drawback is one of the most important research topics recently [64]. In this chapter, a hybrid voltage stability assessment method is designed to take the advantage of complementary benefits of simulation-based and measurement-based methods for VSA. The framework for this real-time hybrid voltage stability assessment is also presented.

4.2 Proposed Framework

The proposed framework is composed of high-performance dynamic simulation analysis tool and MBVSA algorithm. To provide real-time situational awareness against the critical voltage instability contingencies, the dynamic simulation analysis tool provides the information for "*what if*" scenarios such as the stability limits and margins during the *n*-1 contingency conditions. It relies also on the model of the system to provide recommendations for preventive control actions based on scenario analysis. The MBVSA algorithm provides *n*-0 level stability margins and *n*-1 level stability margins to help screening the contingencies need to be conducted for the simulation, and evaluate the

criticality of the system when simulation results are not available. It also contributes to identify vulnerable regions and critical components of the system, and enables model reduction and external system equivalencing. The integrator module receives as an input all the information and results generated by the MBVSA and simulation-based modules and provides the hybrid approach intelligence, which combines the complementary strengths of both approaches. It manages, coordinates, analyzes and processes results from the different modules to generate actionable information with focus on the operator's perspective. The actionable information can be in the form of:

1. Offering the operators with real-time voltage stability margins;
2. Alerting the operators causing by the simulation violations, such as exceed the predefined threshold for stability limits, *n*-1 violations when there is the critical contingencies happen;
3. Recommending the remedial control actions to present the system from instability;
4. Automatically trigging the emergency control actions.

Representative examples of the analysis and decision points of the integrator module, formulated as rule-based actions, include the following:

1. The MBVSA module keeps running to assess the current *n*-0 stability status and doing the contingency screening using *n*-1 sensitivity analysis in Chapter 3.
2. If the voltage stability margin for *n*-0 condition or the predicted margin for *n*-1 condition is low (close or below a predefined threshold), the simulation-based

module is triggered to identify and recommend preventive control actions to prevent system instability.

3. If violations of voltage criteria are identified for any *n*-1 contingency, the emergency control actions are automatically or manually triggered by the operator.

Figure 51 depicts a high-level structure of the integrator module and its hybrid intelligence, as part of the integrated hybrid scheme for online VSA under the hybrid framework we have developed with EPRI under a US DOE project [55].

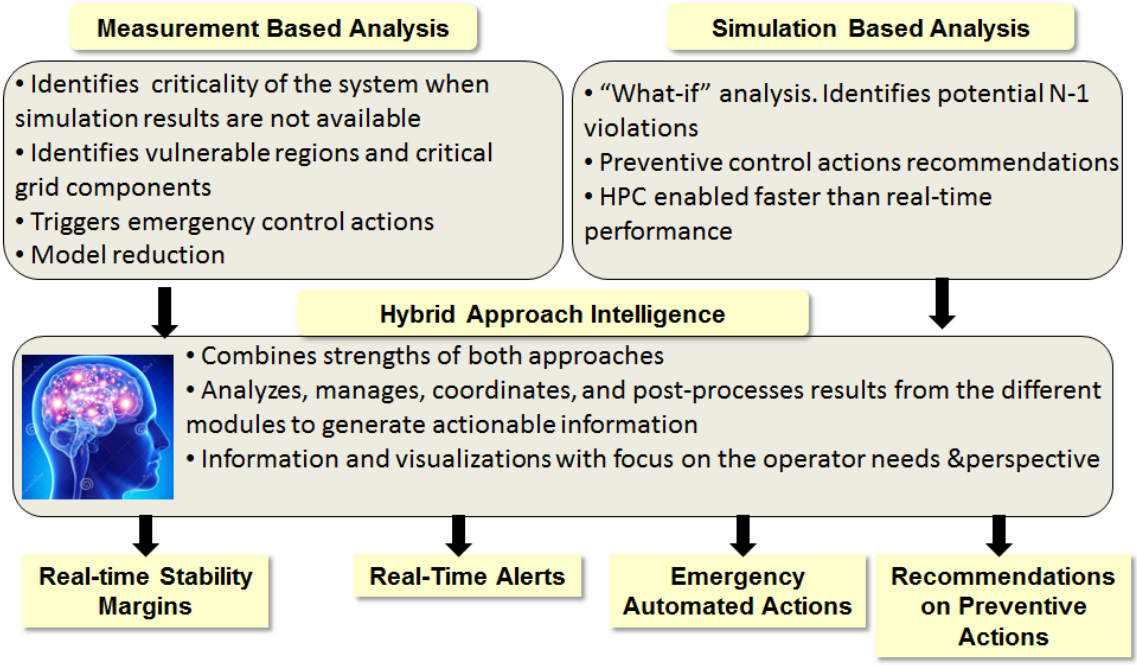


Figure 51. Hybrid approach intelligence.

4.3 Implementation Studies

The use of the proposed hybrid framework is demonstrated here by an pre-designed example. The objective is to walk the reader through the entire process, simulating how the system would evolve during a contingency situation, how the operator would react based on the information from the VSA scheme, and how operator's intervention would affect the system.

The same 140-bus NPCC system is used as the test system in this chapter. Here, the most critical *n*-1 line trip contingency in Chapter 3 is utilized as shown in Table 3, but with simulation-based module enabled. For the contingency in Chapter 3, the load ramping rate is 1.53 MW per second; and the line 4-5 is tripped at t=200s; after another 200s load increase, voltage collapse happens around t=400s. However, in the following contingencies, the remedial action will be triggered to prevent the system from collapse.

Table 3. Margins of all *n*-1 line trip contingency at 200s

Contingency	Margin(MW)	Contingency	Margin(MW)
1. Line 4-5 trip	33	7. Line 33-34 trip	67
2. Line 5-31 trip	54	8. Line 1-2 trip	67
3. Line 1-4 trip	57	9. Line 34-35 trip	72
4. Line 32-33 trip	60	10. Line 32-35 trip	75
5. Line 2-33 trip	62	11. Line 3-4 trip	76
6. Line 31-32 trip	63	12. Line 2-3 trip	78

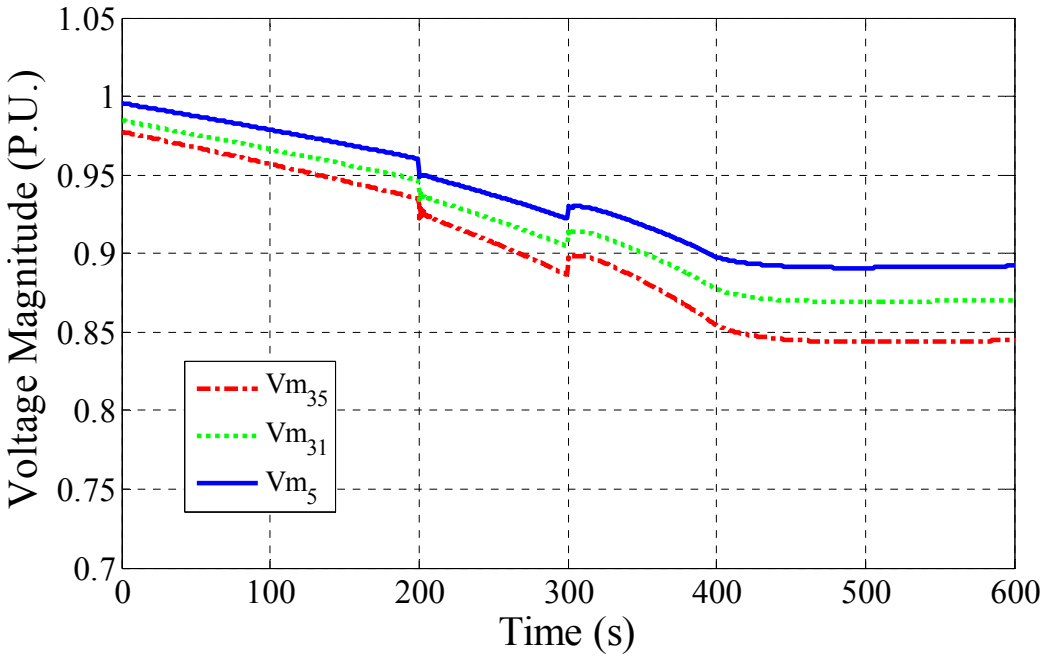


Figure 52. Voltages of three boundary buses.

This scenario is shown in the following three stages, and they are three operating points of the system before and after the contingencies or remedial action, which are shown in Tables 4.

Table 4. Stages of the simulated instability scenario

Stage 1	No Contingency
Stage 2	Line 4-5 tripped
Stage 3	Remedial action triggered

At the first stage, there is no contingency and the system is operating securely under *n*-1 criteria. Note that the *n*-1 limit for the worst contingency (in this scenario the worst contingency is the line 4-5 trip) is provided to the operator by the measurement-based VSA module (i.e. the MBVSA algorithm) when the *n*-1 margin is lower than a pre-designed threshold. In addition, the limit for the current operating point is also calculated by MBVSA. Note that in this case MBVSA may underestimate the voltage stability limit under the "*n*-0" condition. This inaccuracy of MBVSA algorithms far from the instability point has been also reported in previous work. However, at this stage the stability limit value is not important since the margin is quite adequate. At this stage, the MBVSA provides the *n*-0 limits for the operators, and take an action if *n*-0 limits were hit. On the other hand, the MBVSA calculates *n*-1 margin to determine whether to trigger the simulation-based module. The stage 1 is shown in Figure 53, illustrating the power transfer limits on the three tie lines.

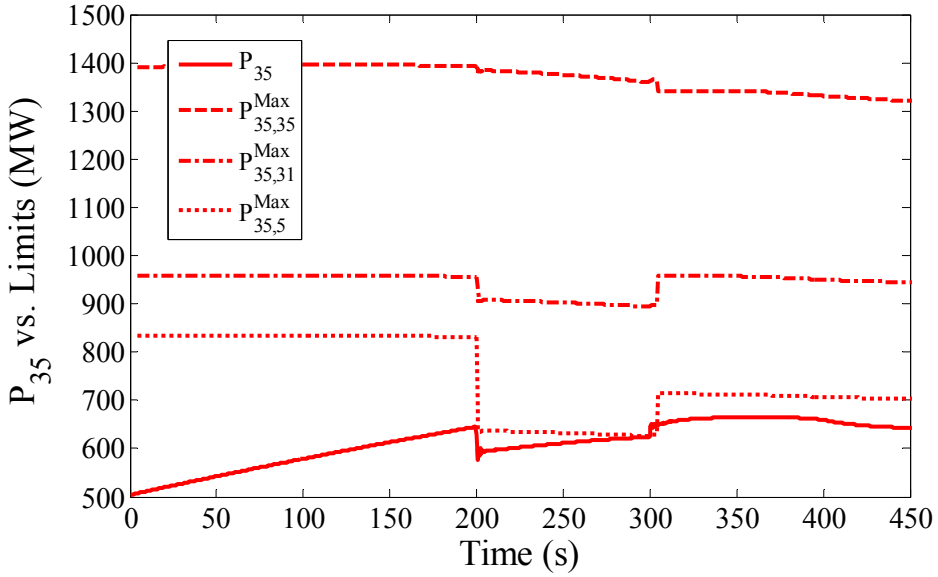
During Stage 2, upon the line 4-5 trip, the system operates under a contingency. Immediately after the contingency, the limits estimated by the MBVSA is changing, means there is an event happened. Based on the MBVSA results, the simulation-based module has been activated automatically to perform the simulation to recalculate the *n*-1 limit, and provides an alert to the operator to trigger simulations to test remedial actions to bring the system back. Note that before the simulation performed by the simulation-based module, the operator can have the margin information which is still sufficient for the present operating condition, so no emergency actions will be triggered. Thus, after the *n*-1 limits are estimated, the results are superposed on the MBVSA results and the additional

information is provided to the operator. The stage 2 is shown in Figure 53. Note that the operating condition under Stage 2 violates the *n*-1 criteria, so there will be an alert to the operator to inform him of this violation so that the remedial control action will be triggered to prevent the system from collapse.

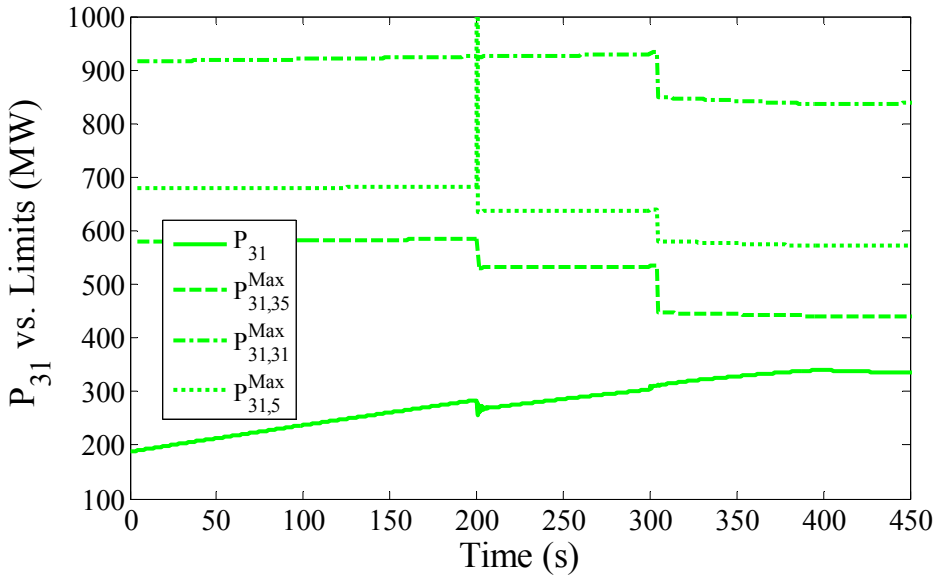
If the operator did not take any corrective action after the system pass through the saddle point bifurcation, which is determined by the MBVSA module, the system may engage voltage collapse. However, the MBVSA will take a pre-designed emergency control automatically if a predefined threshold is triggered. Note that, this threshold is predefined according to the multiple offline case studies and the experiences of the skilled operators.

If during the Stage 2, the simulation successfully provided a remedial action, the time remedial action triggered tells that the system is at Stage 3 of operation. Note that the MBVSA module is also critical at this stage because it provides situational awareness for the operator on the criticality of the system condition, when there is no enough time to perform additional simulations. The stage 3 is shown in Figure 53. The effect of a corrective action, suggested by the integrator module, has been also simulated and is shown in Figure 53. In particular, additional reactive power was dispatched in the system at 300s. Finally, the voltage collapse is prevented, and the system is no longer under emergency condition. In order to bring the system back to secure status, some other actions can be done immediately.

Figure 53. Scenario demonstration.

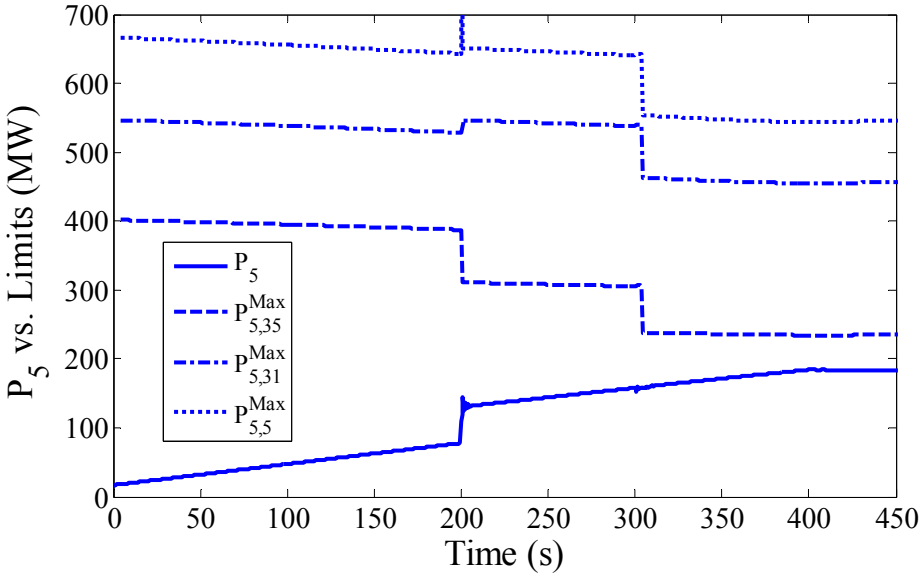


(a) P35 vs. its limits.



(b) P31 vs. its limits.

Figure 53 continued



(c) P5 vs. its limits.

Figure 53 continued

4.4 Considerations for Practical Implementation

The underlying principle of the framework is to improve operator situational awareness, provide operators with an evaluation of events likely to occur and their impact on the system, alert operators of any imminent critical condition, and provide them with guidance of effective mitigating measures to implement. This framework also provides the operators with remedial action recommendation, and it can be implemented as a simple rule-based approach in the form of "*if-then*" rules. With the simulation tools, it can trigger automatic actions such as contingency screening, critical condition alert or remedial actions.

A representative set of actions that may take place in practical implementation of the framework can be summarized as follows:

1. Start with recent State Estimator (SE) solution;
2. Conduct PV curve analysis to calculate transmission limits on the selected interface, and calculate stability margins;
3. Verify and refine stability limits using dynamic simulation tool;
4. Operate the system and keep track on system operating conditions to ensure the system remains within the voltage stability limits;
5. Continuously calculate voltage stability margin using PMU data (MBVSA) in terms of MW transfer limit;
6. If a sudden change in MBVSA stability margin occurs, consider it an indication of a system event that has an influence on voltage stability performance;

7. If the margin goes below Level 1 threshold, perform simulation to identify potential risk of instability and define remedial/preventive actions;
8. If the margin continues to decrease and crosses Level 2 threshold, select and implement appropriate remedial actions.

In addition, practical implementation of the integrator computation platform will require standard models to facilitate effective information and data flow among the different modules. The use of standard data models for information sharing means that the different analytic modules can gather the input data they need and share their results electronically without the need for manual data assembly or transfer.

4.5 Conclusion

The real-time hybrid voltage stability assessment for load area has been proposed and tested on the NPCC system. With this framework, the hybrid method is able to take the advantage of simulation-based and measurement-based methods for system stability awareness, remedial action recommendation and real-time stability margins under both *n*-0 and *n*-1 conditions. It is a well-designed hybrid method for real-time application and decision maker.

CHAPTER 5

DEMONSTRATIONS ON THE CURENT HARDWARE TEST BED SYSTEM

5.1 Introduction

To validate and test the performance of the proposed MBVSA on the physical power system, we utilized the CURENT Hardware Test Bed (HTB) system which is a power electronic converter-based research and experiment platform to do the benchmark test. Another purpose is to demonstrate a closed-loop control strategy on the physical system. Therefore, in this chapter, we are focusing on the implementation of the MBVSA and the closed-loop control strategy on the HTB system. This new strategy is also based on an N+1 buses equivalent proposed by Reference [57] for calculating real-time voltage stability margins on individual tie lines of a load area. Two voltage stability scenarios are designed and implemented on the HTB system that emulates a three-area power system integrating conventional generation, wind generation, and multi-terminal HVDC transmission. The tests validate the effectiveness of real-time monitoring and closed-loop control against voltage instability of a physical power system.

As the transmission network operates closer to its loading limit, the difficulties for monitoring and controlling to maintain the voltage stability have been raised significantly. In order to help the operators foresee potential voltage instability and take control action promptly to mitigate the critical instability, online VSA and closed-loop control are key functions in power system operations.

Traditionally, model-based VSA methods have been utilized to identify the stability indices, and they have been discussed in many literature, such as continuation power flow method (CPFLOW) [12] [65], singular value decomposition [66], sensitivity method [18], and bifurcation theory [67]. However, these model-based tools highly rely on the fidelity in modeling of generation, load, and transmission facilities. Inaccurate models may result in inaccurate VSA results, leading operators to make incorrect decisions and hence increasing the risk of voltage collapse [68].

With real-time wide-area measurement data available to monitor buses vulnerable to voltage instability, MBVSA methods have been proposed [46-48]. Among all MBVSA methods, the TE theorem is widely used to represent the whole power system to a TE circuit. Based on this theory, various voltage stability indicators have been introduced [51] [53]. By assuming that the load power factor is constant, the power transferred to the load bus reaches its maximum when that external Thevenin impedance has the same magnitude as the load impedance.

However, as illustrated in [53], a TE based method may not provide accurate voltage stability margin for each of multiple tie lines together feeding a load area. When the connections between boundary buses are weak, tie lines may reach their power transfer limits at different time instants. By considering the relationship of connection, the new MBVSA method proposed in reference [57] offers detailed margin information on all individual tie lines and actually predicts the voltage collapse by the multistage warning events in terms of active power stability margin, which is brought about by modelling the relationship between all tie lines and monitoring them separately.

The purpose of the monitoring is not only to inform the operators about the stability of the current system, but to help the operators to take preventive control to move the system operation state away from possible voltage collapse by increasing the system stability margin. Although some literature proposed the strategy for preventive control and emergency control, most of them are using the computer simulation result or history data due to the irreproducible voltage collapse scenario for the actual power system operation state. The computer simulation may encounter numerical oscillation due to discontinuities and interpolation without proper selection of integration method [69]. Furthermore, computer simulation tools usually ignore the field issues such as the measurement error, time delay, non-linearity, electromagnetic interference, etc. which may impact the results significantly.

All of the above reasons stimulate the development of a multi-purpose testing facilities for the measurement-based voltage stability monitoring and closed-loop control application. A few test beds have been built, which, however, mostly adopt low voltage or medium voltage [70-75]. No development of a more complicated or representation of a higher voltage power system testing facility has been reported yet. The bottleneck of such a platform mainly lies in the high cost and the difficulty of scaling machines.

The CURENT has recently built an HTB system, which is a reconfigurable power electronic converter-based power grid emulator operated as a real-time power system with measurement, communication and actuation infrastructures [76-83]. It can be utilized to test real-time monitoring and closed-loop control methods for power grids. Compared with computer simulation, the HTB has the following advantages: 1) broad time scales – able to

emulate transients from microseconds for power electronics to milliseconds and seconds for power system events; 2) integrates real-time communication, protection, control, and cyber security; 3) able to test the reliability of the system by incorporating real communication, measurements, and various protection and control; 4) provides a platform for research on converter control and design in utility applications, such as AC/DC microgrid; 5) capable of performing prolonged real-time experiments, and demonstrating detailed system variable information simultaneously; 6) less dependency on numerical calculation, while allowing more flexibility of the whole system.

This chapter describes the proposed preventive control strategy, the HTB architecture and the implementation. To validate the new MBVSA, two scenarios are designed and tested using preventive control strategy [84] [85].

5.2 Settings and Scenarios of Demonstrations

As the number of wind farms increases, the importance of effective utilization of reactive power generation capabilities with wind farms to improve the grid voltage stability becomes more significant. To demonstrate the feasibility of the wind farm VAR support against voltage collapse, the VAR support from the wind farms has been chosen as the primary preventive actions.

As shown in Figure 54, the transmission line is working at the operating point A when the system is running under the normal operating condition initially. After load gradually increases and meets the control threshold at point A', the preventive control is triggered. The shunt VAR compensation helps the system to switch to state B on a new PV curve with better voltage stability. Considering additional load increasing, the system will

move to B’ when the load stops increasing, where the stability margin is larger than that at A’.

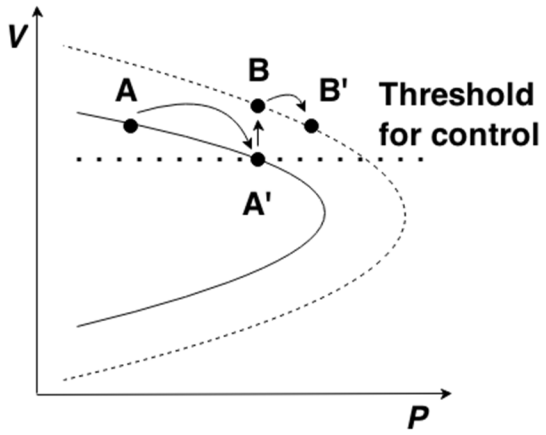


Figure 54. Trajectory of transmission line PV curve with preventive control triggered.

After the installation of the proposed closed-loop control system for tie lines of a pre-selected load area, the real-time parameter estimation is performed. The power transfer limit calculation continues providing the limits using system parameters estimated. When voltage stability margin on any tie line drops to a pre-designed threshold, the preventive action will be activated immediately to perform the aforementioned shunt compensation. The proposed closed-loop control strategy has been summarized in the following steps:

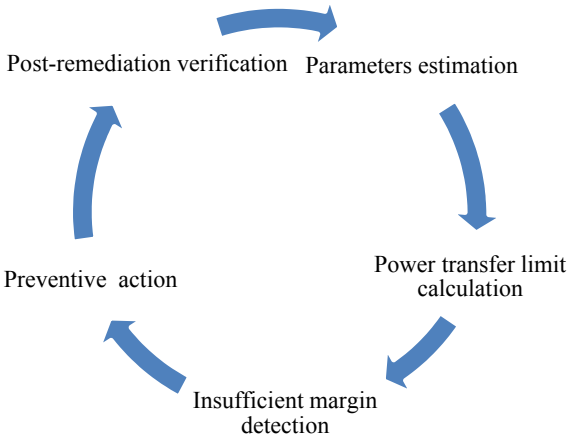


Figure 55. Closed-loop control strategy.

To implement the control strategy on the HTB, the following control structure design has been made. For the control and visualization purpose, NI LabVIEW has been utilized to emulate control centers in power systems. It gathers data from PMUs, and sends supervisory control commands to emulators with the HTB. Each emulator is implemented with a Texas Instrument DSP TMS320F28335, which receives commands (start and stop of the emulators) or data (wind speed, radiation, load consumption, etc.) from, and sends data to the NI CompactRIO through the CAN bus, as shown in Figure 56. With NI CompactRIO, the HTB can be controlled remotely by LabVIEW from the visualization and control center.



Figure 56. HTB control and communication structure.

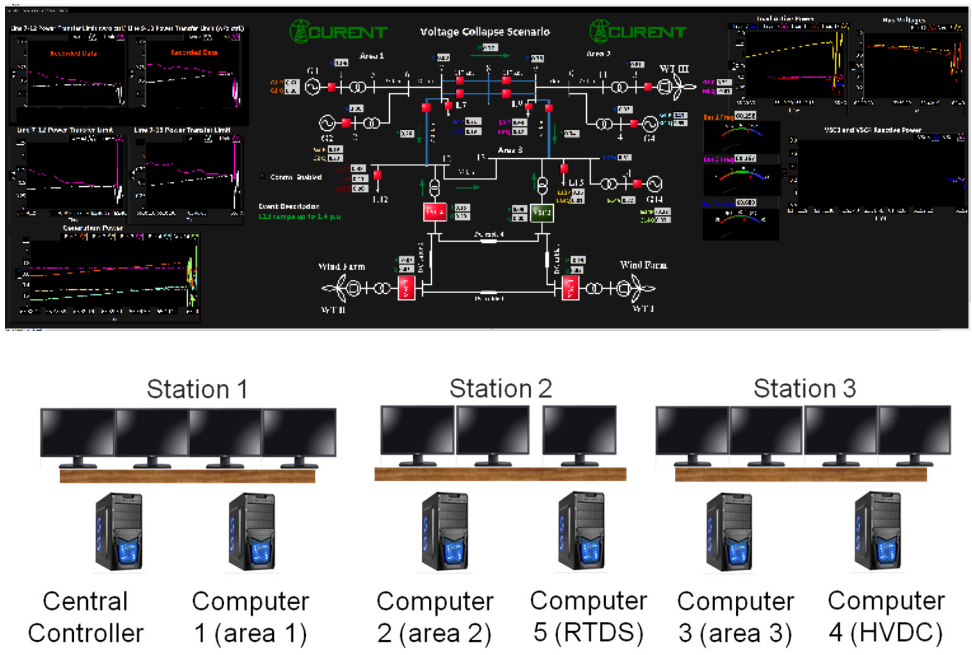


Figure 57. HTB control center.

As shown in Figure 57, all the voltage phasor, power and frequency measurements are sent to the visualization application of the control center, and displayed on the large screen for operators. The voltage stability monitoring and closed-loop control module retrieves the data from the server to call the stability function and preventive control function in real-time.

The three-area system shown in Figure 58 is real-time emulated using the HTB, where the load center is fed by tie line 7-12, tie line 9-13, and one Multi-Terminal Direct Current (MTDC) system. The system represents a reduced NPCC region, where area 3 represents the Connecticut load center (CLC) with voltage stability concerns, and areas 1 and 2 respectively represent the New York area (NYISO) and the New England area (ISO-NE) outside that load center.

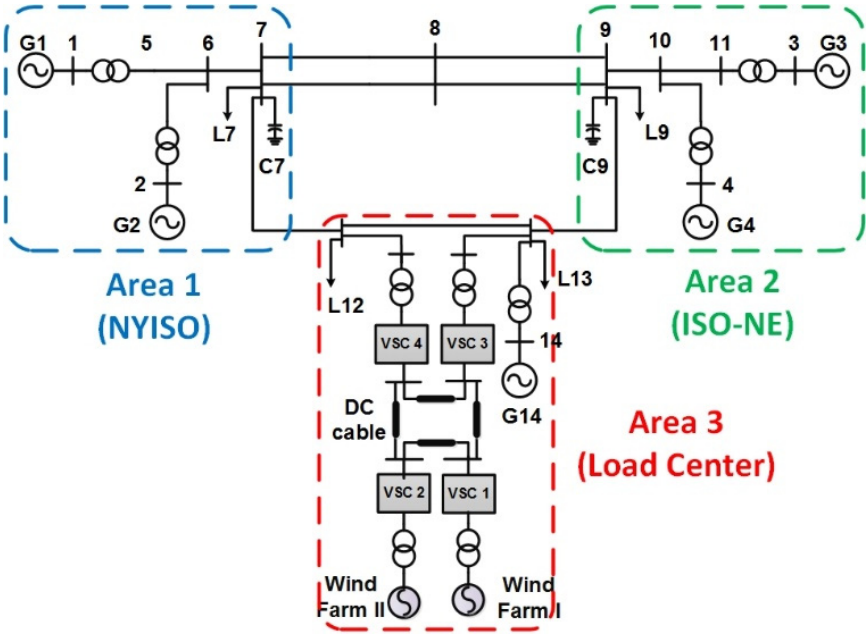


Figure 58. HTB three-area system topology.

Two scenarios, respectively with and without control of the VAR support from the wind farms, are designed with the same contingency to demonstrate the real-time voltage stability monitoring and closed-loop control on the HTB.

5.3 Scenario 1: Voltage Collapse without Control

In the 1st scenario, all loads are ZIP loads which are composed by loads of 20% constant impedance, 20% constant current and 60% constant power. After the HTB system reaches its steady state, the contingency has been activated. The active power of load 13 increases from 0.594 p.u. to 1.4 p.u. Since the real-time voltage stability control module has been disabled for scenario 1, as shown in Figure 59, the system enters a state of voltage collapse with a progressive and uncontrollable decline in voltage at the end.

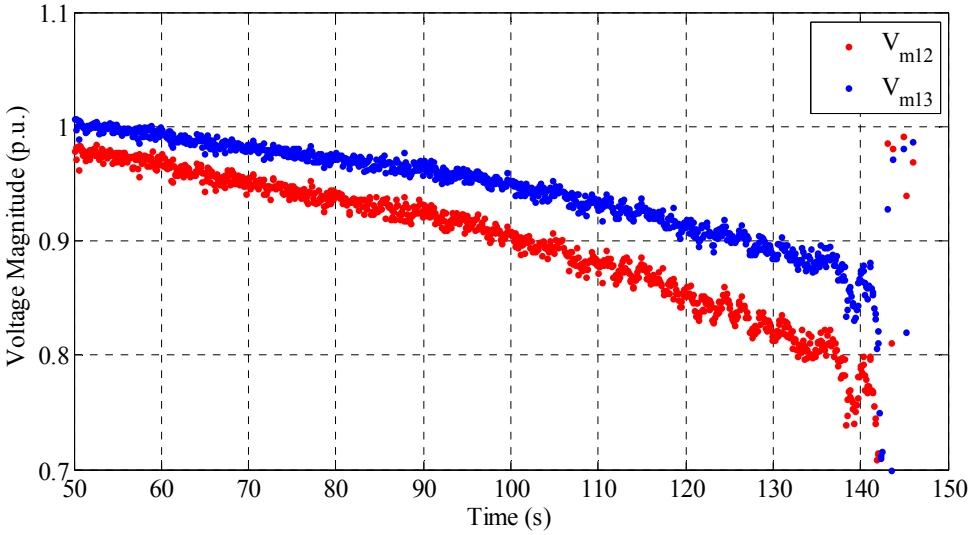


Figure 59. HTB three-area system topology.

Figure 60 shows the PV curves of both transmission lines. Obviously, the "nose" point of PV_{12} has already been passed while the "nose" point of PV_{13} has not, which indicates the voltage collapse may happen after the transmission line 13 reached the "nose" point.

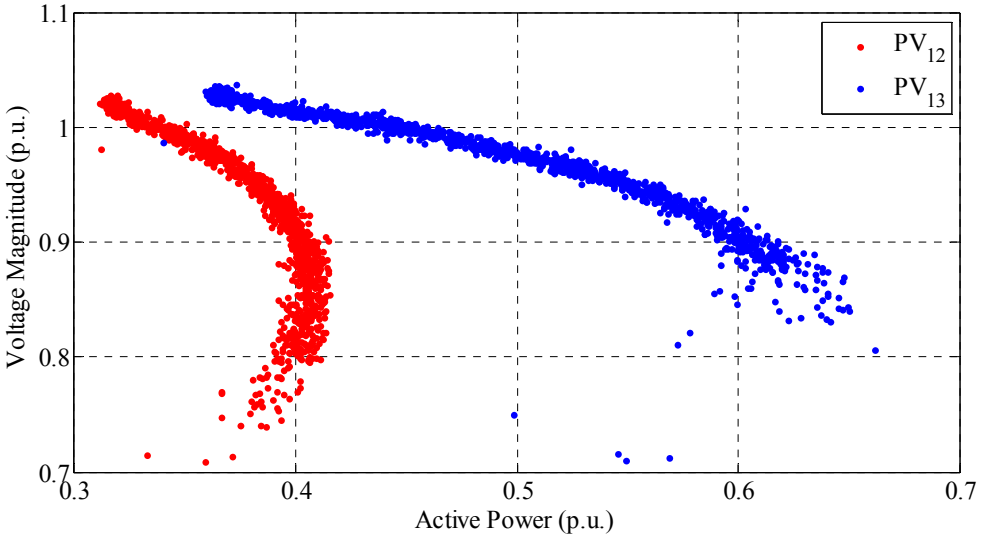


Figure 60. PV curves of transfer active power to bus 12 and bus 13.

The new MBVSA method adopts a 2+1 buses equivalent in order to calculate the power transfer limits individually for two tie lines of the load center, i.e. lines 7-12 and 9-13. The power transfer limits are calculated and shown in Figure 61. In this scenario, only load 13 is increasing, which tells the operator to choose the limits with respect to the direction of load 13 increase. The margins of Bus 12 and Bus 13 are different from each other, so the preventive control module will monitor both of the margins to make a decision. With a pre-designed 10% margin threshold, the green vertical line shows the anticipative control time (101.7s). Tie line 7-12 hits the limit first at 114.5s, which means

the voltage instability originates from that side. Then, after tie line 9-13 hits the limit at 125.5s, voltage collapse happens at 140s. Therefore, this new method predicted the voltage collapse when the first limit was hit before voltage collapse really happened. One of the major advantages provided by this method is the accurate individual stability margin for each tie line, which is brought about by modelling the relationship between all tie lines and monitoring them separately.

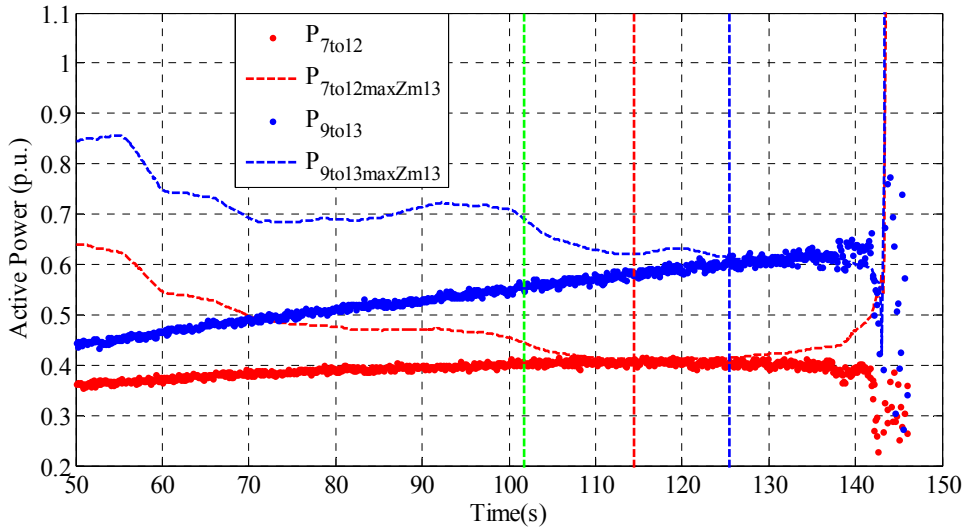


Figure 61. Actual power transfers and their limits.

5.4 Scenario 2: Automatic Control against Voltage Collapse

In the 2nd scenario, the contingency and configuration of the system are almost the same as the ones in the 1st scenario except for the voltage stability control enabled. The pre-designed threshold to trigger the control action has been defined as 10% of the active power.

As shown in Figure 62, the system reached the steady state when both tie-lines are at state A. After they met the control threshold at A', the preventive control is triggered to increase VAR support from the wind farm by 0.4 p.u. This extra VAR support helps the system to enter another state B' with higher stability margin. From the results, the system was saved by the preventive control action triggered by the MBVSA method with high accuracy and reliability.

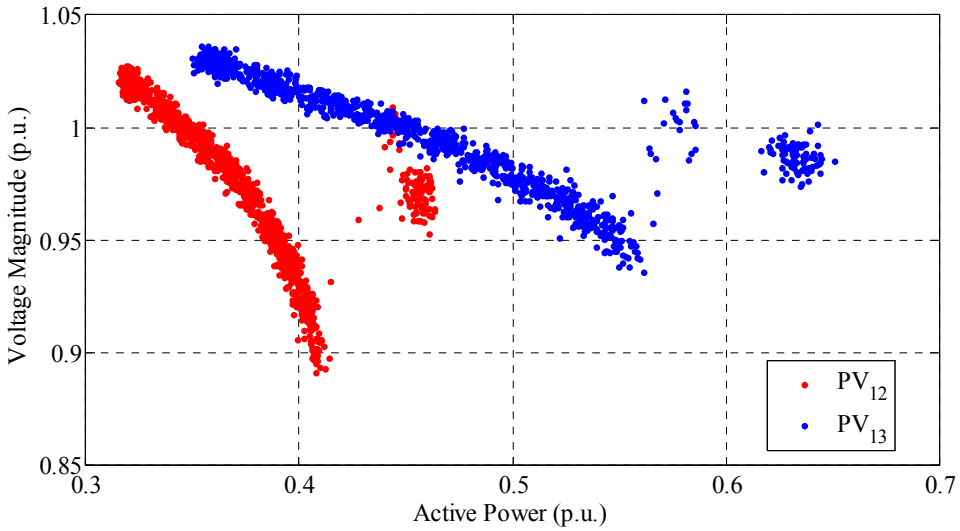


Figure 62. Trajectories of tie line power transfer PV curves with preventive control triggered.

As shown in Figure 63, the preventive action is triggered at 106.3s when the margin drops to 10%, and this time instant is shown as the green vertical dashed line. After the preventive control and the transient dynamics, the system operates at a new stable state.

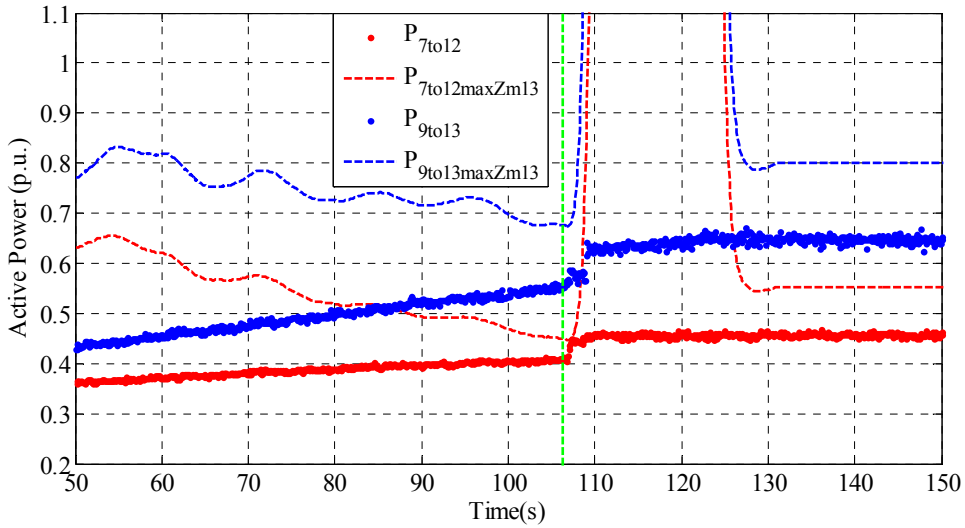


Figure 63. Actual power transfers and their limits.

5.5 Conclusion

This chapter proposed the implementation of the new MBVSA monitoring and the closed-loop control strategy based on the *N*+1 buses equivalent. From the results of the two voltage collapse scenarios, this new MBVSA method and the associated closed-loop control strategy demonstrate high performances to prevent voltage collapse using real-time measurements, and potentials for practical applications at control rooms.

CHAPTER 6

CONCLUSION AND FUTURE WORK

6.1 Summary of Contributions

This work proposes a hybrid approach to real-time voltage stability monitoring and control for load areas. Specifically, the contributions of this work can be summarized in the following five aspects:

1. This work adopts an N+1 buses equivalent system so as to model and monitor individual tie lines compared to traditional TE based methods. For each tie line, the proposed new method solves the power transfer limit against voltage instability analytically as a function of all parameters of that N+1 buses equivalent, which are online identified from real-time synchronized measurements on boundary buses of the load area. Thus, this resulting new MBVSA method can directly calculate the real-time power transfer limit on each tie line, which cannot be obtained from the traditional TE.

2. This work assesses the voltage stability margins under an n-1 contingency while most of MBVSA methods do not have such an important capability.

3. This work decreases the computation burdens for online simulation studies of n-1 contingencies by eliminating the non-critical contingencies using the MBVSA method.

4. This work offers a practical framework to provide stability information and preventive control by taking the advantages of both measurement-based methods and simulation-based methods.

5. The new MBVSA is implemented on a physical power system which is the CURENT Hardware Test Bed (HTB) system, and the effectiveness of real-time voltage stability monitoring and closed-loop control against voltage collapse has been validated.

6.2 Future Works

The following directions can be considered for future work.

1. A new external system equivalent using power flow data and network transformation may be investigated.

2. The advanced optimization method and parallel computing are expected to improve the accuracy and computation speed of the proposed hybrid scheme for online VSA.

3. Field studies are expected to verify the functionalities of the proposed VSA approach since it will further verify the implementation of theoretical techniques and polish the existing procedures.

LIST OF REFERENCES

[1] W. Taylor, Power System Voltage Stability: McGraw-Hill, 1994.

[2] G. Wang, C. Liu, N. Bhatt, E. Farantatos, and M. Patel. "Observability of Nonlinear Power System Dynamics Using Synchrophasor Data," *International Transactions on Electrical Energy Systems,* vol. 26, no.5, pp. 952-967, 2016.

[3] J. Guo, H. Liu, D. Zhou, J. Chai, Y. Zhang, and Y. Liu, "Real-time Power System Electromechanical Mode Estimation Implementation and Visualization Utilizing Synchrophasor Data," in Proc. 2016 IEEE PES Transmission and Distribution Conference and Exposition, May 2-5, 2016.

[4] T. Jiang, H. Yuan, H. Jia, N. Zhou, F. Li, "Stochastic Subspace Identification-based Approach for Tracking Inter-area Oscillatory Modes in Bulk Power System Utilizing Synchrophasor Measurements," *IET Generation, Transmission and Distribution,* vol. 9, issue 15, pp. 2409-2418, Nov. 2015.

[5] G. Wang, C. Liu, N. Bhatt, E. Farantatos, K. Sun, "Observability for PMU-Based Monitoring of nonlinear power system dynamics. Bulk Power System Dynamics and Control," - IX Optimization, Security and Control of the Emerging Power Grid (IREP), Crete, Greece, August, 2013.

[6] J. Guo, Y. Zhang, T. King, Y. Liu, B. David, F. Nuroglu, F. Bai, and X. Wang, "Worldwide Power System Oscillations Observed by Distribution Level Phasor Measurements," in CIGRE/EPRI Grid of the Future Symposium, 2013.

[7] L. E. Bernal, F. Hu, K. Sun, E. Farantatos, "Identification and Wide-area Visualization of the Centers of Oscillation for a Large-scale Power System", 2014 IEEE PES General Meeting, National Harbor, MD.

[8] J. Guo, Y. Ye, Y. Zhang, Y. Lei, and Y. Liu, "Events Associated Power System Oscillations Observation Based on Distribution-level Phasor Measurements," in Proc. 2014 IEEE PES Transmission and Distribution Conference and Exposition, April 2014.

[9] B. Gao, G. K. Morison, and P. Kundur, "Voltage Stability Evaluation Using Modal Analysis", *IEEE Transactions on Power Systems,* vol.7, no. 4, pp. 1529-1542, Nov. 1992.

[10] Y. Mansour, W. Xu, F. Alvarado, and C. Rizzin, "SVC Placement Using Critical Modes of Voltage Instability," *IEEE Transactions on Power Systems,* vol. 9, no. 2, pp. 757- 763, May 1994.

[11] T. Van Cutsem and C. Vournas, Voltage Stability of Electric Power Systems. Norwell, MA: Kluwer, 1998.

[12] V Ajjarapu and C. Christy, "The Continuation Power Flow: A Tool for Steady State Voltage Stability Analysis," *IEEE Transactions on Power Systems,* vol. 7, no. 1, pp. 416-423, Feb. 1992.

[13] C. Cañizares, Ed., Voltage Stability Assessment: Concepts, Practices, and Tools, 2002, ISBN 0 780 378 695. Special publication of the IEEE Power System Stability Subcommittee.

[14] W. W. Hager, Applied Numerical Algebra, New Jersey: Prentice Hall Inc., 1998.

[15] K. Ellithy, M. Shaheen, M. Al-Athba, A. Al-Subaie, S. Al-Mohannadi, S. Al-Okkah, S. Abu-Eidah, "Voltage Stability Evaluation of Real Power Transmission System Using Singular Value Decomposition Technique," Power and Energy Conference, PECon. IEEE 2nd International, pp.1691-1695, Dec. 2008.

[16] V. Venikov, V. Stroev, V. Idelchick, and V. Tarasov, "Estimation of Electrical Power System Steady-state Stability in Load Flow Calculations," *IEEE Transactions on Power Apparatus and Systems,* vol. PAS-94, no. 3, pp. 1034-1041, June 1975.

[17] P. Löf, T. Smed, G. Andersson, and D. Hill, "Fast Calculation of a Voltage Stability Index," *IEEE Transactions on Power Systems,* vol. 7, no. 1, pp. 54-64, Feb. 1992.

[18] N. Flatabo, R. Ognedal, T. Carlsen, "Voltage Stability Condition in a Power Transmission System Calculated by Sensitivity Methods," *IEEE Transactions on Power Systems,* vol. 5, no,4, pp. 1286-1293, Nov. 1990.

[19] R. Schlueter, I. Hu, M. Chang, J. Lo, A. Costi, "Methods for Determining Proximity to Voltage Collapse," *IEEE Transactions on Power Systems,* vol.6, no.1, pp.285-292, Feb. 1991.

[20] C. Concordia, "Voltage Stability Simplified," *International Journal of Electrical & Energy Systems,* vol. 14, no. 5, pp. 364-366, Oct. 1992.

[21] M. Begovic and A. Phadke, "Control of Voltage Stability Using Sensitivity analysis," *IEEE Transactions on Power Systems,* vol. 7, no. 1, pp. 114–123, Feb. 1992.

[22] S. Greene, I. Dobson, and F. Alvarado, "Sensitivity of the Loading Margin to Voltage Collapse with Respect to Arbitrary Parameters," *IEEE Transactions on Power Systems,* vol. 12, no. 1, pp. 262–272, Feb. 1997.

[23] F. Capitanescu, T. Van Cutsem, "Unified Sensitivity Analysis of Unstable or Low Voltages Caused by Load Increases or Contingencies," *IEEE Transactions on Power Systems,* Vol. 20, No. 1, pp. 321-329, Feb. 2005

[24] Y. Gong, "Development of an Improved On-Line Voltage Stability Index Using Synchronized Phasor Measurement," Phd Dissertation, Department of Electrical & Computer Engineering, Mississippi State University, 2006.

[25] T. Gou, R. Schlueter, "Identification of Generic Bifurcation and Stability Problems in Power System Differential-algebraic Model," *IEEE Transactions on Power Systems,* vol. 9, pp. 1032–1044, May 1994.

[26] W. Marszalek, Z. Trzaska, "Singularity-induced Bifurcations in Electrical Power Systems," *IEEE Transactions on Power Systems,* vol. 20, pp. 312–320, Feb. 2005.

[27] T. Cutsem, L. Wehenkel, et al., "Decision Tree Approaches to Voltage Security Assessment," IEE Proceedings C Generation, Transmission and Distribution, vol. 140, no. 3, pp. 189-198, 1993.

[28] R. Diao, K. Sun, V. Vittal et al., "Decision Tree-based Online Voltage Security Assessment Using PMU Measurements," *IEEE Transactions on Power Systems,* vol. 24, no. 2, pp. 832-839, 2009.

[29] K. Vu, M. Begovic, D. Novosel et al., "Use of Local Measurements to Estimate Voltage-stability Margin," *IEEE Transactions on Power Systems,* vol. 14, no. 3, pp. 1029-1035, 1999.

[30] I. Smon, G. Verbic, F. Gubina, "Local Voltage-stability Index Using Tellegen's Theorem," *IEEE Transactions on Power Systems,* vol. 21, no. 3, pp. 1267-1275, 2006.

[31] H. Yuan and F. Li, "A Comparative Study of Measurement-based Thevenin Equivalents Identification Methods," 46th North American Power Symposium, 6 pages, Pullman, WA, Sept. 7-9, 2014.

[32] B. Milosevic, M. Begovic, "Voltage-stability Protection and Control Using a Wide-area Network of Phasor Measurements," *IEEE Transactions on Power Systems,* vol. 18, no. 1, pp. 121-127, 2003.

[33] M. Parniani, et al., "Voltage Stability Analysis of a Multiple-infeed Load Center Using Phasor Measurement Data," IEEE PES Power Systems Conference and Exposition, Nov 2006.

[34] S. Corsi, and G. Taranto, "A Real-time Voltage Instability Identification Algorithm based on Local Phasor Measurements," *IEEE Transactions on Power Systems*, vol. 23, no. 3, pp. 1271-1279, 2008.

[35] C. Vournas, and N. Sakellaridis, "Tracking Maximum Loadability Conditions in Power Systems," in Proc. 2007 Bulk Power System Dynamics and Control-VII, Charleston, SC, Aug. 2007.

[36] M. Glavic, and T. Cutsem, "Wide-area Detection of Voltage Instability from Synchronized Phasor Measurements. Part I: Principle," *IEEE Transactions on Power Systems,* vol. 24, no. 3, pp. 1408-1416, 2009.

[37] C. Vournas, C. Lambrou, M. Glavic et al., "An Integrated Autonomous Protection System against Voltage Instability based on Load Tap Changers," 2010 iREP Symposium, Aug. 2010.

[38] S. Abdelkader, D. Morrow, "Online Thévenin Equivalent Determination Considering System Side Changes and Measurement Errors," *IEEE Transactions on Power Systems*, vol. PP, no. 99, pp. 1-10, 2014.

[39] L. He, C. Liu, "Parameter Identification with PMUs for Instability Detection in Power Systems with HVDC Integrated Offshore Wind Energy," *IEEE Transactions on Power Systems,* vol. 29, no. 2, pp. 775-784, 2014.

[40] W. Li, et al., "Investigation on the Thevenin Equivalent Parameters for Online Estimation of Maximum Power Transfer Limits," *IET Generation, Transmission & Distribution,* vol. 4, no. 10, pp. 1180-1187, 2010.

[41] K. Sun, F. Hu, N. Bhatt, "A New Approach for Real-Time Voltage Stability Monitoring Using PMUs", 2014 IEEE ISGT Asia, Kuala Lumpur, Malaysia.

[42] Y. Wang, I. Pordanjani, et al, "Voltage Stability Monitoring based on the Concept of Coupled Single-port Circuit," *IEEE Transactions on Power Systems,* vol. 26, no. 4, pp. 2154-2163, 2011.

[43] J. Liu, C. Chu, "Wide-area Measurement-based Voltage Stability Indicators by Modified Coupled Single-port Models," *IEEE Transactions on Power Systems,* vol. 29, no. 2, pp. 756-764, 2014.

[44] W. Xu, et al., "A Network Decoupling Transform for Phasor Data based Voltage Stability Analysis and Monitoring," *IEEE Transactions on Power Systems,* vol. 3, no. 1, pp. 261–270, Mar.2012.

[45] I. Pordanjani, et al, "Identification of Critical Components for Voltage Stability Assessment Using Channel Components Transform," *IEEE Transactions on Smart Grid,* vol. 4, no. 2, pp. 1122-1132, 2013.

[46] P. Zhang, L. Min, N. Zhang, Voltage Instability Load Shedding, EPRI Report No. 1012491, 2006.

[47] K. Sun, P. Zhang, L. Min, Measurement-based Voltage Stability Monitoring and Control for Load Centers, EPRI Report No. 1017798, 2009.

[48] P. Zhang, L. Min, J. Chen, Measurement-based Voltage Stability Monitoring and Control, US Patent 8,126,667, 2012.

[49] F. Galvan, A. Abur, K. Sun et al., "Implementation of Synchrophasor Monitoring at Entergy: Tools, Training and Tribulations," IEEE PES General Meeting, 2012.

[50] H. Yuan, F. Li, "Hybrid Voltage Stability Assessment (VSA) for N-1 Contingency," *Electric Power Systems Research,* vol. 122, pp. 65–75, May. 2015.

[51] H. Yuan, T. Jiang, H. Jia, F. Li, Y. Mishra, H. Chen, and G. Li, "Real-Time Wide-area Loading Margin Sensitivity (WALMS) in Power Systems," IEEE PES General Meeting 2015, 5 pages, Denver, Colorado, July 26-30, 2015.

[52] T. Jiang, L. Bai, H. Jia, H. Yuan, F. Li, "Identification of Voltage Stability Critical Injection Region in Bulk Power Systems based on the Relative Gain of Voltage

Coupling," *IET Generation, Transmission and Distribution,* vol. 10, issue 7, pp. 1495-1503, May. 2016.

[53] F. Hu, K. Sun, et al, "An Adaptive Three-bus Power System Equivalent for Estimating Voltage Stability Margin from Synchronized Phasor Measurements," 2014 IEEE PES General Meeting, National Harbor, MD.

[54] J. Nocedal, and S. J. Wright, "Numerical Optimization 2nd," 2006.

[55] K. Sun, F. Hu, N. Bhatt, E. Farantatos, A. Del Rosso (PM), "Hybrid Voltage Stability Assessment (HVSA): Integration of Simulation-Based and Measurement-Based Approaches in Real-Time Operation", EPRI Product ID: 3002001313, 2013.

[56] N. Bhatt, E. Farantatos, A. Del Rosso, K. Sun, F. Hu, Real-Time Reactive Power Management and Voltage Control: Hybrid Voltage Stability Assessment (HVSA), EPRI Product ID: 3002002868, 2014.

[57] F. Hu; K. Sun; A. Del Rosso; E. Farantatos; N. Bhatt, "Measurement-Based Real-Time Voltage Stability Monitoring for Load Areas," *IEEE Transactions on Power Systems,* vol. 31, No. 4, pp. 3189-3201, July 2016.

[58] J. Chow, R. Galarza, P. Accari et al., "Inertial and Slow Coherency Aggregation Algorithms for Power System Dynamic Model Reduction," *IEEE Transactions on Power Systems,* vol. 10, no. 2, pp. 680-685, 1995.

[59] T. Jiang, H. Jia, H. Yuan, N. Zhou, and F. Li, “Projection Pursuit: A General Methodology of Wide-Area Coherency Detection in Bulk Power Grid,” *IEEE Transactions on Power Systems,* vol. 31, no. 4, 2016, Jul. 2016.

[60] P. Sauer, “On the Formulation of Power Distribution Factors for Linear Load Flow Methods," *IEEE Transactions on Power Apparatus and Systems,* vol. PAS-100, no. 2, 1981.

[61] A. D.-G. P. S. Yu Chen, “Online Estimation of Power System Distribution Factors-A Sparse Representation Approach,” in North American Power Symposium, 2013.

[62] A. P. Marija Ilic-Spong, “Redistribution of Reactive Power Flow in Contingency Studies," *IEEE Transactions on Power Systems,* vol. PWRS-1, no. 3, 1986.

[63] S. S. S. N. Singh, “Improved Voltage and Reactive Power Distribution Factors for Outage Studies,” *IEEE Transactions on Power Systems,* vol. 12, no. 3, 1997.

[64] J. Guo, Y. Zhang, M. A. Young, M. J. Till, A. Dimitrovski, Y. Liu, and P. Williging, “Design and Implementation of a Real-Time Off-Grid Operation Detection Tool from a Wide-Area Measurements Perspective,” *IEEE Transactions on Smart Grid,* vol.6, no.4, pp. 2080-2087, 2015.

[65] H. D. Chiang, A. J. Flueck, K. S. Shah, and N. Balu, “CPFLOW: A Practical Tool for Tracing Power System Steady-state Stationary Behavior due to Load and

Generation Variations," *IEEE Transactions on Power Systems,* vol. 10, no. 2, pp. 623–634, May 1995.

[66] P.-A. Löf, G. Andersson, and D. J. Hill, "Voltage Stability Indices for Stressed Power Systems," *IEEE Transactions on Power Systems*, vol. 8, no. 1, pp. 326–335, Feb. 1993.

[67] C. Canizares, "On Bifurcations, Voltage Collapse and Load Modeling," *IEEE Transactions on Power Systems,* vol. 10, no. 1, pp. 512–522, 1995.

[68] C. Huang, F. Li, Y. Jiang, T. Ding, J. Guo, Y. Liu, "A Bounded Model of the Communication Delay for System Integrity Protection Schemes," *IEEE Transactions on Power Delivery,* in-press, 2016.

[69] J. Mahseredjian, V. Dinavahi, and J. A. Martinez, "Simulation Tools for Electromagnetic Transients in Power Systems: Overview and Challenges," *IEEE Transactions on Power Delivery,* vol. 24, no. 3, pp. 1657–1669, Jul. 2009.

[70] R. Torquato, Q. Shi, W. Xu, and W. Freitas, "A Monte Carlo Simulation Platform for Studying Low Voltage Residential Networks," *IEEE Transactions on Smart Grid,* vol.5, no.6, pp.2766-2776, Nov. 2014.

[71] B. Kroposki, and G. Martin, "Hybrid Renewable Energy and Microgrid Research Work at NREL," in Proc. 2010 IEEE PES General Meeting, Minneapolis, MN.

[72] J. Eto, R. Lasseter, B. Schenkman, J. Stevens, D. Klapp, H. Vokommer, E. Linton, H. Hurtado, J. Roy, "Overview of CERTS Microgrid Laboratory Test Bed", in Proc. CIGRE/IEEE PES Joint Symposium on Integration of Wide-Scale Renewable Resources Into the Power Delivery System, pp. 1-7, 2009.

[73] O. A. Mohammed, M. A. Nayeem, and A. K. Kaviani "A Laboratory based Microgrid and Distributed Generation Infrastructure for Studying Connectivity Issues to Operational Power Systems," in Proc. 2010 IEEE PES General Meeting, Minneapolis, MN.

[74] L. Bai, T. Ding, Q. Hu, F. Li, and H. Sun, "Robust Mean-Variance Optimization Model for Grid-Connected Microgrids," IEEE PES General Meeting 2015, Denver, Colorado, July 26-30, 2015.

[75] V. Salehi, A. Mohamed, A. Mazloomzadeh, and O. A. Mohammed, "Laboratory-based Smart Power System, Part I: Design and System Development," *IEEE Transactions on Smart Grid,* vol. 3, no. 3, pp. 1394–1404, Sep. 2012.

[76] C. Huang, Y. Xu, C. Harley, D. Masters, and F. Li, "LabVIEW FPGA based Electromagnetic Transient Simulator Using Nodal Analysis Methods and State-space Analysis Methods," in Proc. 2015 IEEE DRPT, pp. 1-5.

[77] H. Hu, Q. Shi, Z. He, J. H, and S. Gao, "Potential harmonic resonance impacts of PV inverter filters on distribution systems," *IEEE Transactions on Sustainable Energy,* vol.6, no.1, pp.151-161, Jan. 2015.

[78] Q. Shi, H. Hu, W. Xu, and J. Yong, "Low-order harmonic characteristics of photovoltaic inverters," *International Transactions on Electrical Energy Systems,* vol. 26, no. 2, pp. 347–364, Feb. 2016.

[79] C. Huang, F. Li, Z. Jin, "Maximum Power Point Tracking Strategy for Large-scale Wind Generation Systems Considering Wind Turbine Dynamics," *IEEE Transactions on Industrial Electronics,* vol. 62, no. 4, pp. 2530-2539, Apr. 2015.

[80] L. Bai, F. Li, T. Jiang, H. Jia, "Robust Scheduling for Wind Integrated Energy Systems Considering Gas Pipeline and Power Transmission N-1 Contingencies," *IEEE Transactions on Power Systems,* in-press, 2016.

[81] L. Bai, F. Li, H. Cui, T. Jiang, H. Sun and J. Zhu, "Interval Optimization based Operating Strategy for Gas-Electricity Integrated Energy Systems Considering Demand Response and Wind Uncertainty," *Applied Energy (Elsevier),* vol. 167, pp. 270-279, Apr. 2016.

[82] L. Yang, Y. Ma, J. Wang, J. Wang, X. Zhang, L. M. Tolbert, F. Wang, K. Tomsovic, "Development of Converter based Reconfigurable Power Grid Emulator," in Proc. 2014 IEEE Energy Conversion Congress and Exposition, pp. 3990-3997.

[83] C. Huang, F. Li, T. Ding, and Z. Jin, "Second-order Cone Programming-based Optimal Control Strategy for Wind Energy Conversion Systems over Complete Operating Regions," *IEEE Transactions on Sustainable Energy,* vol. 6, no. 1, pp. 263-271, Jan. 2015.

[84] D. Osipov, F. Hu, K. Sun, "Voltage Stability Margin Estimation for a Load Area Using a Three-Bus Equivalent," 2016 IEEE PES General Meeting, Boston, MA.

[85] F. Hu, L. Yang, J. Wang, Y. Ma, K. Sun, L. M. Tolbert, F. Wang, "Measurement-based Voltage Stability Assessment and Control on CURENT Hardware Test Bed System," 2016 IEEE PES General Meeting, Boston, MA.

APPENDIX

Publications during Ph.D. Study

Journal Papers

[J1] **F. Hu**, K. Sun, "The *n*-1 Sensitivity Analysis and Contingency Screening of the Measurement-Based Real-Time Voltage Stability Monitoring," *in progress*.

[J2] **F. Hu**, K. Sun, "Properties of the Power Transfer Limits for the *N*+1 Equivalent Model," *in progress*.

[J3] **F. Hu**, K. Sun, A. D. Rosso, E. Farantatos, N. Bhatt, "Measurement-Based Real-Time Voltage Stability Monitoring for Load Areas," *IEEE Trans. Power Systems*, vol. 31, no. 4, pp. 2787-2798, July 2016.

Conference Papers

[C1] **F. Hu**, L. Yang, J. Wang, Y. Ma, K. Sun, L. M. Tolbert, F. Wang, "Measurement-based Voltage Stability Assessment and Control on CURENT Hardware Test Bed System," 2016 IEEE PES General Meeting, Boston, MA.

[C2] D. Osipov, **F. Hu**, K. Sun, "Voltage Stability Margin Estimation for a Load Area Using a Three-Bus Equivalent," 2016 IEEE PES General Meeting, Boston, MA.

[C3] **F. Hu**, K. Sun, A. D. Rosso, E. Farantatos, N. Bhatt, "An Adaptive Three-bus Power System Equivalent for Estimating Voltage Stability Margin from Synchronized Phasor Measurements," 2014 IEEE PES General Meeting, National Harbor, MD.

[C4] L. E. Bernal, **F. Hu**, K. Sun, E. Farantatos, "Identification and Wide-area Visualization of the Centers of Oscillation for a Large-scale Power System", 2014 IEEE PES General Meeting, National Harbor, MD.

[C5] K. Sun, **F. Hu**, N. Bhatt, "A New Approach for Real-Time Voltage Stability Monitoring Using PMUs", 2014 IEEE ISGT Asia, Kuala Lumpur, Malaysia.

Technical Reports

[T1] N. Bhatt, E. Farantatos, A. Del Rosso, K. Sun, **F. Hu**, Real-Time Reactive Power Management and Voltage Control: Hybrid Voltage Stability Assessment (HVSA), EPRI Product ID: 3002002868, 2014.

[T2] K. Sun, **F. Hu**, N. Bhatt, E. Farantatos, A. Del Rosso (PM), Hybrid Voltage Stability Assessment (HVSA): Integration of Simulation-Based and Measurement-Based Approaches in Real-Time Operation, EPRI Product ID: 3002001313, 2013.

VITA

Fengkai Hu joined the University of Tennessee, Knoxville in August 2012 to pursue the Ph.D. degree in Electrical Engineering. Prior to that, he received the B.S. and M.S. degrees in Automation from the University of Electronic Science and Technology of China, Chengdu, Sichuan, China, in 2009 and 2012, respectively. His research interests include power system stability and control, wide area measurement system visualization and smart grid communication.